The Pennsylvania State University

The Graduate School

College of Engineering

TISSUE CUTTING MECHANICS OF DYNAMIC NEEDLE INSERTION

A Dissertation in

Mechanical Engineering

by

Andrew C. Barnett

Submitted in Partial Fulfillment
of the Requirements
for the Degree of

Doctor of Philosophy

May 2016

The dissertation of Andrew C. Barnett was reviewed and approved* by the following:

Jason Z. Moore
Assistant Professor of Mechanical and Engineering
Dissertation Advisor
Chair of Committee

Mary Frecker
Professor of Mechanical Engineering

Scarlett Miller
Assistant Professor of Engineering Design and Mechanical Engineering

Zoubeida Ounaies
Dorothy Quiggle Career Developmental Professorship
Professor of Mechanical Engineering

Siyang Zheng
Assistant Professor of Biomedical Engineering

Karen A. Thole
Professor of Mechanical Engineering
Department Head of Mechanical and Nuclear Engineering

*Signatures are on file in the Graduate School

ABSTRACT

Needles are commonly used in many medical procedures to sample blood and tissue, inject drugs and anesthetics, and implant radioactive seeds among other uses. The procedures of brachytherapy cancer treatment and tissue biopsy utilize needles to reach precise locations inside the body. However, due to high insertion forces, high accuracy is difficult to achieve. Previous researchers have demonstrated that vibration can reduce these high needle insertion forces. However, little research has currently focused on how the dynamic motions of vibration and velocity effect needle insertion force. This dissertation directly fills this void in knowledge to help reduce needle insertion force, which increases needle position accuracy. This research creates a further understanding of how velocity and vibration affect needle insertion force. This work also presents experimental results and force modeling of dynamic needle insertions. Based on this research, a novel compliant needle is designed and developed that utilizes vibration to reduce insertion forces.

Three major topics are explored in this research: fracture mechanics model development, analysis of vibrational effect on insertion force, and the development of a novel compliant needle geometry to reduce needle insertion force. Firstly, a fracture mechanics model was developed that allowed for the understanding of how fracture force, tissue spreading force, and friction force impact the overall needle insertion force over a range of velocities (1-80 mm/s). The parameters of tissue toughness and tissue shear modulus were experimentally tested on ex vivo porcine skin. Model results showed the total needle insertion force was comprised of 70% tearing force which was dependent on the fracture toughness, 13% spreading force which was dependent on the shear modulus, and the remaining 17% friction force.

To analyze the effect of vibration on insertion force, two needle insertion experiments were performed. First, lancet hypodermic needles were inserted into ex vivo porcine skin with applied

vibration. The insertion force was reduced up to 35% with the application of vibration compared to insertion without applied vibration. Next, experiments were performed using five conical tipped needles of varying grind angle sharpness between 15° and 75°. These needles were inserted with applied vibration into ex vivo bovine liver and polyurethane sheets. The experiments into bovine liver showed that any vibratory combination of amplitude and frequency reduced the insertion force of the sharpest needle, grind angle of 15°, by an average of 55.1% compared to the insertion of the needle without applied vibration. However, the bluntest geometry needle, grind angle of 75°, had no significant reduction in bovine liver insertion force from applied vibration compared to the insertion without vibration. The experiments into polyurethane reinforced these findings that sharper needles benefit more from vibration in reducing insertion force compared to blunter needles.

Lastly, a novel compliant geometry was developed that transforms applied axial vibration into transverse motion at the needle tip. The needle geometry consisted of four grind planes to create the tip and a single axis flexural hinge created with two slits. Finite element modal analysis was performed on this needle tip geometry to determine the motion upon vibration. Experimentally the motion was measured using a stereomicroscope to be 16.0 μm in the transverse direction for the compliant geometry. Experiments showed the compliant needle was able to reduce the puncture and friction forces of insertion (18.8% and 71.0% respectively) compared to a standard non-compliant needle without applied vibration. This was due to the crack length in the skin simulant increasing by 190% with the compliant needle over the non-compliant needle, allowing the compliant needle to pass through the crack with less force. This reduced friction force can improve needle placement accuracy, thereby improving the efficacy of needle based procedures such as biopsy and brachytherapy.

TABLE OF CONTENTS

LIST OF FIGURES

LIST OF TABLES

NOMENCLATURE

$A(x)$	Cross-sectional area
a	Length of crack in the tissue
$\boldsymbol{a}$	Intersection of planes P_nA_γ
A_i	Theoretical input amplitude of vibration
A_o	Experimental measured amplitude of vibration
A_γ	Needle face plane
α_h	Strain hardening factor
α	Rake angle
$\boldsymbol{b}$	Intersection of plane P_nP_r
β	Compliant needle rotation angle
β_l	Rotation angle of lancets
c	Wave propagation speed
d	Outer diameter of the needle
D_1	Distance from needle tip of first slit
D_2	Offset distance of slits
E	Young's Modulus
$\dot{\varepsilon}$	Strain rate of the tissue
f_c	Contact factor
f_i	Applied frequency of vibration
γ	Radial needle position
H	Depth of slit

J_{IC}	Mode I fracture toughness of the tissue
k_1	Stepped horn correction factor
k_2	Stepped horn correction factor
L	Length of ultrasonic horn
l	Insertion depth of the needle
Λ	Strain energy stored in tissue
λ	Inclination angle
λ_i	Principle stretch ratios
λ_z	Stretch ratio in the z (pull) direction
μ	Shear modulus of the tissue
N	Number of termed Ogden fit
ND	Normalized difference
n_γ	Normal vector of needle face A_γ
ω	Resonance frequency
P	Total insertion force
P'	Insertion force of second insertion
P_c	Cutting Force
P_F	Friction Force
P_{FP}	Puncture Friction Force
P_n	Cutting edge normal plane
P_r	Cutting direction plane
P_s	Spreading Force

ϕ	Strain energy density
ϕ	Secondary bevel angle
r	Outer radius of the needle
R_s	Radius of back skin plate hole
ρ	Material density
$\boldsymbol{s}$	Cutting edge tangent vector
σ_z	Stress in the z (pull) direction
t	Thickness of slit
$\theta(t)$	Time dependent orientation of cutting direction
$U(x)$	Axial displacement
V	Volume
v	Needle insertion velocity
$\boldsymbol{v}$	Normal vector of cutting direction plane
v_o	Steady insertion speed of vibration insertion
W_R	Energy released by crack formation
x	Position of start of steady needle penetration
x'	Position of end of steady needle penetration
ξ	Compliant needle grind angle
ξ_c	Conical grind angle
ξ_1	Primary bevel angle of the needle
ξ_2	Secondary bevel angle of the needle
y	Axis initially normal to major bevel angle

y'	Axis normal to major bevel after rotation
z	Distance from needle tip
z_l	Total length of needle tip

ACKNOWLEDGEMENTS

First and foremost, I would like to thank Dr. Jason Moore for all the help he provided over the last four years as my research advisor. I truly learned a great deal on all aspects of research from modeling to design of experiments to technical writing to being a good mentor. I would also like to thank Dr. Mary Frecker, Dr. Scarlett Miller, Dr. Zoubeida Ounaies, and Dr. Siyang Zheng for serving on my committee and providing valuable feedback. I would also like to thank Dr. Yuan-Shin Lee of NC State University for added guidance on my research and manufacturing needles used in this study.

I would like to thank Mr. Bill Genet who helped me on countless occasions to manufacture parts in the Learning Factory. The research conducted would have taken twice as long without his expertise. I would like to thank all the graduate and undergraduate members of the PMIDL who I had the privilege to work with over the last four years. Their help over the years has been invaluable.

I would like to thank the National Science Foundation. This material is based upon work supported by the National Science Foundation under Grant No. CMMI-1404916.

Finally, I would like to thank my family for all their support not just over the last four years but my entire life. The love of my parents and sister led me to and through this pursuit. Last but certainly not least, thank you to my fiancée Hannah for all her patience, understanding, and love. It was certainly not easy but we did it.

Chapter 1

Introduction

Needles are instruments frequently used in medical procedures. It is estimated 16 billion needle injections are performed worldwide annually [1]. They are utilized in procedures such as blood sampling [2], drug delivery [3], local and regional anesthesia [4], tissue biopsies [5], and brachytherapy cancer treatment [6]. For the procedures of biopsy and brachytherapy, the location of the needle in the body is very important [7, 8]. Brachytherapy, commonly used to treat prostate cancer, is a treatment where radioactive seeds are placed in precise locations inside the body. Misplacement of radioactive seeds can cause medical complications including urinary and bowel incontinence, rectal bleeding, erectile dysfunction, and tissue damage [9-11]. Biopsies require accurate placement of the needle to acquire a tissue sample in the desired region to test for diseases. False negative diagnoses can happen if the needle tip is not precisely located [12-14]. Accurate needle placement is a challenge because both the thin needles and the soft tissue deform as needle cutting forces are introduced.

Prostate brachytherapy is an example procedure where high needle placement accuracy is necessary for success. Prostate cancer is the most commonly diagnosed cancer in men. In 2013, an estimated 239,590 new cases of prostate cancer were diagnosed in the United States [15]. In permanent seed prostate brachytherapy, 50-70 radiation seeds are inserted into the body in and around the cancerous prostate tissue by thin gauge needles [16, 17]. The needles are generally pyramidal or bevel tipped as shown in Figure 1-1. These needles are inserted by hand in a precise pattern according to the treatment plan. With this procedure, seed accuracy of 2 to 3 mm is obtainable with guidance from high resolution ultrasonic imaging [18]. Greater accuracy is difficult

to achieve due to further needle positioning leading to edema (swelling of tissue) that can alter the anatomy and cause seeds to shift positions post operation [19]. This poor accuracy causes many doctors to implant more seeds than necessary to ensure adequate coverage [11], but this higher than necessary radiation can lead to complications [16, 20]. Therefore, higher precision is desired to improve the procedure efficacy and patient quality of life.

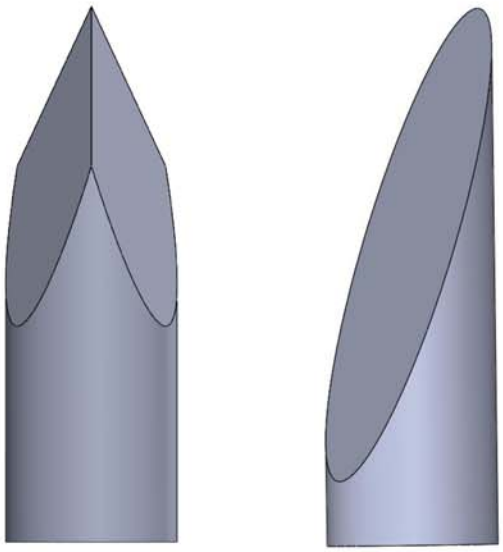

(a) (b)

Figure 1-1. (a) Standard three-planed symmetric pyramidal needle tip and (b) one plane bevel needle tip.

Accurately positioning the needle in the body has proven difficult with standard medical equipment. Needles can bend upon insertion due to the forces of interaction between the tissue and the needle [21, 22]. This leads to the needle tip missing the target location inside the body, as can be seen in Figure 1-2(b). Inaccuracy also comes from the tissue deflecting away from the needle as shown in Figure 1-2(c). Since, the tissue is free to move the target can easily become displaced upon needle insertion. Lower insertion force has been shown to reduce needle bending and tissue deflection [23-25]. In addition, lower insertion forces have been shown to reduce the pain felt by

patients during procedures [26]. There is a need to reduce the forces on the needle and the tissue upon insertion to reduce bending and deflection of the needle as well as increase the comfort of the patients. Many methods have been explored by researchers to reduce the insertion forces.

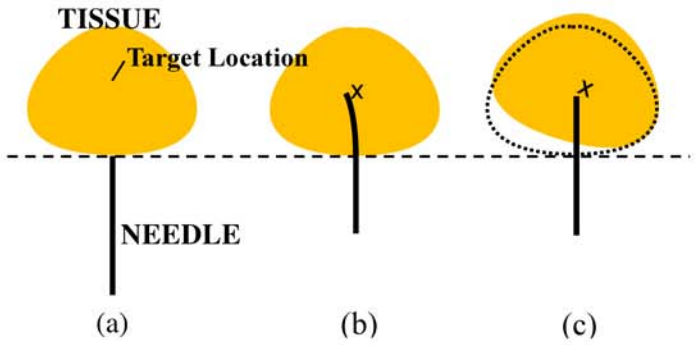

Figure 1-2. Needle shown (a) before insertion, (b) bending as a result of insertion forces, and (c) deflecting the tissue as a result of insertion forces.

Needle Geometry Methods

The insertion force of the needle can be reduced by altering the tip geometry. The needle tip geometry can be described by oblique cutting geometry used in traditional manufacturing [27]. The geometry of needle tips has been studied to determine how geometry relates to insertion force; more specifically, effects of cutting edge angles of the needle tip on insertion force were investigated [28, 29]. By altering the needle tip geometry, the needle can cut with less force [30, 31]. The standard hypodermic needle, which is commonly used for drug delivery, blood donation, and epidurals, is a three plane bevel needle as shown in Figure 1-3. Work has been done to study the geometry of the hypodermic needle and to optimize the grind angles to achieve a more efficient cutting geometry [32, 33]. Five plane bevel needles, being used for insulin injections, have an

efficient cutting geometry [34] that has been shown to cause less pain and cut with less force [35-37].

Figure 1-3. Standard three-planed bevel hypodermic needle tip geometry.

Another method to reduce needle insertion force is to use smaller diameter needles. For example, a 30 gauge needle (outer diameter of 0.311 mm) was shown to reduce patient pain compared to a 27 gauge needle (outer diameter of 0.413 mm) [26]. In addition, the insertion force needed to insert the needle was reduced by 20% [26]. To further reduce pain and insertion force, microneedles down to 100 microns in diameter are being developed. The microneedles have been shown to drastically reduce the insertion force [38-41]. Work is being done to use microneedles in drug delivery [42, 43]. However, vaccinations that require a large dose or have larger particulates cannot be passed through a small diameter needle, nor can brachytherapy seeds [44].

Insertion Speed Methods

The dynamic effects of insertion on cutting force, insertion speed and vibratory insertion, have been briefly explored in tissue cutting. For softer tissue, increased speed shows benefits. For example, Heverly et al. [45] have shown that with increasing the insertion speed of the needle, the force needed to puncture the tissue is reduced in porcine heart. Higher insertion speed was also shown to reduce insertion force in porcine liver samples [46] and turkey breast [47]. However, for tougher tissues such as skin, the reduction in force is not seen with higher velocity. Frick et al. [48] showed no velocity dependent effect on the insertion of suture needles into sheep skin and Koelsman et al. [49] showed needle insertion force into skin-like simulant increased 12% by increasing the speed from 100µm/s to 500µm/s. A velocity dependent model, such as the one presented in Chapter 2, is needed to describe the time dependent phenomena occurring in the needle-tissue interactions.

Applied Vibration Methods

Another dynamic insertion technique is vibration tissue cutting, where axial vibration is applied to needles to reduce insertion force. Vibration has been utilized in traditional manufacturing for many years. It was first proposed by Wood and Loomis in 1927 [50]. Since then, it has been refined and applied to machining many different materials and utilized in many different processes. Vibration is applied axially to a tool bit utilizing an actuator. An example setup can be seen in Figure 1-4. Many benefits arise when using vibration in manufacturing procedures. Work has been conducted utilizing ultrasonic vibrations to reduce and almost eliminate burr formation in drilling processes [51, 52]. This speeds up manufacturing because a second process to eliminate burrs is no longer needed. Another benefit to vibration cutting is a better surface finish [53, 54]. Balamuth [55]

has shown that surface finish of single point machining (lathe turning, milling, broaching) of metals can be improved by the addition of applied vibration. Chern et al. [56] found a smoother surface finish by applying vibration in boring operations. Another benefit of ultrasonic vibration is an increase in the allowed feed rate of machining, allowing for fast manufacturing [57]. The allowed feed rate of cutting is increased because vibration reduces the cutting and friction forces reducing heat generation and chatter. Finally, vibration cutting has been shown to reduce the cutting force required. Balamuth [55] showed reductions in cutting force of metals up to 80% by utilizing vibration. Wang et al. showed a reduction in cutting force in drilling fiber-reinforced plastics, where Pujana et al. used ultrasonic vibration to reduce the cutting force in titanium alloys [58, 59].

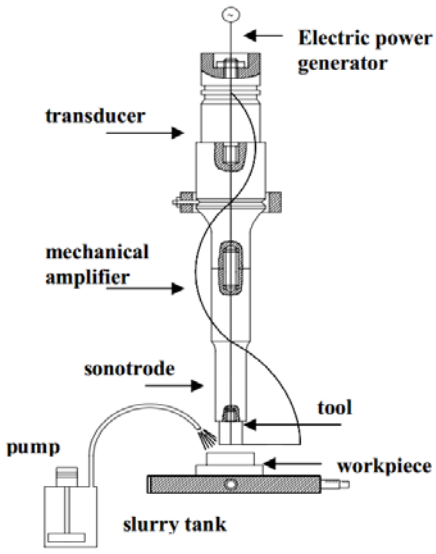

Figure 1-4. Schematic of ultrasonic vibration drilling [60]

With vibration cutting being used in traditional manufacturing for decades, there has been optimization of the parameters to achieve the best machining results. Ceyala et al. [61] explored how vibratory parameters affected surface finish, tool wear, and chip formation in turning processes

of mild steels. Mehbudi et al. [62] investigated the effect of vibration amplitude in drilling of GFRP laminates and found that higher amplitudes could reduce thrust force by up to 50%. Sadek et al. [63] explored vibratory parameters in drilling of fiber reinforced epoxy laminates and reduced the thrust force by 40% by optimizing the spindle rate, feed rate, amplitude, and frequency. By optimizing parameters, benefits can be gained by utilizing vibration cutting, especially in hard-to-machine materials. The use and benefits of vibration cutting in traditional manufacturing shows potential for using applied vibration to benefit needle tissue cutting.

Currently, vibration is used in some medical procedures to aid in cutting tissue. Alam et al. has shown that applying ultrasonic vibration to a tradition bone drilling bit, cutting forces were reduced [64]. Harmonic scalpel blades utilize ultrasonic vibration to cut and cauterize as the scalpel goes through tissue. Actuated Medical, Inc. (Bellefonte, PA) developed GentleSharp®, a commercial vibratory needle to aid in blood sampling. The device decreases the insertion force of the needle allowing for greater blood sampling and lower stress in the animals. However, the product is only for preclinical veterinary applications and laboratory research. More research on vibratory needle cutting is needed to develop a product for human use.

To further vibration tissue cutting, researchers are studying the effects of vibration on needle insertion. Yang et al. [65] showed a reduction of insertion force of microneedles by applying axial vibration to the needle. Axial vibration is vibrating the needle in the insertion direction as can be seen in Figure 1-5. Huang et al. [66] showed reduction in force of 27 gauge hypodermic needles by applying ultrasonic vibration with a piezoelectric actuator. Utilizing vibration, Izumi et al. [67] successfully designed a harpoon like jagged microneedle imitating a mosquito's proboscis to reduce insertion force. In order to optimize vibration tissue cutting, Begg and Slocum [68] tested the insertion force of lancet needles at varying frequencies and amplitudes. They saw a reduction in insertion force with applied vibration; however, discernable conclusions from their parameter study cannot be formed. The frequency and amplitudes tested in their study were coupled due to

the structural dynamics of the needles and test setup. Because of this, significant conclusions about the effects of either frequency or amplitude independently have on vibration cutting cannot be made.

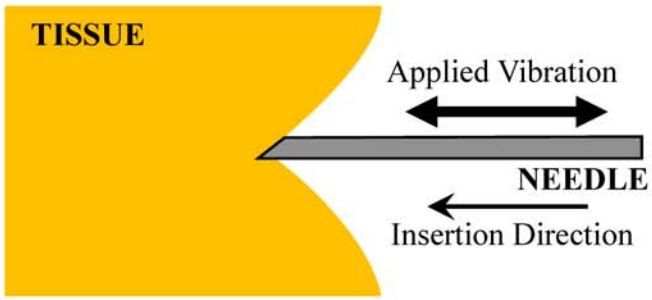

Figure 1-5. Diagram of the axial vibration applied to the needle.

Needle vibration has also been shown to improve needle position accuracy. Bi and Lin [69] showed vibration can be used to reduce needle deflection inside the body. They utilized a beam bending model in a dynamic system to determine the optimum frequency to apply to reduce deflection and saw a reduction of error (distance from target location) of 37% while applying a 15Hz vibration to a 2 mm/s insertion rate over a standard 2 mm/s insertion rate. Yan et al. [70] showed that by applying an ultrasonic axial vibration, the accuracy of needle location can be increased. They showed that target movement in gel tissue analogs was reduced with applied vibration compared to insertion without vibration. However, little work has been conducted to determine the effects of varying vibratory parameters of frequency and amplitude. In addition, the effect of geometry on vibration tissue cutting has yet to be explored by other researchers.

Research Motivation and Organization

In summary, due to insertion forces, current needles bend and deflect tissue upon their entry into the body. Because of this, the accuracy required in certain medical procedures is not met. Researchers have briefly explored reducing the insertion force by altering tip geometries [30-33], using smaller needles [26, 38-41], utilizing different insertion speeds of the needle [45-49], and applying an axial vibration [65-68]. However, fundamental research in understanding dynamic needle insertion and the effects of vibration tissue cutting has yet to be performed. In addition, vibration has only been applied to already in use needle geometries.

The purpose of this research is to study dynamic insertion forces of needles. An understanding of dynamic insertion will aid in developing novel methods to reduce insertion forces such that procedure efficacy and patient quality of life can be improved for needle based procedures. The main objectives of this research are as follows:

1. Create a velocity dependent force model that newly shows how tissue properties are affected by needle insertion at varying speeds.
2. Determine the effect varying amplitudes and frequencies have on the insertion force of needles.
3. Develop an understanding of how the geometry of the needle tip affects the performance of vibration tissue cutting.
4. Design and develop a novel needle geometry to utilize vibration to reduce the insertion force further.

To address these objectives, this dissertation is organized as follows. In Chapter 2, velocity's effect on insertion force is explored. A fracture mechanics based model is presented to explain the physical phenomena occurring when needles are inserted at different speeds. The experimental procedure in determining the model parameters is described as well as the results.

The model provides insight into tissue properties that are affected by varying the insertion speed and how these properties affect the cutting force. Chapter 3 explores how vibration can reduce the insertion force. First, experimental procedures are explained for determining the effects of parameters used in vibration cutting on standard hypodermic needles. Next, the relationship between geometry and vibration is explored. This chapter further extends knowledge on vibration cutting by determining how vibratory parameters and geometry affect insertion forces. Chapter 4 explores the development and performance of a novel compliant geometry. The compliant geometry is defined and finite element analysis was implemented to model the motion of the needle. Insertion experiments were performed to determine the effectiveness of the compliant geometry. The compliant geometry needle uses vibration to reduce insertion forces to improve the efficacy of medical procedures. Chapter 5 summarizes the findings, accomplishments, and significance of the work. It also presents the recommended future work based on the limitations of this study.

Chapter 2

Velocity Dependent Needle Insertion

Many techniques have been studied to decrease the force required to insert a needle into the body. One such way is to increase the speed of the needle entering the tissue. This chapter describes the methodology of understanding how the insertion speed and needle size influence the insertion force. Firstly, a background of needle insertion mechanics is discussed. Next, a physics based model is described and experimental procedures related to the model are detailed. Finally, results and discussion are presented. This chapter is based on a paper published in the ASME Journal of Manufacturing Science and Engineering [71].

Needle Insertion Mechanics

A needle passing through tissue experiences different phases of cutting. An example of these cutting phases is illustrated in Figure 2-1 where an 18 gauge hypodermic needle is passed through ex vivo bovine liver. In Phase 1, the tissue deflects and the force gradually rises. In Phase 2 the tissue is cut; an initial crack is formed, the crack is widened by the needle geometry, then needle passes through with friction acting between the needle and the tissue. In Phase 3, the needle continues to pass through the tissue and there is friction force between the outside of the needle and the tissue. If the needle passes through thick tissue there may be multiple deflection and cutting phases before the needle reaches its target location. The maximum cutting force is reached in Phase 2 and is defined as the total cutting force P, as shown in Figure 2-1. There are three forces associated with the puncture force of Phase 2: a cutting force P_c that tears the tissue forming a crack, the force P_s needed to spread the tissue apart to allow the needle through, and the friction P_f that acts along

the needle faces. These forces can be seen acting on the needle in Figure 2-2. The total cutting force P is the sum of these three forces as shown in Equation 1:

$$P = P_c + P_s + P_f \tag{1}$$

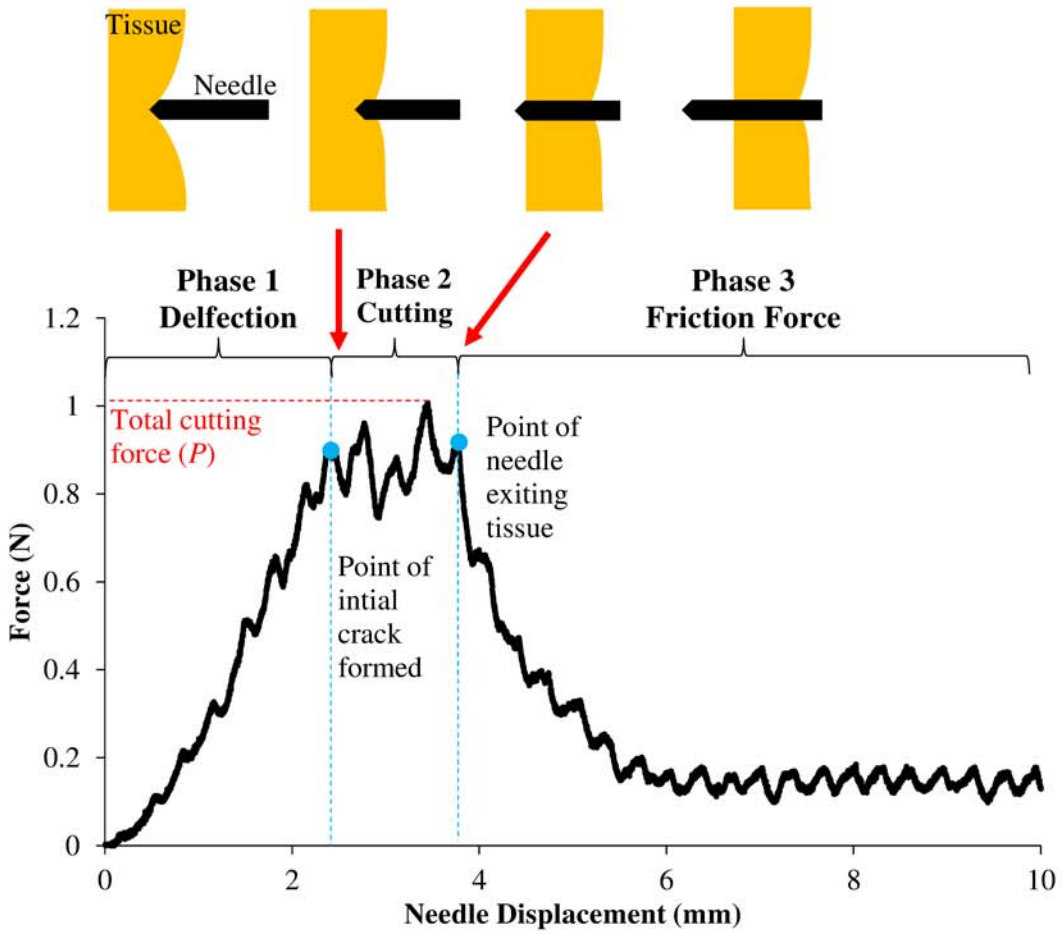

Figure 2-1. Insertion and friction forces with cutting phases illustrated above.

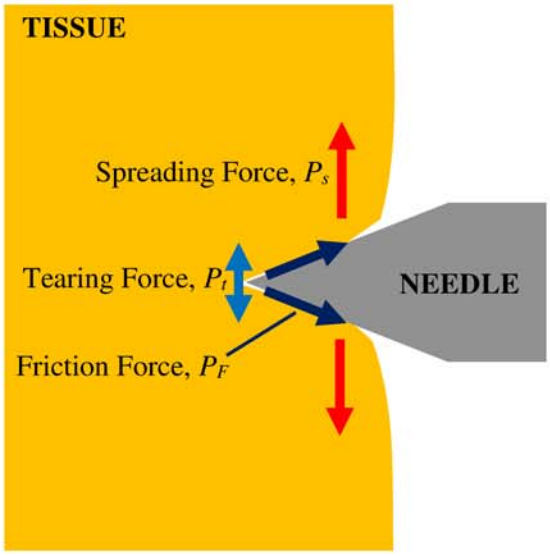

Figure 2-2. Forces acting at puncture.

Needle Insertion Force Modelling Background

To improve needle insertion, several physics and nonphysics-based models have been developed to predict insertion forces. Many models have been created to fit the insertion force profile without using any physical parameters to understand what phenomena are affecting the data [45, 72, 73]. For example Heverly et al. [45] described the final puncture force of a needle at varying speeds with a fitted equation, and Crouch et al. [72] developed a piecewise force model that fit logarithmic curves to experimental insertion data, describing the whole insertion. Other models explored incorporating mechanics of cutting into the models by exploring the forces acting on the needle [74-76]. For example, Dehghan et al. [74] utilized experimental data to determine cutting and friction forces and used those in an FEA model to determine tissue deflection. In addition, Okamura et al. [75] also determined cutting forces and friction forces from experimental data and utilized piecewise polynomials to describe each force. Approaching the problem differently, Roethuis et al. [76] utilized needle tip geometry to determine the insertion force and deflection of needles. These models broaden the utilization across different tissues and needle geometries by

incorporating friction force and puncture force acting on the needle. However, these models do not fundamentally describe how these forces are created.

To determine the cause of the cutting forces acting on needles, fracture mechanics-based models were developed. For example, Shergold and Fleck [77] developed a fracture mechanics-based model to describe the forces acting on the needle for quasistatic insertion, and is the basis of the model presented later in this chapter. Similarly, Mirsa et al. [78] utilized fracture mechanics concepts to determine the mechanics of steerable needles in tissues. Mavash et al. [79] developed a force model for dynamic insertion of needles by using tissue properties to build a modified Kelvin model to describe the tissue. However, dynamic insertion models have only briefly been developed.

Fracture-mechanics based approaches have been used extensively on metallic and ceramic materials because of the approach's ability to better predict when failure will occur [80, 81]. Recently, researchers have been applying fracture mechanics techniques to highly deformable materials including biological materials [82-84]. By measuring the energy to fracture tissue and moving a needle through the newly developed crack, a physics-based force model is constructed in this chapter. This model incorporates parameters including fracture toughness and shear modulus of the tissue. Because of the viscoelastic properties of the tissue, these factors are strain rate dependent, causing the speed of insertion to vary the insertion force.

Fracture Mechanics Model of Dynamic Needle Insertion

A tissue fracture mechanics model is formed dependent on needle diameter and insertion speed. As the needle inserts into tissue, work is performed equal to $P\delta l$ where P is the axial force exerted and δl is a differential insertion length. The needle then creates a crack in the tissue and spreads the tissue apart to accommodate the width of the needle. During cutting, there is friction between the needle and tissue as well. The work done by the needle is equal to the energy released

by the creation of the crack δW_R, the strain energy stored by the tissue spreading around the needle $\delta \Lambda$, and the work done by the friction on the needle $P_F(l) \cdot \delta l$, where the friction force is a function of insertion depth l. This relationship produces Equation 2:

$$P\delta l = \delta W_R + \delta \Lambda + P_F(l) \cdot \delta l \tag{2}$$

The work released by the generation of a crack in the tissue, δW_R, is:

$$\delta W_R(d,v) = J_{IC}(d,v)\ a(d)\ \delta l \tag{3}$$

Where $a(d)$ is the length of the crack generated in meters, $J_{IC}(d,v)$ is the mode-I fracture toughness of the tissue in units J/m^2, d is the outer diameter of the needle in meters, and v is the insertion speed of the needle in m/s. Kinetic energy was neglected in the development of the model due to its contribution in the work-energy equation being in the range of micro-Joules when a relatively small mass of tissue is acted upon.

The strain energy $\delta \Lambda$ associated with the spreading of the tissue is modelled as spreading a circle with an initial radius $r = 0$ to final radius $r = r$. With a plane strain assumption, this reduces to:

$$\delta \Lambda = \tfrac{1}{2}\, \pi\, \mu(v)\, r^2\, \delta l \tag{4}$$

However, the crack around the needle is not completely circular [82]. Because of this, a nondimensional contact factor $f_c(d)$ needs to be added into the $\delta \Lambda$ term. Combining the constants into the contact factor term, Equation 4 then becomes:

$$\delta \Lambda = \mu(v)\, r^2 f_c(d)\, \delta l \tag{5}$$

Substituting Equations 3 and 5 into Equation 2 yields:

$$P(d,v)\ \delta l = J_{IC}(d,v)\ a(d)\ \delta l + \mu(v)\, r^2 f_c(d)\ \delta l + P_F(l,d,v) \cdot \delta l \tag{6}$$

The goal of this work is to be able to describe the maximum insertion force of the needle into tissue. The friction occurring at the maximum insertion force is the puncture friction force P_{FP}. This friction force is substituted into Equation 6. Assuming the tissue parameters do not change with depth and describing only the maximum insertion force, Equation 6 becomes:

$$P(d,v) = J_{IC}(d,v)\, a(d) + \mu(v)\, R^2\, f(d) + P_{FP}(d,v) \tag{7}$$

To determine the mechanical properties of fracture toughness J_{IC} and shear modulus μ, as well as the needle-tissue interaction components crack length a and puncture friction force P_{FP}, experiments were conducted as discussed in the Experimental Procedures section. The contact factor $f_c(d)$ is determined by fitting the model to the experimental data as discussed in the Results and Discussion section. For this model, only the diameter of the needle and the insertion speed were explored. The needles were inserted into the same tissue under the same conditions. The type of tissue, temperature of the tissue, and pre-stress of the tissue were held constant during this study.

Experimental Procedures

This section describes the experimental procedures utilized to determine mechanical properties needed to develop the force model. Two experimental procedures, Experimental Procedure 1 and Experimental Procedure 2, were carried out to determine the parameters utilized in the model as can be seen in Table 2-1. In Experimental Procedure 1 the fracture toughness, frictional force, and crack length were found by inserting a needle into tissue as discussed in the following subsections. In Experimental Procedure 2 the shear modulus of the tissue is measured. To determine how properties changed with needle size, four different hypodermic needle gauges were used and can be seen in Table 2-2. The needle sizes were chosen because they are commonly used sizes in medical procedures for drawing blood [85], IV's [86], fine needle aspirations [87, 88], and delivering vaccines [89, 90]. The needles (Becton Dickinson, Franklin Lakes, NJ) used were

BD PrecisionGlide™ needles (Part numbers 301629, 305127, 305167, 305196, and 305198) as shown in Figure 2-3(a). A model of hypodermic needle tip geometry is shown in Figure 2-3(b). Hypodermic needles are three-planed lancet bevel needles, meaning they are ground on three planes to yield a sharper leading point than a basic one plane bevel needle.

Table 2-1. Description of which tissue properties and needle tissue interactions are determined by the two experimental procedures used in this study.

Experiment Procedure	Tissue Properties	Needle Tissue Interactions
1	Fracture Toughness	Friction Force Crack Length
2	Shear Modulus	n/a

Table 2-2. Experimental Procedure 1 parameters used in study.

Needle Gauge	Needle Outer Diameter (mm)	Insertion Speed (mm/s)	Number of Trials
16	1.65	1, 20, 40, and 80	5
18	1.27		
21	0.82		
25	0.51		
27	0.41		

(a) (b)

Figure 2-3. (a) The four hypodermic needles used in this work and (b) a close up of the tip geometry.

The effect of insertion speed on tissue cutting parameters was also experimentally determined. In Experimental Procedure 1 each needle was inserted into the porcine skin at four different speeds, as shown in Table 2-2. This allowed for the determination of how tissue properties are sensitive to insertion speed. The speeds were chosen to encompass typical insertion speeds used during medical procedures. Needle insertions for epidurals have been shown to be between 0.4 mm/s to 10 mm/s [91]. Typical hand insertion velocities for brachytherapy treatment are 60 mm/s [92]. In addition, Heverly et al. [45] showed no improvement in insertion force for insertion speeds greater than 75 mm/s. In Experimental Procedure 2 the shear modulus was determined by stretching the porcine skin at 4 different strain rates (0.25, 1, 10, and 25 % mm/mm-s). In the following subsections, methods for determining model parameters are discussed.

Fracture Toughness

The first model parameter determined during Experimental Procedure 1 is the fracture toughness. The experimental setup shown in Figure 2-4(a) was developed to carry out the test. The setup uses a linear motor (Dunkermotoren, Bonndorf, Germany) to insert the needle into porcine skin. The porcine skin is mounted between two plates to have consistent boundary conditions across trials. A six-axis force sensor (ATI Industrial Automation, Apex, NC) records the force on the tissue. Needle position information was acquired from an encoder located on the linear motor. Porcine skin was utilized because it has been shown to be analogous to human skin by having similar stress-strain response and tensile strength [93]. Therefore, creating a force model for porcine skin would be beneficial to work being done on humans. The porcine skin, 4 mm thick, was obtained fresh from a local butcher and vacuumed sealed in bags to keep as fresh as possible without freezing and damaging the tissue. Each needle was inserted into the same section of the skin to reduce variance from one animal to another as well as variance from one part of the skin to another. Upon needle insertion, the needle goes through the entire thickness of the porcine skin as can be seen in Figure 2-4(b). The skin itself is unbacked. During testing, the skin was allowed to warm up to room temperature (21.1˚C) before running trials.

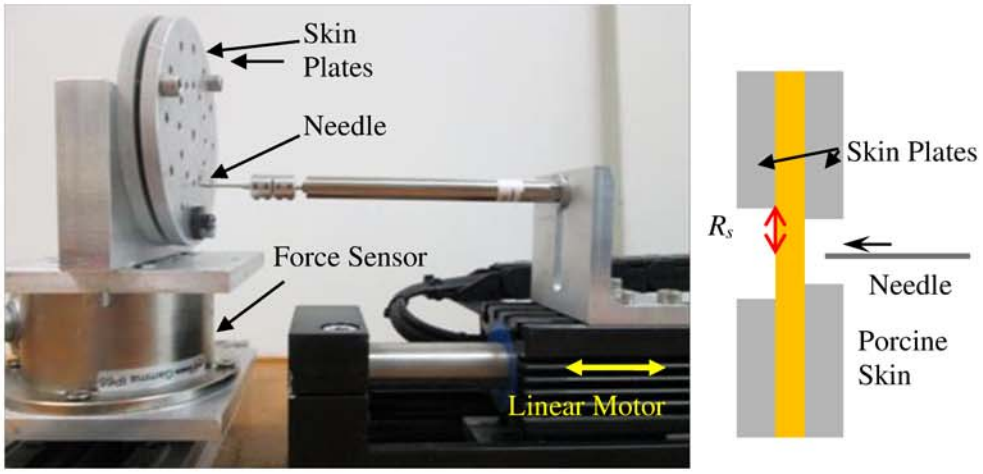

Figure 2-4. (a) Experimental setup for needle insertion and (b) the porcine skin mounting.

For each trial the needle was inserted through the porcine skin, tearing a hole into the skin, and then reinserted through the same hole. During the initial needle insertion, the total insertion force at puncture, P, is due to the fracturing of the tissue, the spreading of the tissue, and friction. In the second insertion the needle is inserted into the exact hole as before producing a force P'. Since the crack has already been formed in the first insertion, only the force from spreading the tissue and the friction remain as shown in Equation 8. Crack size was verified to be equal from the first insertion to the second using an optical microscope. Therefore difference between P' and P is the fracture force as shown in Equation 9.

$$P'\delta l = \delta\Lambda + P_F\delta l \tag{8}$$

$$(P - P')\delta l = J_{IC}a\delta l \tag{9}$$

Using the two insertions, the fracture toughness is extracted when the needle is under steady penetration during a portion of Phase 2, from x to x' as shown in Figure 2-5 (a). The region x to x' begins after the drop off in force after the initial puncture and ends before the relaxation of the tissue begins. The fracture work is the integral of the difference in force, P-P', with respect to

insertion depth. Fracture work versus crack area is shown in Figure 2-5(b). The crack area was calculated based on the measured crack width results, shown later in the section. The slope of this line yields the fracture toughness J_{IC}, shown in Figure 2-5(b).

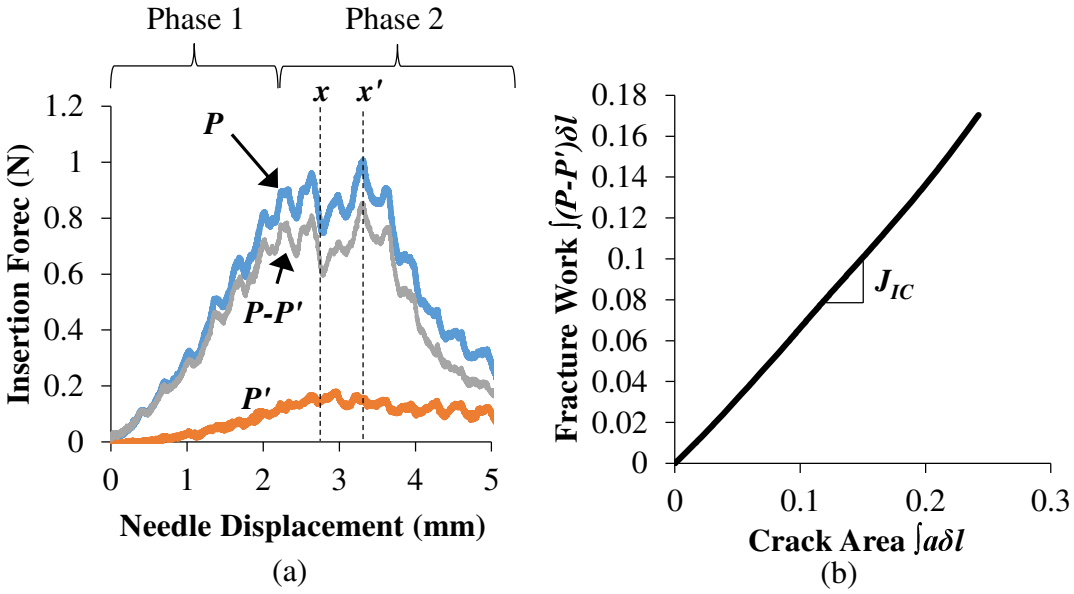

Figure 2-5. (a) Graph of double needle insertion with first insertion force *P*, second insertion force *P'*, and the difference and (b) graph of fracture work to determine J_{IC}.

Friction Force

Also utilizing Experimental Procedure 1, the puncture friction force P_{FP} was acquired during the needle insertion trials. Because the porcine skin has no tissue backing, after the fracture the force drops and levels off. The force occurring in Phase 3, as shown in Figure 2-1, is comprised only of friction force acting between the needle surface area and the tissue. At this point, no fracture or spreading of tissue is occurring. For this study, the friction measured during Phase 3 was approximated to be the friction occurring at the maximum insertion force during puncture. This

approximation was made because the friction during puncture is at its maximum value when the needle is in contact with the entire thickness of tissue, just as in Phase 3. Although the geometry of the needle in contact with the tissue varies between Phase 2 and Phase 3, the identical tissue thickness makes this an accurate approximation. The speed dependence of P_{FP} was determined through needle insertion experiments run at varying speeds.

Crack Length

The last model parameter acquired during Experimental Procedure 1 is the crack length. After needle insertion experiments were performed, the skin was inspected under an optical microscope. The crack length was then measured. An example tissue crack can be seen in Figure 2-6. The cracks were measured at the insertion side and exit side of the skin and then compared. Black ink was applied to the crack to allow for easier visual inspection of the crack length as shown in Figure 2-6.

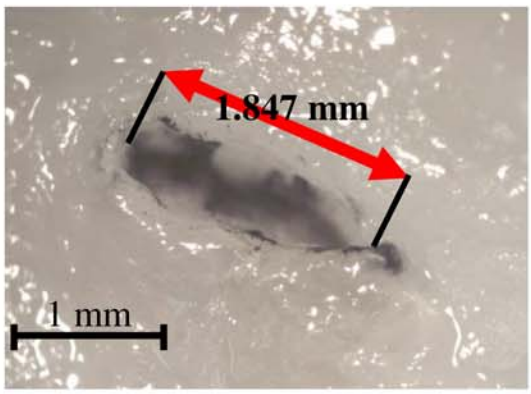

Figure 2-6. Example crack length.

Shear Modulus

Experimental Procedure 2 was utilized to find the shear modulus. The shear modulus was found experimentally by carrying out a tension test on the porcine skin. The experiment utilized the test setup seen in Figure 2-7. The skin was pulled at strain rates of 0.25, 1, 10, and 25 % mm/mm-s. Four trials were performed for each strain rate. The results of this experiment were analyzed with an Ogden model to determine the shear modulus and strain hardening properties of the tissue.

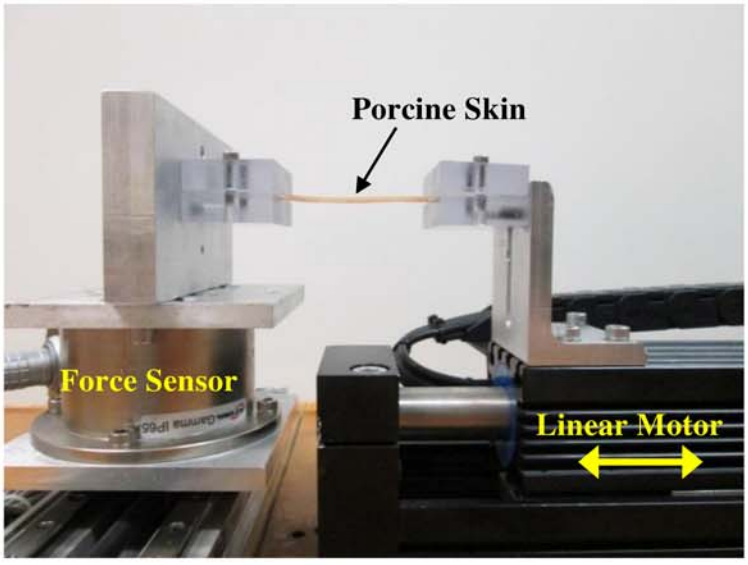

Figure 2-7. Experimental setup to determine shear modulus.

Porcine skin is viscoelastic and anisotropic [94, 95]. These properties come from the structure of the skin. The skin consists of stiffer collagen fibers and softer more flexible elastin as shown in Figure 2-8. The collagen fibers are naturally oriented in a certain direction (along Langer lines) due to the natural pretension of skin. When tensioned, the Young's modulus of the tissue is initially very low because the collagen fibers are moving about each other. Most of the initial stress occurs in the elastin fibers. At higher strains, the collagen fibers become aligned and the tissue

stiffens. This creates a J-shape stress-strain curve as shown in Figure 2-9. The shape of the stress-strain curve is dependent on the direction the skin is pulled. Figure 2-9 shows an example stress-stretch ratio of porcine skin stretched parallel, at a 45° angle, and perpendicular to the collagen fibers direction. These mechanics are strain rate sensitive as well [96]. Researchers have shown that most biological materials experience shear thinning, thus making it easier to deform them at high strain rates [97].

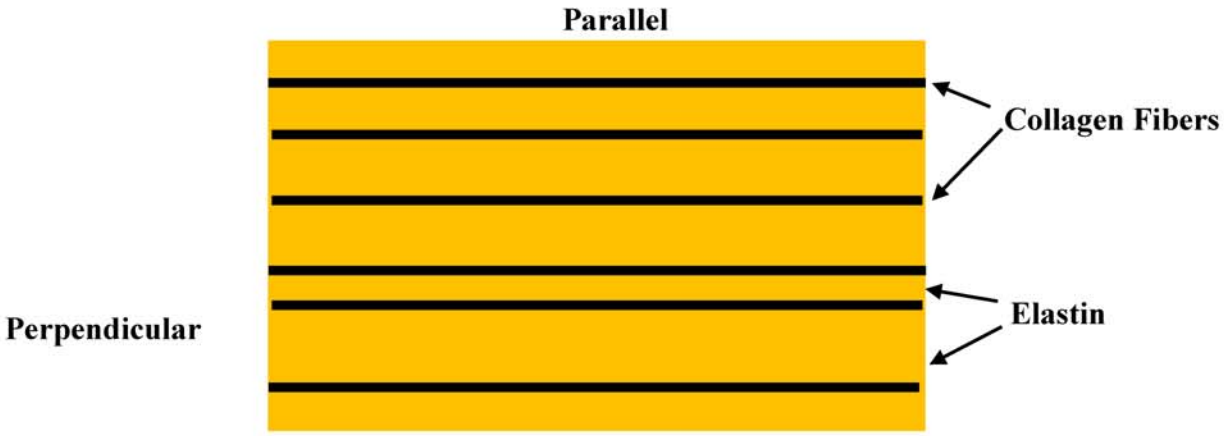

Figure 2-8. Diagram of collagen fibers and elastin of skin

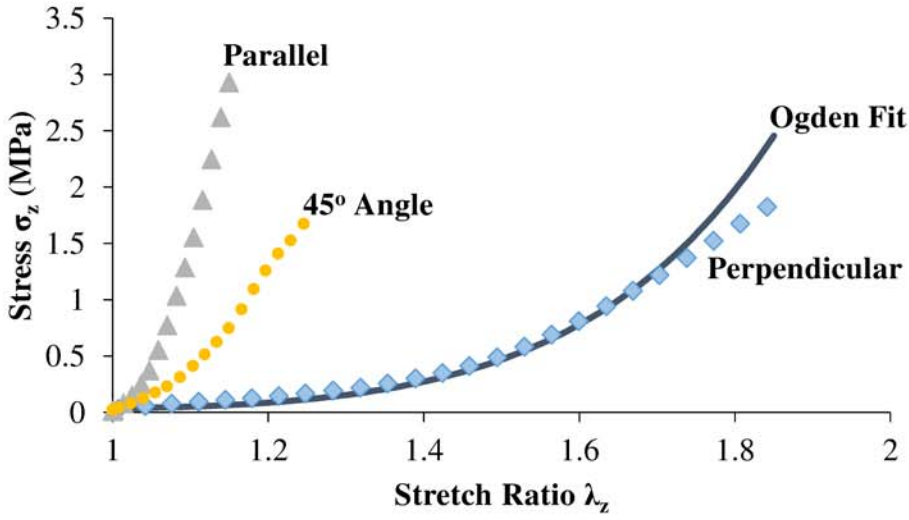

Figure 2-9. Stress-strain curve of the porcine skin parallel, at a 45° angle, and perpendicular (including Ogden Fit) to the Langer lines.

A sample response of the material with an Ogden fit can be seen in Figure 2-9. For this study, the shear modulus of the porcine skin perpendicular to the Langer lines was used. It is easier for a crack to travel along the collagen fibers than through them, similar to what occurs in bone tissue [98]. Thus, the tissue would then spread perpendicular to the Langer lines. The response can be described by the Ogden model for incompressible, isotropic, hyper-elastic solids. The fit is used to determine the shear modulus and strain hardening of the skin [99]. The Ogden fit can be written as:

$$\phi = \frac{2\mu}{\alpha_h^2}\left(\lambda_1^{\alpha} + \lambda_2^{\alpha} + \lambda_3^{\alpha} - 3\right) \tag{10}$$

Where ϕ is the strain energy density, μ is the shear modulus, α_h is the strain hardening, and λ_i are the principle stretch ratios. The one term, one dimension Ogden fit is utilized to determine μ and α_h:

$$\sigma_z = 2\frac{\mu}{\alpha_h}\left(\lambda_z^{\alpha_h - 1} + \lambda_z^{-1-\alpha_h/2}\right) \tag{11}$$

Where σ_z and λ_z are the stress and stretch ratio in the pull direction respectively. The Ogden equation is fit to the tension test data using least square regression to determine the shear modulus and strain hardening.

Results and Discussion of Experimental Procedures

This section discusses the experimental results from the two procedures performed. In addition, this section discusses the fits applied to the experimentally procured data and how the fits depend on velocity and needle diameter. The results are organized by first discussing each individual tissue property or needle-tissue interaction characteristic. The final model is then constructed and a validation case is presented.

Fracture Toughness

The results of the fracture toughness are shown in Figure 2-10, with five trials of each needle at each speed. As can be seen in the figure, the velocity of the insertion has little effect on the value. The diameter of the needle plays a major role in determining the fracture toughness. A third-degree multivariable (d and v) polynomial was fit to the data with an R^2 value of 0.95. The fit was third ordered across the needle diameters and first ordered across the speeds. The equation for the fitted surface is:

$$J_{IC}(d,v) = 1.305\times10^{4} - 3.582\times10^{7}\,d + 1.52\times10^{4}\,v + 3.389\times10^{10}\,d^{2} - 2.222\times10^{7}\,dv - 1.003\times10^{13}\,d^{3} + 8.006\times10^{9}\,d^{2}v \quad (12)$$

Where d is the outer diameter of the needle and v is the velocity of insertion. The variance increased for smaller needles because the steady cutting region used to calculate the fracture toughness was shorter due to the smaller needle tip.

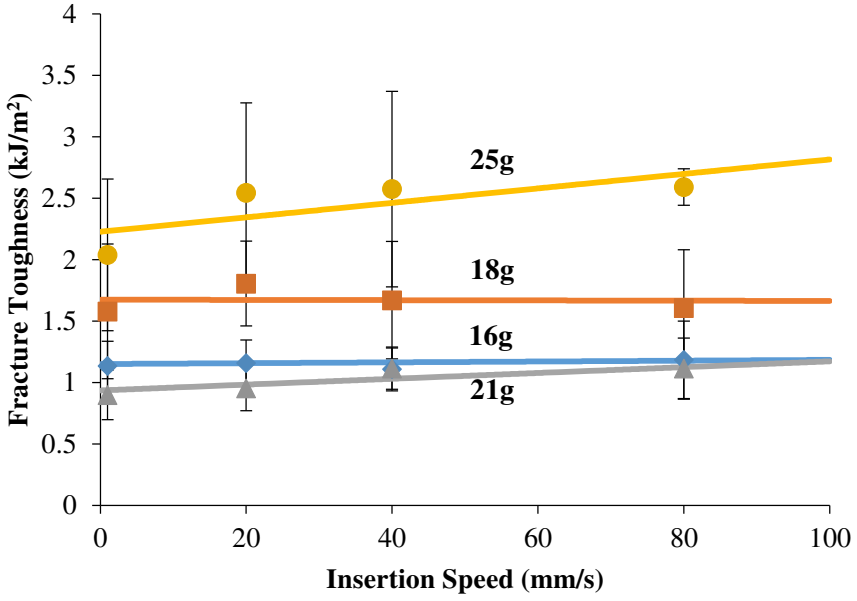

Figure 2-10. Two-dimensional fit of fracture toughness data where the points are experimental data and the line is the fit.

The fracture toughness relationship to needle diameter is not linear as has been found in other studies. For example Gokgol et al. found that the measured fracture toughness of round sharp punches (having conical tips) decreases linearly with increased diameter [100]. This study did not have this linear trend due to the hypodermic needle having a more complex shape than a round sharp punch. Hypodermic needles have three bevel angles that define their geometry: ξ_1, ξ_2, and β_1, as can be seen in Figure 2-11 [33]. The three angles were measured for all for needle gauges used in this study and the results are shown in Table 2-3. The different angled bevels of the different diameter needles may affect the fracture toughness results and cause the 21 gauge needle have lower fracture toughness than the 16 gauge needle. As seen in Table 2-3, both bevel angles, ξ_1 *and* ξ_2, are smallest for the 21 gauge needle.

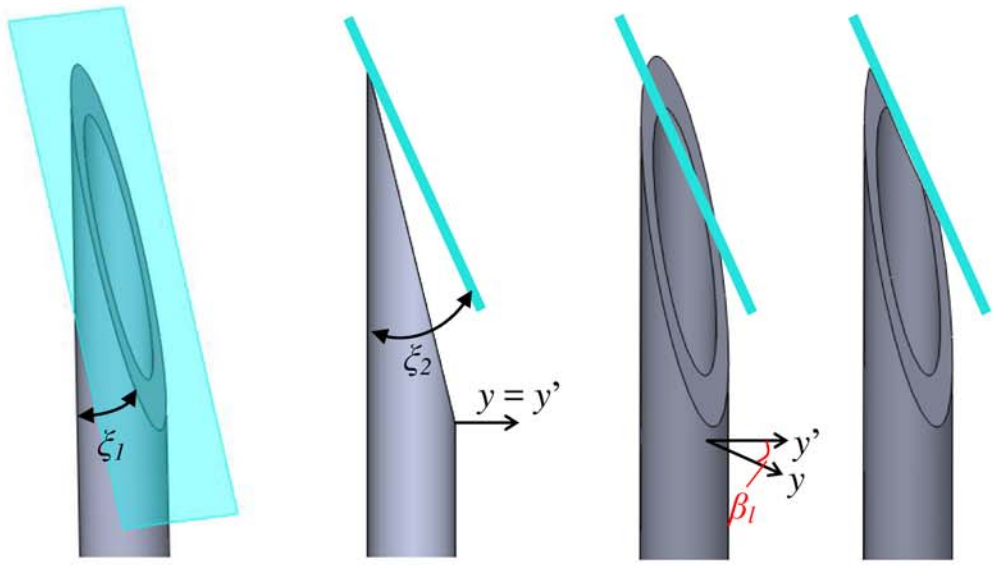

Figure 2-11. Definition of the three angles that define hypodermic needle geometry.

Table 2-3. Measured angles of hypodermic needles.

Needle Gauge	ξ_1	ξ_2	β_1
16	9.9°	17.5°	53.0°
18	10.6°	21.5°	48.5°
21	9.4°	16.0°	46.5°
25	9.6°	18.5°	43.0°

Past researchers have shown that different experimental techniques in measuring fracture toughness yield different results [101, 102]. Although fracture toughness is entirely a material property, the nature of biological tissues and other flexible materials cause them to be test dependent. The two most common tests for fracture toughness of biological materials are the trousers test and the scissors test. The trousers test involves cutting the test material in a rectangular strip, cutting a slit in the middle of the long end, and pulling the two "legs" apart, as can be seen in Figure 2-12. The scissors test works by cutting the test material with a pair of scissors and measuring the force and the length of cut. The scissors test generally yields lower fracture toughness due to the scissors concentrating the force more at the crack tip. In the trousers test, the pulling of the test material can round the crack tip, causing more energy to build up before the crack will propagate. The test method utilized in this work measures the fracture toughness in relation to needle puncture. This should yield the most accurate response to a needle inserting into the tissue and creating a crack.

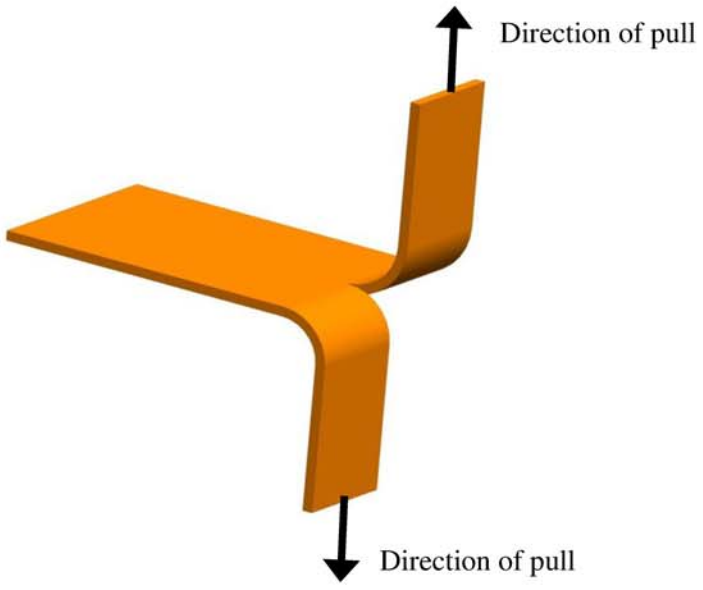

Figure 2-12. Diagram of trousers test.

Friction Force

The friction force was recorded and the results are shown in Figure 2-13. A two-dimensional fit was applied to the data is shown in Equation (13) with an R^2 value of 0.895. The R^2 value is somewhat low which will affect the accuracy of the frictional force component in the model. However, this fit is very simplistic, closely correlates to already existing friction models [46] and is appropriate for the high standard deviation in measured frictional values (13% on average). The high variance is caused by slight variations in the porcine skin.

$$P_{FP} = 0.1493 + 365.7d + 0.04463\ln(v) \tag{13}$$

Previous studies showed an increase in frictional force with increasing speed, as does the data gathered in this experiment [46, 75]. The friction model is closely related to that of Kobayashi et al. [46] where the friction increases logarithmically with increased velocity. The friction force also increases with increasing needle diameter. The puncture friction force also increases with increasing needle diameter which is to be expected. A larger needle size has more contact surface area and there is more pressure pushing the needle and tissue together.

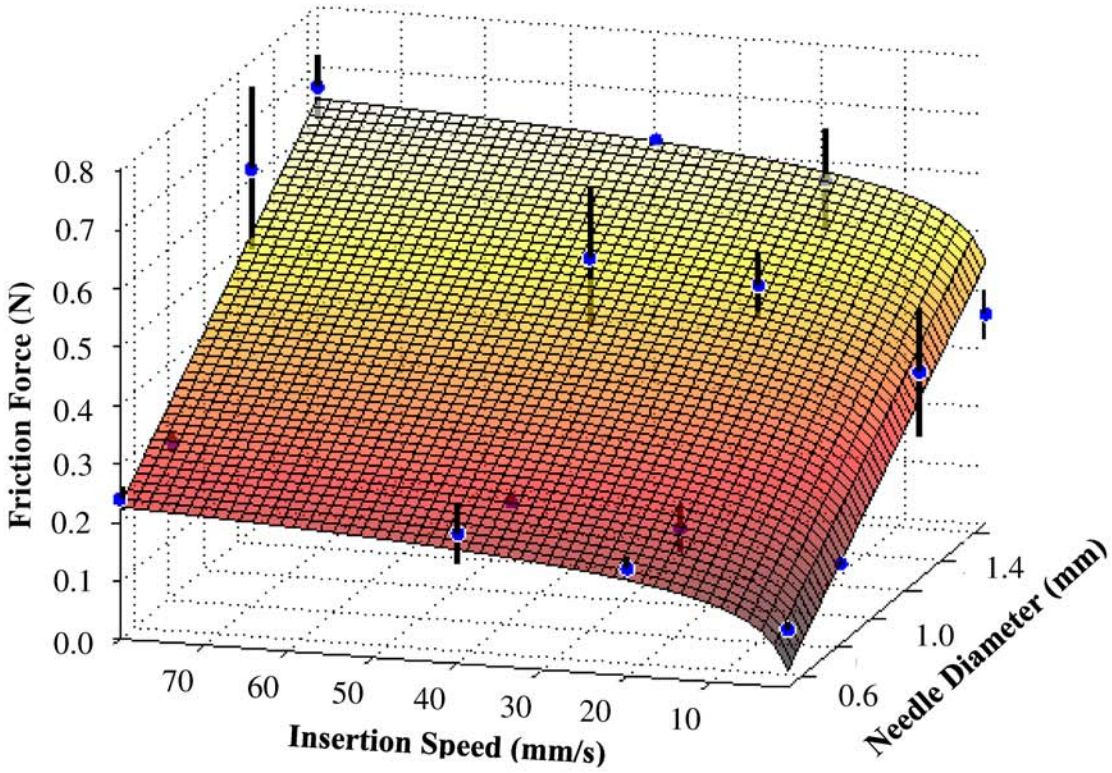

Figure 2-13. Two-dimensional fit of friction data where the points are the experimental data with standard deviation and the surface is the fit.

Crack Length

The crack length was measured for each of the five trials at each needle size. The results gave a linear trend with the crack size being slightly less than the diameter of the needle with an equation of:

$$a = 0.9052\, d \tag{14}$$

Where a is the crack length and d is the diameter of the needle in millimeters. The data is plotted in Figure 2-14 along with the standard deviation. The smaller crack size than needle diameter occurs because as the needle moves forward, the skin deflects and is stretched before the needle begins to

cut. The tissue deforms outward to accommodate the needle moving through as well. The crack does not run and keep enlarging because there are many mechanisms found in biological tissues to increase the amount of energy needed to continue fracturing material once a crack is formed. For example, the crack tip rounds due to the softness of tissues and fibers branch across the crack [97]. The standard deviation increases with the increasing needle diameter. This is due to the larger needle being in more contact with the nonhomogeneous skin.

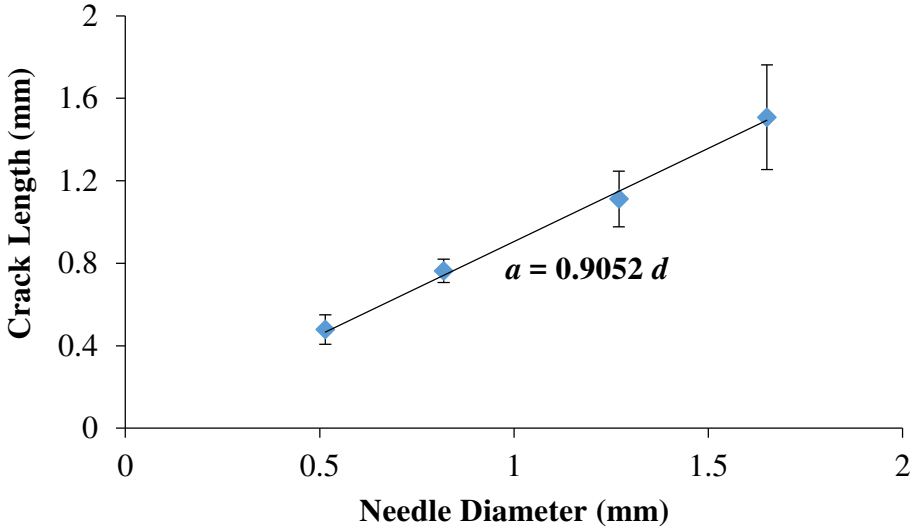

Figure 2-14. Crack Lengths with fit.

Shear Modulus

The shear modulus was measured at four different speeds for each of the 5 trials. The strain hardening and the shear modulus were computed from each trial. The shear modulus results and standard deviation are shown in Figure 2-15. The standard deviation increased as the strain rate increased. This occurs because more movement of the inhomogeneous tissue will result in higher

variation in force results and therefore higher variation in the calculated shear modulus. An equation was fitted to the data presented in Figure 2-15:

$$\mu = -6101\ln(\dot{\varepsilon}) + 87024 \tag{15}$$

Where μ is the shear modulus and $\dot{\varepsilon}$ is strain rate of insertion in mm/mm-s. The shear modulus decreased as the strain rate increased, confirming that the porcine skin shows shear thinning. The shear modulus values are similar to others in literature [96, 103].

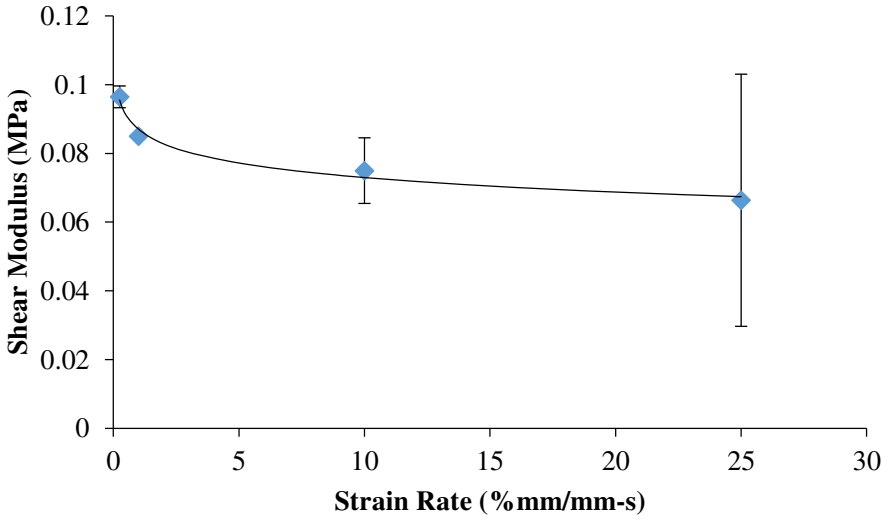

Figure 2-15. Shear modulus data with fit.

To determine the strain rate induced by the needle insertion, it was assumed that the tissue strained perpendicular to the insertion direction. The strain rate of the tissue is proportional to the insertion speed of the needle by the following equation:

$$\dot{\varepsilon} = \frac{v\tan(\alpha)}{R_s} \tag{16}$$

Where v is the insertion velocity, α is the bevel angle of the needle, and R_s is the radius of the hole in the back plate holding the skin, as can be seen in Figure 2-4(b).

Contact Factor

The contact factor f_c was found by fitting the insertion force model, Equation 7 to the experimental force results. The contact factor was found for each needle gauge size separately using a best fit least-squares regression. The results for the contact factor are shown in Figure 2-16 and were shown to decrease with increasing diameter based on Equation 17.

$$f_c = 17.534\, d^{-0.542} \tag{17}$$

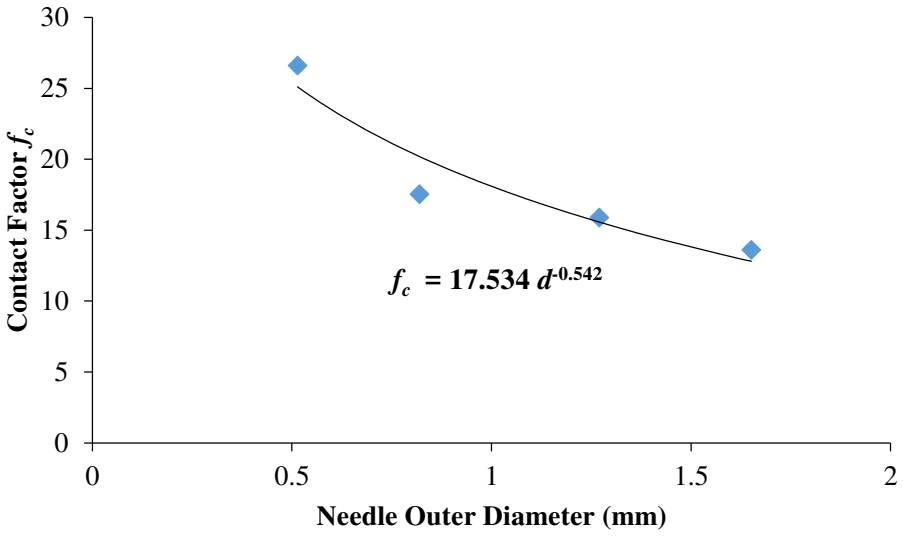

Figure 2-16. Contact factor f_c versus needle outer diameter.

Force Model and Validation

The completed force model, Equation 7, with the values of $J_{IC}(d,v)$ (Equation 12), $a(d)$ (Equation 14), $\mu(v)$ (Equations 15 and 16), $f_c(d)$ (Equation 17), and $P_{FP}(d,v)$ (Equation 13) incorporated is shown in Figure 2-17 with the experimental results. The model for each needle gauge is within one standard deviation of the experimental data with the largest error being 6.6% for the 21 gauge needle. Equation 7 can be used to determine the portion of the total insertion force

represented by each of the three forces acting on the needle as given by Equation 1. The tearing force, P_t, is given by $J_{IC}(d,v)a(d)$, the spreading force, P_s, is given by $\mu(v)r^2f_c(d)$, and the puncture friction force is P_{FP}. On average across the four needle sizes and insertion speeds, the tearing force accounts for 70% of the total insertion force, the spreading force accounts for 13%, and the friction force accounts for the remaining 17%.

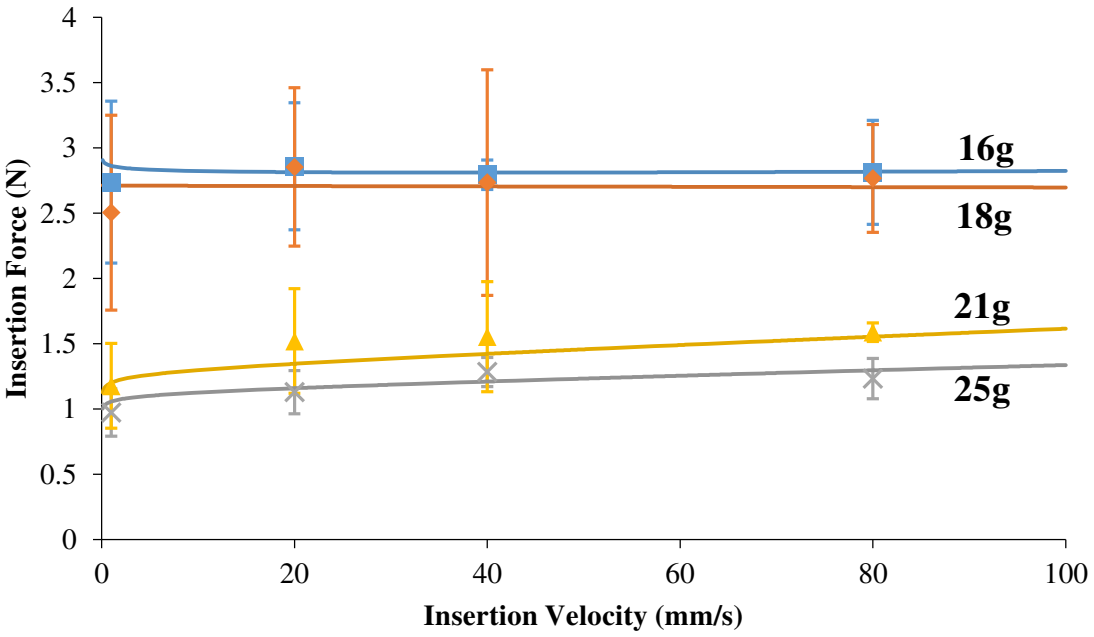

Figure 2-17. Force model (lines) plotted against experimental data (points).

To validate the force model, a 27 gauge hypodermic needle was tested. The needle's outer diameter is 0.41 mm and was inserted five times at each insertion speed as shown in Table 2-2. The experimental results is shown in Figure 2-18 along with the model's prediction. The over prediction of the model is attributed to the complex third degree fit of the fracture toughness overestimating the fracture toughness outside the range of needles tested. However, the model is still within one standard deviation for each data point with the model's greatest error from the experimental data being 13.7%. The standard deviation for the 27 gauge needle was 20.3%, similar to the percent

deviations of the other four needle gauges (14.5%, 24.4%, 13.6%, and 21.4% for the 16 gauge, 18 gauge, 21 gauge, and 25 gauge respectively). The 18 gauge and 25 gauge needles had the highest standard deviations in total insertion force. The two needles also had the highest values of fracture toughness corresponding to them. The high fracture toughness caused higher forces in fracturing the tissue, causing higher variation in the total insertion force.

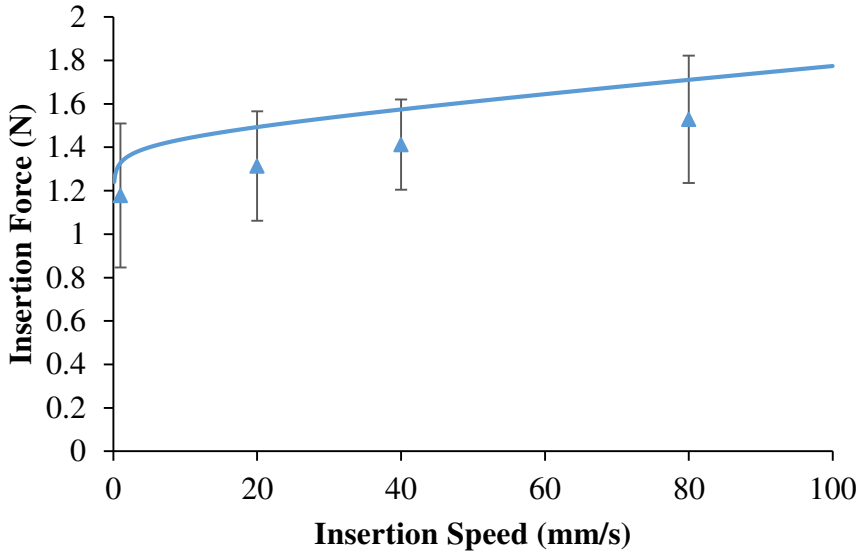

Figure 2-18. Completed force model (lines) plotted against experimental needle insertion force result (points) for 27 gauge needle.

Conclusions

A dynamic physics-based model was constructed and shown to accurately model insertion forces upon needle insertion into porcine skin for four different gauge hypodermic needles within 6.6% of experimental data. The model then predicted within one standard deviation the insertion force of a fifth hypodermic needle. The model shows that on average, 70% of the total insertion force comes from creating the crack. Friction contributes 17% of the total force and the spreading of the tissue contributes 13% of the force. For porcine skin, increasing the insertion speed did not

lower the insertion force, which can be explained by the decomposition of the total cutting force. From the experimental results, it is evident that fracture toughness, the majority of the total force, is relatively constant across different insertion speeds. Increasing speeds were shown to benefit in reducing the spreading force of the tissue. However, this benefit was offset by the increase in friction force caused by increasing the insertion speed. The spreading and friction forces were shown to contribute similar percentages (13% and 17% respectively) of the total force.

This model describes how tissue properties are dependent on the insertion speed of the needle. By decomposing the total force into component forces, the model is able to describe how these velocity dependent properties contribute to the total force, a novel attribute of the model. The model parameters experimentally obtained are specific to a hypodermic needle being inserted into ex vivo porcine skin. However, future work can expand this model by experimentally determining new model parameters. These new specific model parameters could then be applied to determine the optimal insertion speed for specific procedures.

Chapter 3

Vibratory Needle Insertion of Fixed Geometry Needles

This chapter describes work conducted to further understand vibratory cutting of tissue with fixed geometry needles. Experiments are presented that show how the vibratory cutting parameters of frequency and amplitude influence needle insertion force. This is based on a conference paper presented at and published in the proceedings of the 2014 ASME International Manufacturing Science and Engineering Conference [104]. Next, experiments are presented that illustrate how blunt hypodermic needle geometry cuts tissue under vibration. This study utilizes vibration to improve the performance of a blunt needle in hopes of reducing accidental needlestick injuries. This is based on the paper presented at and published in the proceedings of the 41st North American Manufacturing Research Conference [105]. Finally, a study is performed to determine how fixed geometry coupled with vibration effects insertion forces. This study is performed to aid in the development of novel needle geometries to be used with vibration. This work is based on a journal paper submitted to Proceedings of the Institution of Mechanical Engineers, Part B: Journal of Engineering Manufacture.

Vibratory Parameter Study

As discussed in Chapter 1, vibration has been utilized to reduce insertion forces of needles into tissue [65-68]. However these studies did not determine the effect vibratory parameters have on insertion forces. This study experimentally explores the effect vibratory amplitude and frequency have on the insertion force. This section describes the experimental procedure utilized in the study, presents the results, and discusses the findings.

Force Measurement Experimental Setup

The following subsections describe the insertion force measurement method. First, the experimental test setup used to record the data as well as the needles utilized in the test is discussed. Next, the design of the experiments and the parameters varied during the test are discussed. Lastly, the insertion mechanics of the hypodermic needle into tissue is presented and the insertion force is defined.

Needle Insertion Testing Apparatus

An experimental setup was devised to determine how vibratory parameters affect insertion force. The experimental setup shown in Figure 3-1(a) utilizes a linear motor (Dunkermotoren, Bonndorf, Germany) to insert the needle into the porcine skin at a constant rate. Mounted to the slide is a piezoelectric actuator (Physik Instrumente, Karlsruhe, Germany) that has a maximum travel length of 90 microns. The piezo actuator provided the vibration during the tests. The force was measured with a six-axis force sensor (ATI Industrial Automation, Apex, NC) mounted on an adjacent table to isolate it from the vibrations. A data acquisition system (National Instruments, PXIe-6361) and LabVIEW software were used to record force results and to control the linear motor and piezoelectric actuator.

Porcine skin was utilized as the testing medium, as researchers in the past have used it as an appropriate analog to human skin with similar stress-strain responses and tensile strengths [93]. The porcine skin was 4 mm thick and was clamped between two plates without tissue backing to hold it, as shown in Figure 3-1(b). The porcine skin was obtained fresh from a local butcher and vacuumed sealed in bags to keep as fresh as possible without freezing and damaging the tissue. The plates had twelve holes in them, allowing the needle to pass through the skin in 12 different

locations without applying any tension to the skin. The plates were mounted on the force sensor, as shown in Figure 3-1(a).

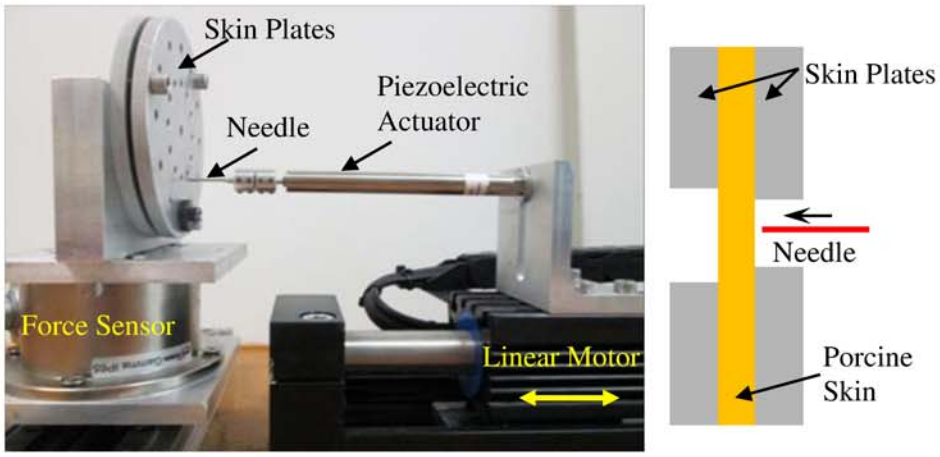

Figure 3-1. Experimental setup with (a) vibratory needle cutting setup and (b) diagram of porcine skin holder.

Four different sized hypodermic needles (Becton Dickinson, Franklin Lakes, NJ) were used in this study. Different sized needles were used to determine if needle diameter played a role in choosing the optimal parameters for vibration. The needles can be seen in Table 3-1 along with there outer diameters. These needles were chosen because they all are commonly used in medical practices, which can be seen in Table 3-1 as well.

Table 3-1. Gauges, sizes, and typical uses of the needles used in this study.

Needle Gauges	**Outer Diameter (mm)**	**Uses**
16	1.651	Blood Donation
18	1.270	IVs
21	0.8192	Fine Needle Aspiration
25	0.5144	Vaccines

Experimental Design

An experiment was designed to test the insertion force of hypodermic needles through porcine skin at various vibration frequencies and amplitudes to determine those parameters' effect on insertion force. The average velocity of the insertion was kept at a constant 1 mm/s, supplied by the linear actuator, for all the trials. This isolated the vibratory parameters as the factors the insertion force could be dependent on and is a typical insertion speed for needles inserted by hand [91]. The experiment used four different hypodermic needle gauges as referenced in Table 3-1. The needles were tested at 18 different combinations of amplitude and frequency, as listed in Table 3-2, with five trials at each combination. The needle was also inserted with no vibration as a control to compare the feasibility of utilizing vibration to reduce the cutting force. The combinations tested a broad spectrum of amplitudes and frequencies to better determine the effects of the vibratory parameters. The limits of frequency and amplitude tested were determined by the amount of power that could be safely put into the piezoelectric actuator. Having both high frequency and high amplitude requires a large amount of power be applied to the piezoelectric actuator. Excessively high electrical power will cause the actuator to generate large amounts of heat and break the piezoelectric ceramic.

Table 3-2. The experimental parameters of the 18 vibratory combinations.

		Peak-to-Peak Amplitudes (μm)			
		5	10	25	50
Frequencies (Hz)	100	#1	#2	#3	#4
	250	#5	#6	#7	#8
	500	#9	#10	#11	
	750	#12	#13		
	1000	#14	#15		
	1500	#16	#17		
	2000	#18			

Force and position data were collected for each trial. An example of the insertion force upon insertion is shown in Figure 3-2. The data was sampled at four times the vibration frequency to accurately measure the force. The insertion force was recorded at the point of puncture, as shown in Figure 3-2. Similar to the work conducted in Chapter 2, the point of puncture occurs at the beginning of the first Phase 2 of cutting. This successfully allowed the force and position to be recorded. The next step was to measure the amount of vibration being applied, which is discussed in the next section.

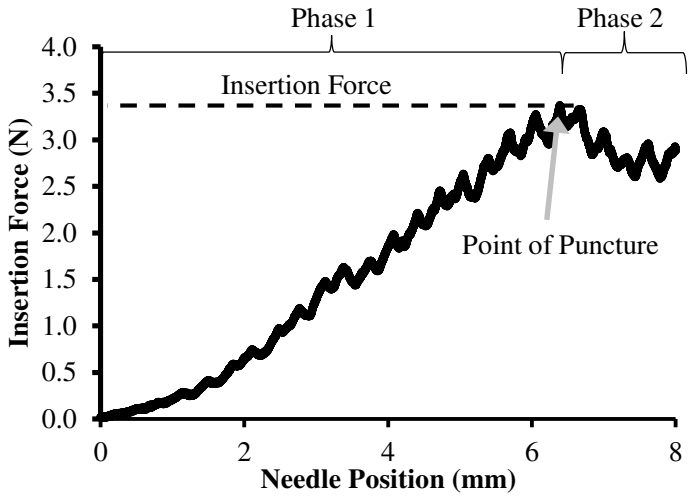

Figure 3-2. Example plot of needle force with cutting phases labeled.

Vibration Measurement Setup

The application of the vibration with the piezoelectric actuator is an open-loop system. During the trials, there was no feedback given to the actuator to ensure accuracy in positioning. Because of this, needle tip motion measurements were needed to obtain an accurate force map. The compliance in the system creates a difference in the input frequency and amplitude (the signal given

to the actuator) and the output frequency and amplitude (the displacement of the needle tip). The vibration measurement allowed insight into the frequency response of the system.

Vibration Measurement Apparatus

Due to the nature of the force measurement setup and the device used to measure the vibration, a separate experimental setup and procedure was needed to take the measurement. The experimental setup shown in Figure 3-3 is similar to the insertion force setup. The piezoelectric actuator is attached to the linear slide. The tip of the hypodermic needle is cut off and reflective tape is attached to the end. Isolated from the needle and slide is a fiber-optic probe (MTI Instruments Inc., Albany, NY) attached to a micrometer to finely tune the standoff distance. The probe measures the displacement of the needle in real time. LabVIEW software was used to record the displacement output and control the piezoelectric actuator to provide the vibration.

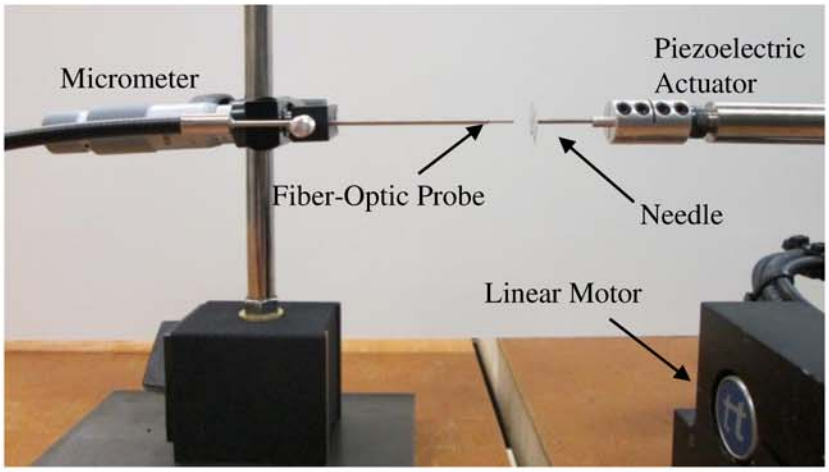

Figure 3-3. Experimental setup of vibration measurement system.

Experimental Design

The needle was vibrated at every frequency and amplitude combination utilized during the insertion force experiments, listed in Table 3-2. The fiber-optic probe measured the vibration of the needle tip. The displacement data was recorded for 100 periods. The data was then filtered with a 4th-ordered Butterworth filter to reduce the noise. The frequency and amplitude were recorded from the data, as shown in the example plot in Figure 3-4.

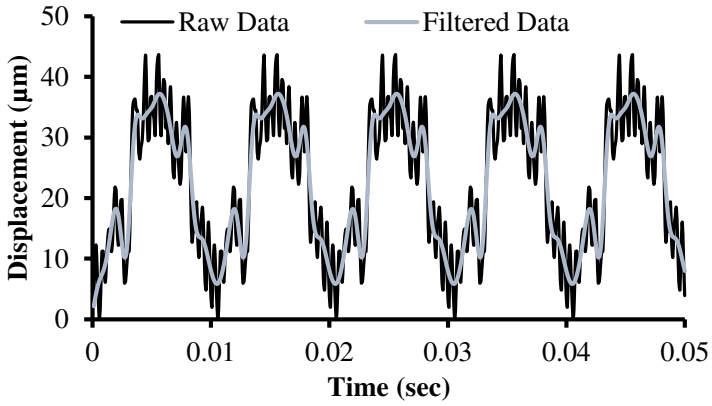

Figure 3-4. Plot showing the raw vibration data and the filtered data.

Results and Discussions of Force and Vibration Measurement Experiments

Results are presented from the vibration measurement experiment and force measurement experiment.

Vibration Measurement Results

The peak-to-peak amplitude and frequency were measured from the filtered vibratory measured results for each vibration parameter combination. The measured vibrational frequencies

at the needle tip were equal to the input waveform given to the piezoelectric actuator. The power supply and actuator were able to operate at the frequency ranges utilized in this study. However, the output amplitude varied from the input amplitude. To determine the frequency response of the system to the applied vibration, a normalized difference of the amplitude was taken and averaged over a certain frequency. The normalized difference was calculated by the following equation:

$$ND = \frac{A_o - A_i}{A_i} \times 100 \tag{18}$$

Where ND is the normalized difference, A_o is the experimentally measured output amplitude, and A_i is the theoretical input amplitude that was applied to the actuator. By normalizing the difference, the data was averaged across amplitudes at each frequency. For example, the normalized difference was calculated for all the amplitudes of trials run at 100 Hz. The four 100 Hz normalized differences were then averaged together to get the mean normalized difference for that specific frequency (100 Hz in this example). This provided insight to how the system performed at each individual frequency. This resulted in a frequency response of the test setup which can be seen in Figure 3-5. The results show that the system's output matches the input at low frequencies, but begins to deviate more as the frequency increases. There were four samples for the 100 Hz and 250 Hz frequencies, three samples for the 500 Hz and 750 Hz, two samples for the 1000 Hz and 1500 Hz, and one for the 2000 Hz. The higher deviation at 500 Hz would imply the dynamic response of the system is more unstable at that frequency, possibly near a natural frequency of the test system.

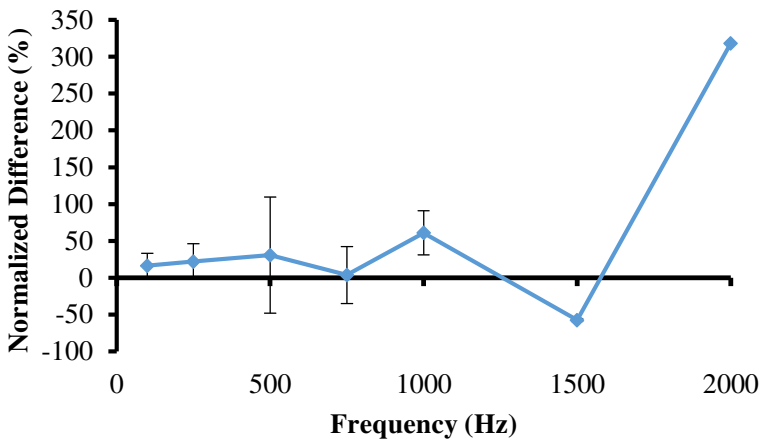

Figure 3-5. Frequency response of the test setup in terms of normalized difference with standard deviation.

The vibration measured in this study was conducted with the needle outside tissue in air. In practice, the needle is contacting the tissue and will therefore have a different response. The needle is attached to the piezoelectric actuator via a strong magnet. When force is applied to the needle (i.e. contacting the tissue), the magnet coupler provides a stronger connection causing the system to become stiffer. The needle's output amplitude inside the tissue is unkown. Due to this, all frequencies and amplitudes in the results are the input frequencies and amplitudes, not the measured results which is a limitation of this study.

Insertion Force Results

The results from the insertion force experiments were averaged across the five trials at each vibratory combination parameter. The results were then plotted against the amplitude and frequency of the vibration. A linear interpolation was conducted to map out the insertion force between data points. This was done for all four needle gauges separately. The results can be seen in Figure 3-6 through Figure 3-9 for needle gauges 16 through 25 (largest outer diameter to smallest),

respectively. The control insertion force (insertion with no vibration) is marked on the colorbar for reference.

The experimental setup promoted good repeatability of the data. It is common for experiments involving soft tissue cutting to have variability as high as 25% from trial to trial [29]. This is due to tissue being anisotropic. In addition, tissue properties vary from one animal to the next and even from one part of a single animal to another. The porcine skin was obtained fresh from a local butcher to have as consistent results as possible. All the trials for a specific needle gauge were performed on the same section of skin. The sections of skin, however, differed between the needle gauges. With this consistency, the average standard deviation for the trials was 23.49%, 18.96%, 14.63%, and 23.58% for the 16, 18, 21, and 25 gauge needles respectively.

The force maps in Figure 3-6 through Figure 3-9 shows regions of high and low force. The regions of high and low forces shifted towards higher frequencies as the needle diameter decreases. The maximum and minimum insertion force of each needle gauge was determined. There are regions on every map where the insertion force is less than the control insertion with no vibration as can be seen in Table 3-3, with approximately 30% reduction across the four needles. Table 3-3 also shows what vibratory parameter combination the minimum force occurred at. These combination numbers can be seen in Table 3-2.

Unpaired T-tests were performed on data comparing the insertion force at maximum reduction to the control insertion for each needle. For the 16 gauge needle, there was significant, $t(8) = 2.66$, $p = 0.03$, reduction in force of 30% with applied vibration ($M = 3.51$, $SD = 0.66$) over the control insertion ($M = 5.03$, $SD = 1.09$). The 18 gauge needle with applied vibration ($M = 8.07$, $SD = 2.38$) reduced the insertion force by a similar 33% over the control insertion ($M = 11.99$, $SD = 0.29$), also a significant amount, $t(8) = 3.66$, $p = 0.006$. The 21 gauge needle saw the least maximum reduction in force, 21%, with applied vibration ($M = 3.60$, $SD = 1.29$) over the control insertion ($M = 4.57$, $SD = 0.41$). Due to the high variance inherent in the tissue, this is not a

significant result, $t(8) = 1.60$, $p = 0.15$. Finally, the 25 gauge needle produced the greatest maximum reduction of force using applied vibration (M = 1.17, SD = 0.33) over the control insertion (M = 1.72, SD = 0.32). Vibration was able to reduce the insertion force significantly, $t(8) = 2.73$, $p = 0.03$, by 35%. In general, the trials with applied vibration had higher standard deviations than the control insertion.

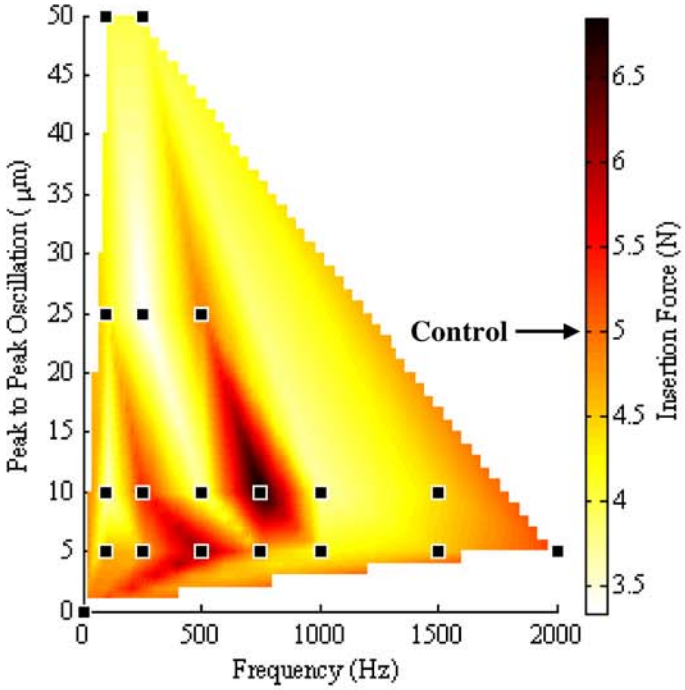

Figure 3-6. The insertion force map for 16 gauge needle.

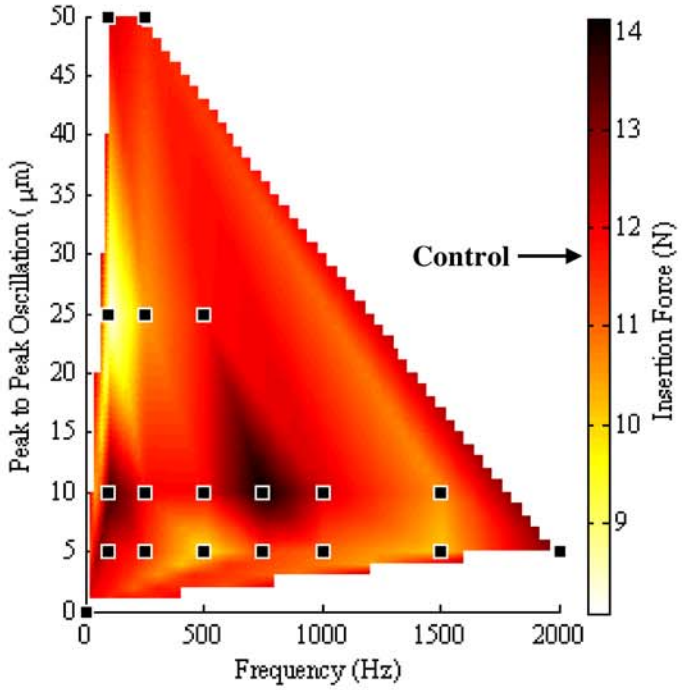

Figure 3-7. The insertion force map for 18 gauge needle.

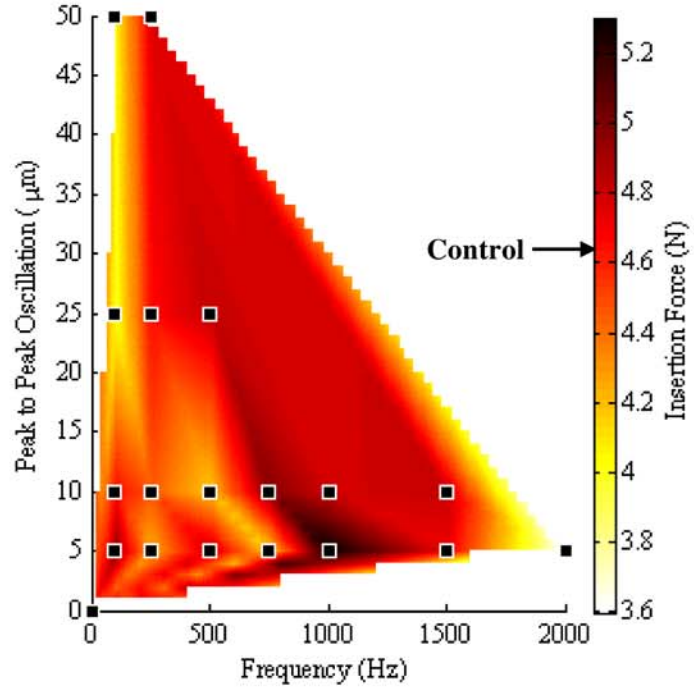

Figure 3-8. The insertion force map for 21 gauge needle.

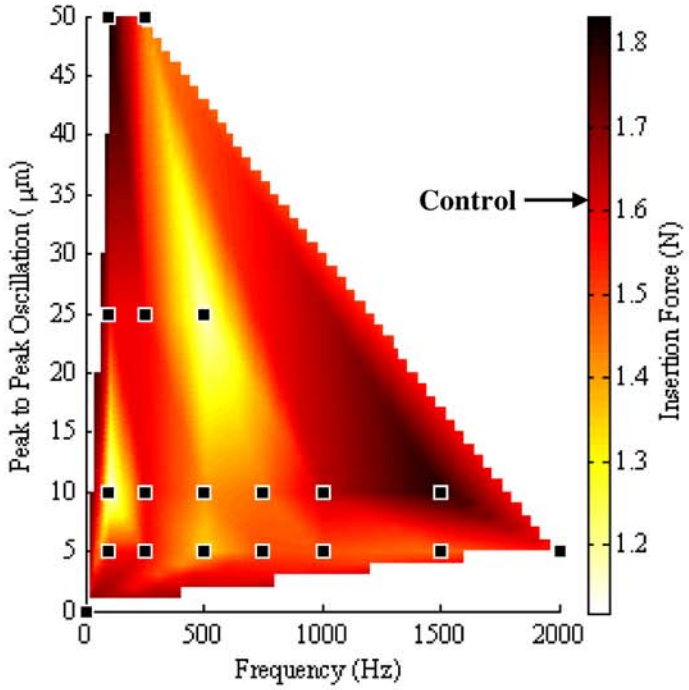

Figure 3-9. The insertion force map for 25 gauge needle.

Table 3-3. The insertion force reduction for each needle and for which combination they occurred.

Needle Size (gauge)	16	18	21	25
Percent Force Reduction	30.2%	32.7%	21.2%	35.0%
Combination Number	#2	#3	#10	#11

The maximum and minimum insertion force values occur at different frequencies and amplitudes for the different sized needles as can be seen in Table 3-3 and Figure 3-6 through Figure 3-9. To compare the needle gauges and vibratory parameters, the frequency and amplitude combinations were converted to relative insertion speed. Chapter 2 explored how insertion force

was dependent on the speed of insertion. One method of altering the speed of the needle is to apply vibration. The position of the tip of a vibrating needle can be expressed by the following formula:

$$Insertion\ Position = A_i \sin(2\pi f_i t) + v_o t \tag{19}$$

Where A_i is the applied input amplitude, f_i is the applied frequency, t is elapsed time, and v_o is the steady insertion speed. In Figure 3-10, two insertion profiles are plotted. The straight line is the position of a needle being inserted at a steady 10 mm/s. The oscillating line is the position of the needle being inserted at a rate of 1 mm/s with a 100 Hz frequency and 50 micron amplitude vibration. The vibrating needle's position on average lags behind the position of the 10 mm/s steady inserting needle, yielding a more controlled insertion. Calculating the instantaneous speed of the needles shows that the maximum speed of the vibrating needle is actually higher than the steadily inserted needle, as can be seen in Figure 3-11. The equation for maximum vibratory insertion speed is:

$$Maximum\ Vibratory\ \ Insertion\ Speed = 2\pi A_i f_i \tag{20}$$

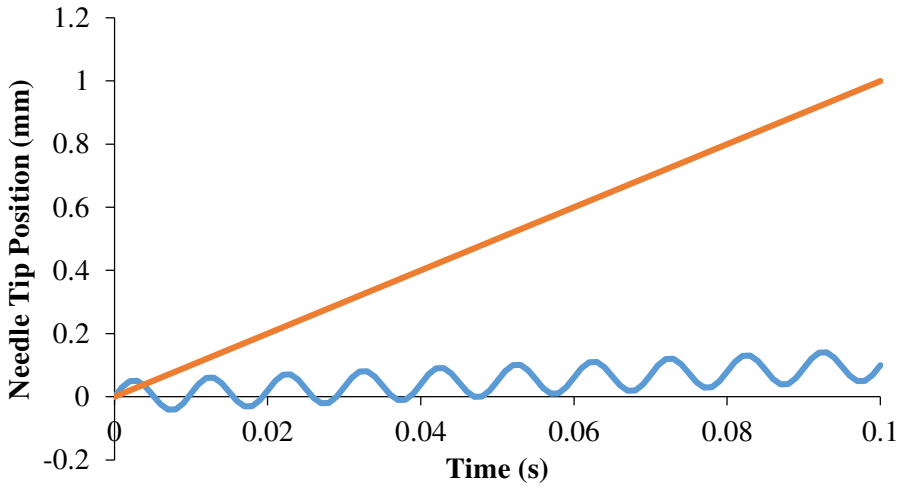

Figure 3-10. Needle tip position of a steadily inserted needle and a needle with applied vibration.

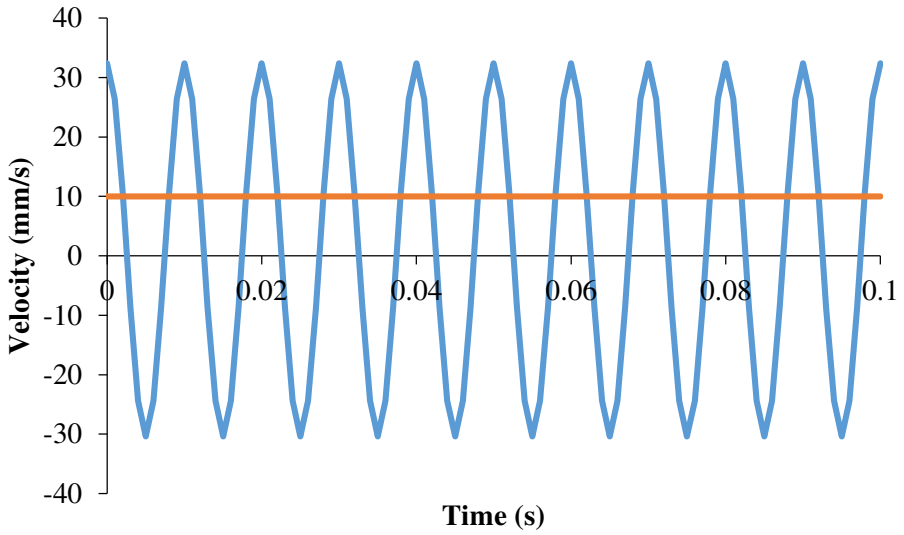

Figure 3-11. Needle tip velocity of a steadily inserted needle and a needle with applied vibration.

Since the needle is oscillating, the insertion speed is not constant throughout the trial. The insertion speed used for comparison in this work was the maximum insertion speed. Figure 3-12 shows the maximum vibratory insertion speed at each frequency and amplitude combination. The maximum and minimum insertion force for each needle diameter was plotted against the insertion speed in Figure 3-13. As shown, the larger the needle diameter, the lower the maximum vibratory insertion speed for the minimum force.

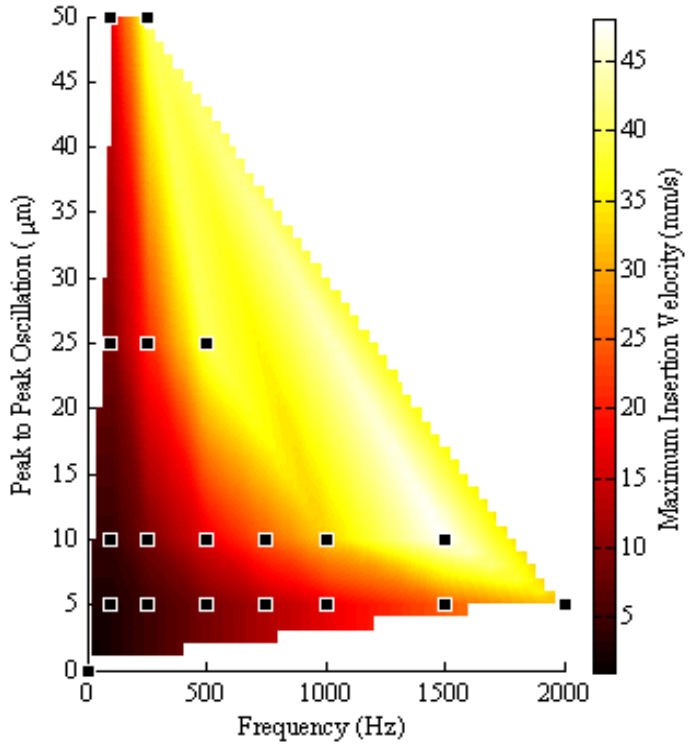

Figure 3-12. Plot of maximum vibratory insertion speed for the vibratory parameter combinations.

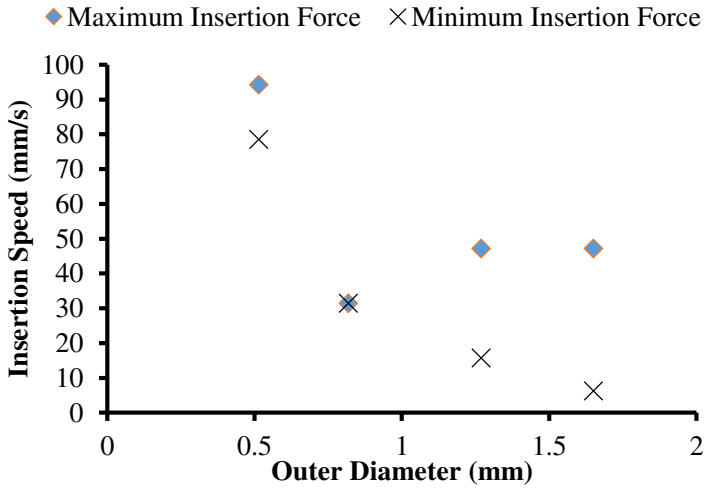

Figure 3-13. The maximum and minimum insertion forces for each needle diameter plotted at the insertion speed at which they occur.

The cause of this trend is hypothesized to be due to the strain rate sensitivity of the tissue as discussed in Chapter 2. The strain rate, $\dot{\varepsilon}$, of the tissue being stretched by the insertion of the needle depends on the needle diameter. For the same insertion rate $\dot{x}_n$, the strain rate is greater for the larger diameter needle. Conversely, for two different sized needles to impart the same strain rate on the tissue, the insertion speed of the smaller of the two needles must be higher than the larger needle. Therefore, the smaller needle would need a higher insertion speed to impart the same optimal strain rate on the tissue. However, as can be seen in Figure 3-13, the minimum and maximum force occurs at the same relative velocity, just at different vibratory parameter combinations. This would imply that the benefits of vibratory cutting are not entirely dependent on relative insertion speed, other phenomena exist. The benefit of reduction of force with applied vibration can be utilized favorably in designing new ways of cutting tissue. An example is provided in the next section.

Vibration Tissue Cutting for Blunt Hollow Needles

This section will discuss utilizing vibration cutting to reduce insertion force of blunted needles in hopes of preventing accidental needlesticks. Blunt needles are too dull to be effective at piercing skin. However, with the aid of applied vibration, the force needed to insert the needle reduces. This would prevent accidental needlesticks by rendering the needle ineffective at cutting tissue unless the healthcare provider was actively using the vibratory device. This concept instills a safety force as can be seen in Figure 3-14. The safety force is the difference between force needed to insert the blunt needle with and without vibration. The goal for this work is to explore how vibration affects the cutting force of blunt hypodermic needles.

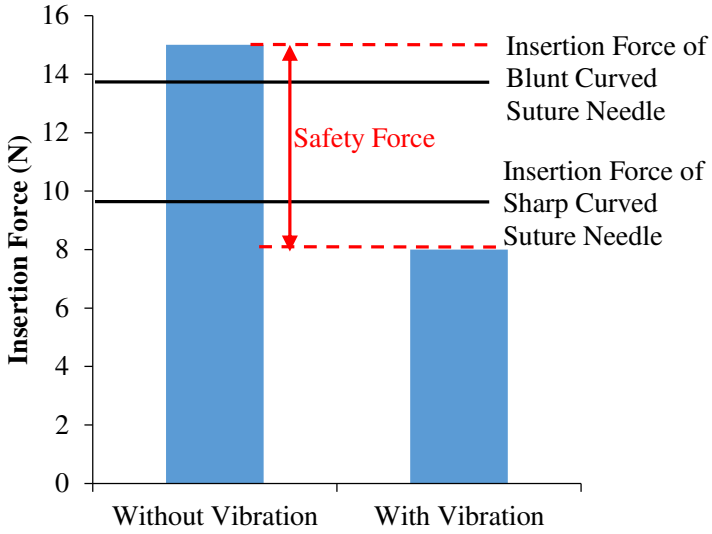

Figure 3-14. Concept of safety force for blunt needles with and without vibration.

Background and Motivation for Using Blunt Needles

Hollow needles, including hypodermic needles, are very commonly used in medical procedures. These needles have a sharp leading cutting edge geometry, one with a high rake and inclination angle that reduces the force needed to pierce the tissue. Reducing the insertion force can reduce pain in the patient and tissue deflection in certain procedures [26]. However, sharp leading edges can lead to accidental needlestick injuries. Needlestick injuries from used medical needles can result in the transmission of over 20 different blood borne pathogens (BBP) including HIV and Hepatitis C (HCV) for which there is no immunization or cure [106]. Between 600,000 and 800,000 needlestick injuries occur to health care workers in the US each year [107] for an estimated annual health care cost of $188 million [108].

By blunting the tip of the needle, needlestick injuries can be reduced. Blunting the tip of the needle gives it a 0° rake and inclination angle, the least efficient cutting geometry. Blunt suture needles have been commonly used over the last 15 years. Figure 3-15(a) illustrates a blunt suture

needle compared to a regular sharp suture needle, Figure 3-15(b). In 1994 a CDC study involving three hospitals in New York City showed that increasing the use of blunt needles in gynecological surgeries from <1% to 55% caused a decrease in percutaneous injuries (PI) from 5.9 PI's per 100 procedures to 1.1 PI's per 100 procedures [109]. However, while the blunt tip is sharp enough to pierce internal tissues, such as muscle and fascia (fibrous, internal tissue that surrounds muscles), it is not sharp enough to pierce through skin under most circumstances [110].

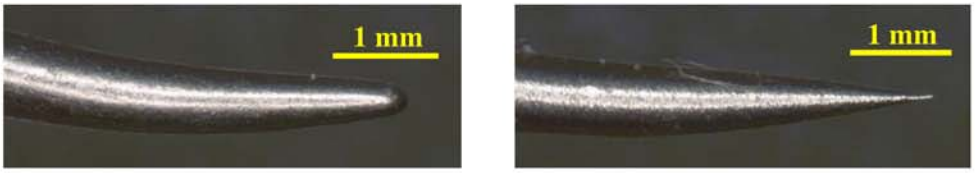

(a) (b)

Figure 3-15. Suture needles that are (a) blunt and (b) sharp.

Blunt Needle Tip Geometry

For this work, hypodermic needles are once again examined. This style of needle contains three ground edges where two combine to form a sharp leading point, of which a standard sharp hypodermic can be seen in Figure 3-16(a). The blunted hollow needle tip geometry developed is shown in Figure 3-16(b), where the sharp tip has been ground down (normal to the z axis) to yield a blunt area. A coordinate system is defined on a needle where z coincides with the center of the needle and x passes through the lowest point as shown in Figure 3-16(b). A given point **A** on the cutting edge is defined by a radial position γ away from the x axis as shown in Figure 3-16(b).

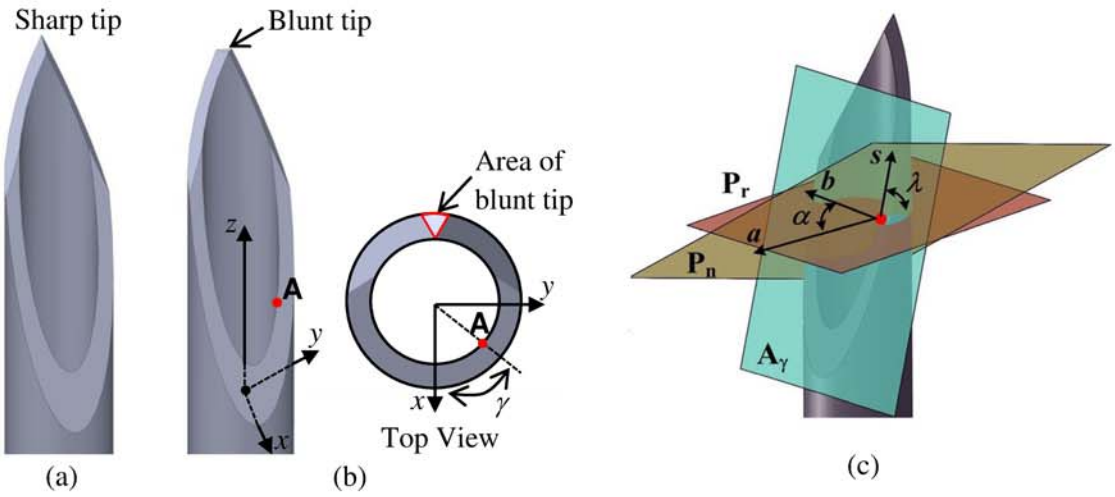

Figure 3-16. (a) Hypodermic needle and (b) novel blunt needle design with (c) rake and inclination angles defined for a hypodermic needle cutting edge [33].

Rake and Inclination Angle

Two critical parameters of the needle geometry are the rake angle, α, and inclination angle, λ, for a needle [111]. These angles vary around the needle circumference and help to define the needle's ability to cut tissue; the higher these angles the sharper the cutting edge. The inclination and rake angle for a hypodermic needle cutting edge is shown in Figure 3-16(c) [33]. Previous studies conducted have determined the rake and inclination angle for multiplane biopsy needles [112], curved needles [113], and hypodermic needles [33]. The inclination and rake angle on a standard hypodermic needle, Figure 3-17(a), and a blunt needle, Figure 3-17(b), were calculated based on equations previously developed by Wang et al. [33]. As illustrated, the geometry is identical except around the needle tip where the blunt needle's rake and inclination angle drop to 0^{o} (poorest configuration for cutting efficiency) at the leading tip of the needle ($\gamma = 180°$). This low inclination and rake angle on the blunt needle will require more force to penetrate tissue [28],

thereby, reducing the risk of accidental needle puncture while increasing the difficulty to pierce the patient's tissue.

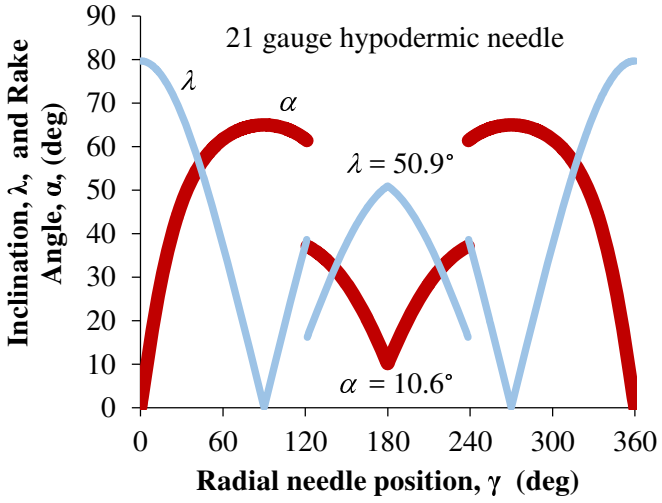

(a)

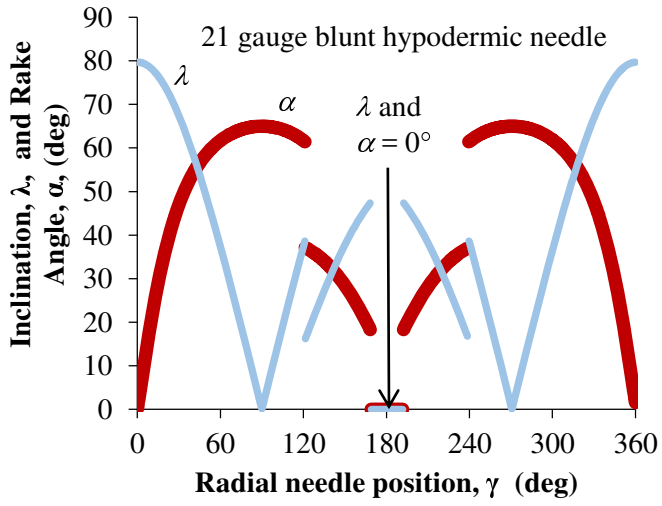

(b)

Figure 3-17. Rake and inclination angles for (a) a standard 21 gauge hypodermic needle and (b) a blunt tip 21 gauge hypodermic needle.

Blunt Needle Tip Fabrication

A blunting device was developed in order to have precise blunting. The blunted needles will modify existing 21 gauge hypodermic needles (BD Precisionglide Needle), the typical size needle for blood drawing and drug administration. The custom apparatus, shown in Figure 3-18, mounts the needle onto a micrometer (Mitituyo). The device is placed onto a precision ground stainless steel plate. The needle is gradually lowered with the micrometer until it makes contact with the plate. The point of contact is determined by measuring the resistance between the needle and the plate. The needle is then lowered out of the device to the desired blunting depth, and ground using an aluminum oxide sharpening stone. The needle is ground until it is flush with the device, thus ensuring precise blunting. The precision blunting allows for determining a relationship between vibration parameters, blunt area, and insertion force.

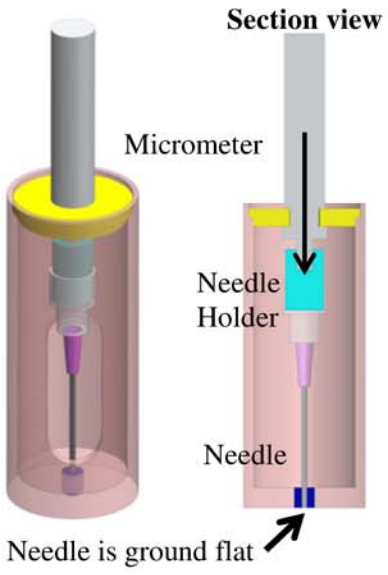

Figure 3-18. Needle fixture device for making blunt tipped needles.

Experimental Setup

A systematic way of testing the insertion force of the blunt needles at varying frequencies and amplitudes was needed. The experimental setup shown in Figure 3-19 was utilized. This setup is similar to the one described in Figure 3-1 previously in the chapter. The difference for this setup is a piezoelectric actuator (Physik Instrumente, Karlsruhe, Germany) with a maximum travel length of 45 microns is utilized. In addition, a smaller six-axis force sensor is used. Instead of the tissue being mounted on the force sensor as in the previous setup, the needle is mounted to the force sensor here. This causes problems to arise that will be discussed in a later section. The porcine skin is also held on by a plate with one large hole instead of 12 smaller holes. The skin is shifted around allowing for more punctures to be taken, but not in a systematic pattern as before. The plate is clamped to the fixture using c-clamps. Much care was taken to ensure no pre-tension or compression was applied to the tissue.

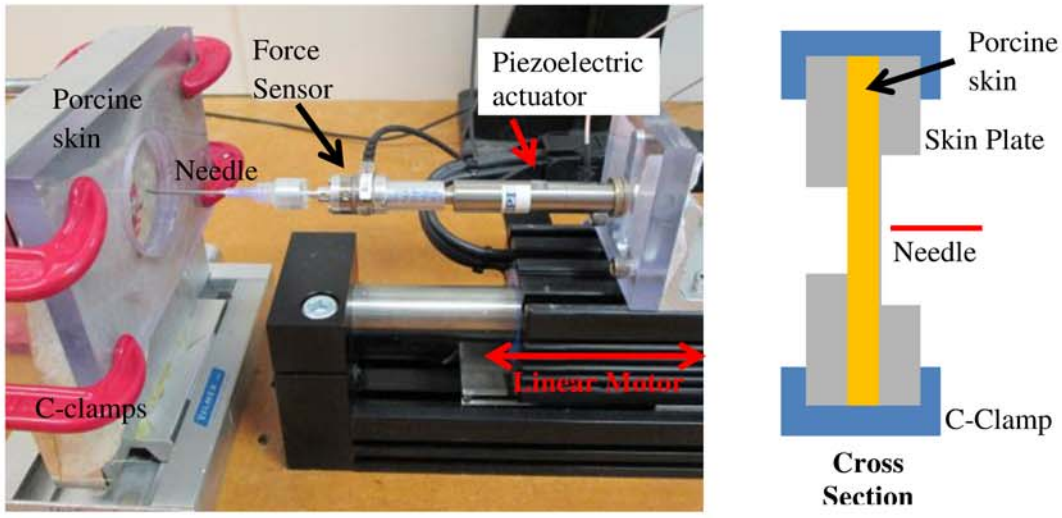

Figure 3-19. Experimental setup with (a) vibratory needle cutting setup and (b) diagram of porcine skin holder.

An experimental procedure was developed to test the effectiveness of different bluntness of needles and different vibratory frequencies. The nominal insertion velocity was kept constant for all of the trials. The linear slide moved forward at a constant 1 mm/s. Three 21 gauge hypodermic needles were used. The needles were sharp (unmodified), blunted down 63.5 µm, and blunted 190.5 µm as shown in Figure 3-20. All three needles were vibrated at varying frequencies: 250, 500, 750, and 1000 Hz, as well as inserted with no vibration. All vibrations had a maximum travel length of 1 µm. For each needle and frequency combination, five trials were run.

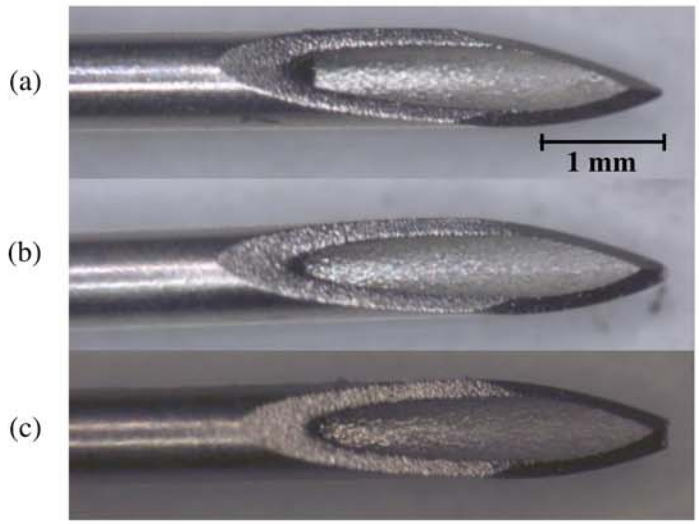

Figure 3-20. Microscope images of the three needles: (a) sharp, (b) blunted 63.5 µm, and (c) blunted 190.5 µm.

Force and position data were acquired for each trial, as shown in the example force plot with vibration, Figure 3-21(a), and without vibration, Figure 3-21(b). The insertion force, force at point of puncture, was determined from these force plots. Due to the nature of the setup, the mass of the needle, and its fixture to the force sensor, an inertial force component appears on the graph as can be seen in Figure 3-21(b). This is due to those items and the force sensor itself moving with constantly changing acceleration due to the vibration. To account for this term, the inertial force

was calculated as the amplitude of the force oscillations before the needle comes into contact with the porcine skin. The amplitude was then subtracted off the peak force to obtain the actual insertion force. Once again, the beginning of the first Phase 2 was used as the insertion force.

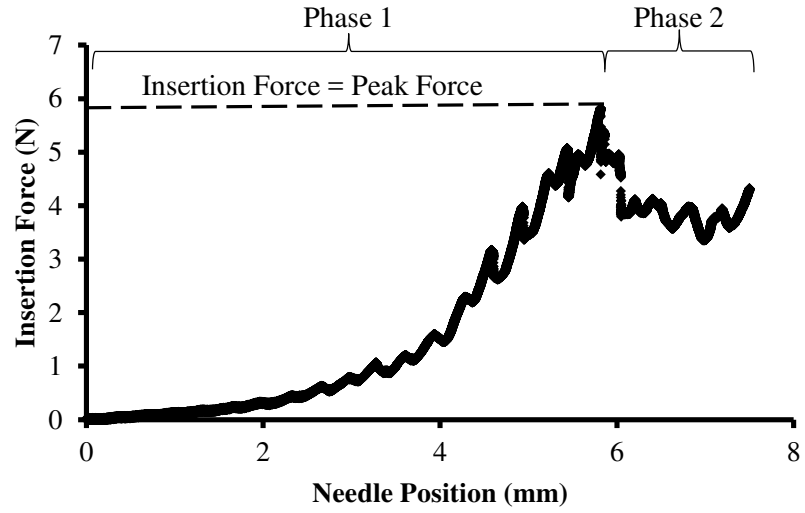

(a)

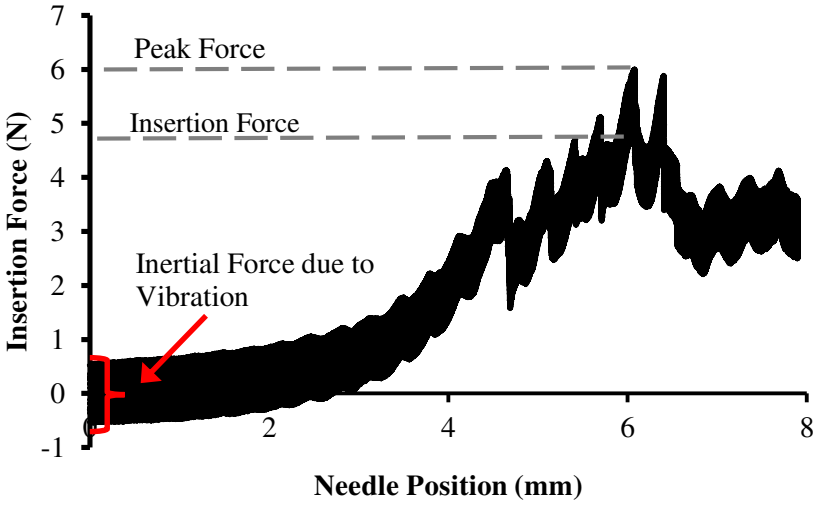

(b)

Figure 3-21. Example insertion (a) with no vibration and (b) with vibration with inertial forces labeled.

Results and Discussion of Blunt Needle Work

The insertion force of the five trials for both needle bluntness and oscillation frequency was averaged and plotted in Figure 3-22. The results from the experiments show that applied vibration lowered the insertion force for the blunt needles. The 63.5 µm needle had a maximum reduction of force of 17% with the applied vibration ($M = 4.77$, $SD = 0.42$) over the control insertion with the 63.5 µm needle ($M = 5.73$, $SD = 0.46$). The 190.5 µm blunt needle with applied vibration ($M = 5.55$, $SD = 0.69$) was able to reduce the insertion force by 18% over the insertion with no vibration ($M = 6.76$, $SD = 0.40$). The standard deviation was highest for the needles at the 1000 Hz frequency. This was caused by the 1000 Hz frequency having the highest inertial force. Both the 63.5 µm needle reduction, $t(8) = 3.40$, $p = 0.004$, and the 190.5 µm reduction, $t(6) = 3.40$, $p = 0.007$, show significant reductions using unpaired T-tests. However, the blunt needles in this study saw a lower improvement than the sharp needles of the previous section (18% versus 35%). The next section describes a study completed on the effects of geometry on vibration needle cutting to determine why the blunt needles benefitted less from the applied vibration.

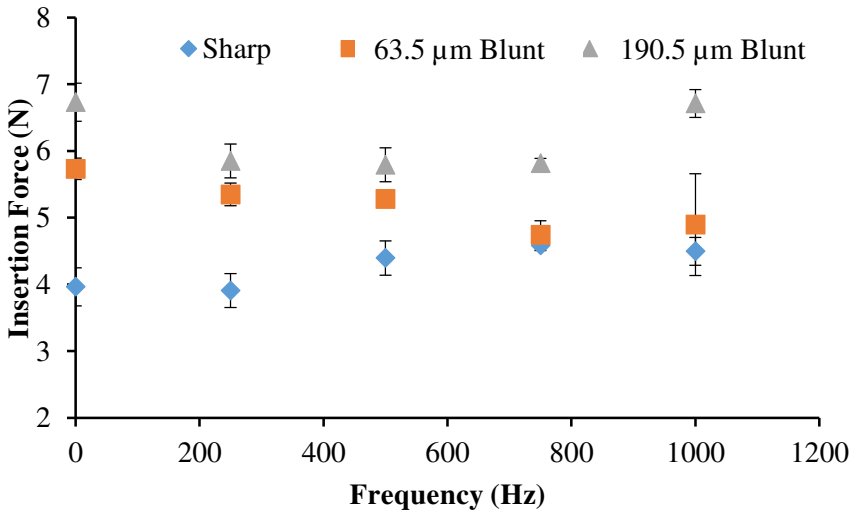

Figure 3-22. Insertion fore of the various needle tip bluntnesses against vibratory frequencies.

Needle Geometry Effect on Vibration Tissue Cutting

This section will discuss the study of needle geometry on vibration tissue cutting. To do so, vibratory parameters will be varied along with the geometry of the needle tip. First, the geometry of the needle tip is defined. Next, the experimental test setup and experimental design are described. Finally, the results are presented and discussed.

Geometry

To determine how geometry and vibratory parameters are related, the geometry of the needle must be quantified. For this study, the volume of the needle from the tip of the needle was considered. Five conical tipped needles were used in this study as shown Figure 3-23 to isolate the effects of one geometric feature: the grind angle ξ_c. Needles such as hypodermic needles have complex cutting faces and angles, making it difficult to fully understand the relationship between geometry and vibration [112]. The symmetric nature of the conical tip does not instill transverse forces on the needle which can cause the needle to deflect [78]. Blunter geometry needles are being utilized in medical procedures to reduce accidental punctures [109, 114-116]. However, the blunt cutting geometry requires greater insertion force to puncture tissue [105].

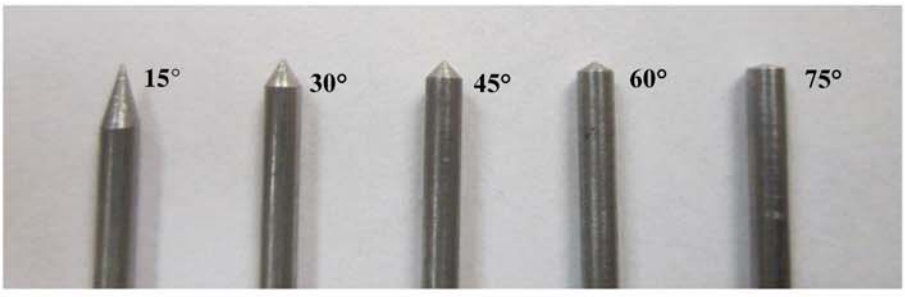

Figure 3-23. Conical tipped needles.

The volume for the conical tipped geometry can be expressed in terms of the grind angle ξ_c and the outer radius r as can be seen on Figure 3-24. The volume is calculated for a given depth z from the tip of the needle in Equation 21:

$$V(z) = \begin{cases} \frac{1}{3}\pi z^3 \tan^2 \xi_c , & z < z_l \\ \frac{1}{3}\pi z_l^3 \tan^2 \xi_c + \pi r^2 (z - z_l), & z \geq z_l \end{cases} \tag{21}$$

Where the length of the needle tip z_l, as seen in Figure 3-24, is given by:

$$z_l = \frac{r}{\tan \xi} \tag{22}$$

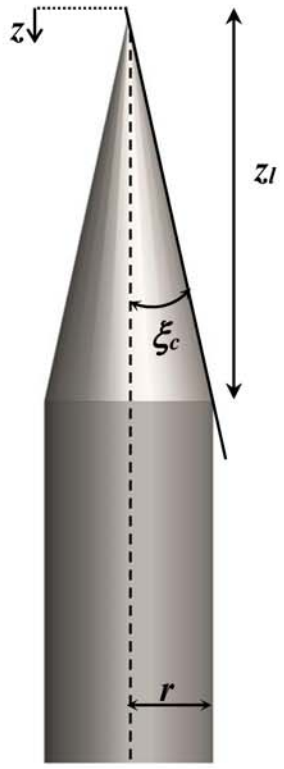

Figure 3-24. Geometry of conical needle tip.

Five conical tipped needles made of 304 stainless steel were considered with varying grind angle ξ. The grind angles utilized were 15°, 30°, 45°, 60°, and 75°. The grind angles were verified by measuring the angles with a stereomicroscope (Zeiss, Oberkochen, Germany). Digital pictures of the needle tips were taken and the grind angles were measured using Axiovision software (Zeiss, Oberkochen, Germany). 304 stainless steel was utilized because is the most commonly used needle material. This material is biocompatible, has good corrosion resistance, and is inexpensive for its high tensile strength and high modulus of elasticity. All needles had an outer diameter of 1.6 mm, equal to that of a 16 gauge needle. Figure 3-25 shows the volume of the needle tip at varying depths for the five different grind angles. As can be seen, the steeper the grind angle (lower ξ_c), the lower the rate of volume change. The lower volume change rate allows the needle to fracture the tissue with less force [71].

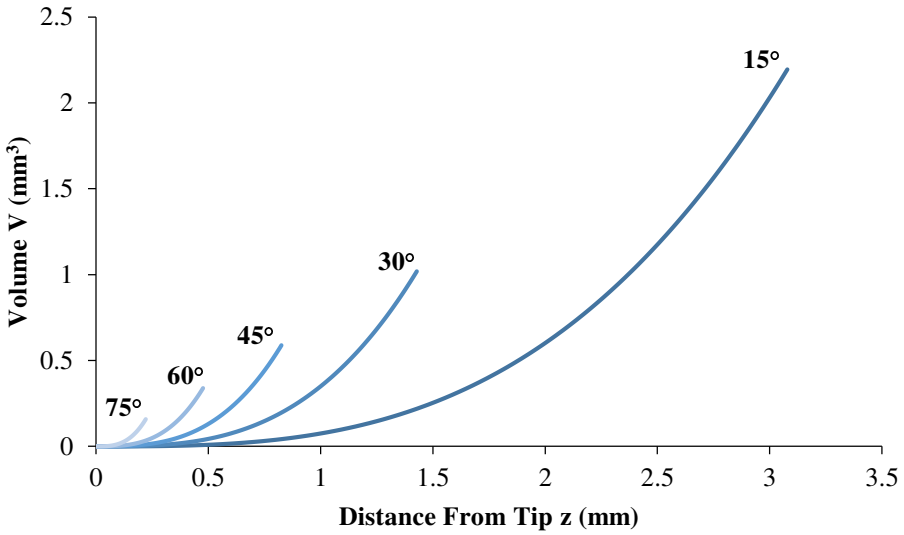

Figure 3-25. Volume of needle tip at a given distance from the tip for each grind angle.

Experimental Procedure

To determine the effects of vibration and geometry on insertion force, two experiments were conducted as outlined in Table 3-4. First, the needles were inserted into ex vivo bovine liver. Bovine liver was used in this study due to its consistency throughout the portion being tested. Bovine liver has been used in previous tissue cutting studies [75, 112, 117]. However, tissue cutting experiments in ex vivo tissue has been shown to have standard deviations up to 25%[29]. A second experiment was conducted to verify the ex vivo tissue results. The needles were inserted into phantom tissue made from a polyurethane sheet of Shore hardness 40A (Polyurethane Products, Addison, IL). Polyurethane sheets have been used in other studies to simulate skin dermis [118, 119]. The phantom material does not produce as accurate of force profiles as ex vivo tissue, but yields more consistent results. These results were used to verify the tissue experiment.

Table 3-4. Outline of two experimental procedures.

	Testing Medium	Needles (°)	Frequencies (Hz)	Amplitudes (μm)
Experiment 1	Bovine Liver	15, 30, 45, 60, 75	100-2000	5-50
Experiment 2	Polyurethane	15, 45	250, 1500	5, 50

Ex vivo Tissue Procedure

Needle Insertion Testing Apparatus

This study utilized the experimental setup shown in Figure 3-26. It utilizes a linear motor (Dunkermotoren, Bonndorf, Germany) to insert the needle into the bovine liver at a constant rate. Mounted to the slide is a piezoelectric actuator (Physik Instrumente, Karlsruhe, Germany) which provided the vibration during the tests. The force was measured with a six-axis force sensor (ATI

Industrial Automation, Apex, NC) mounted on an adjacent table to isolate it from the vibrations. The force sensor was mounted on the tissue side of the experiment.

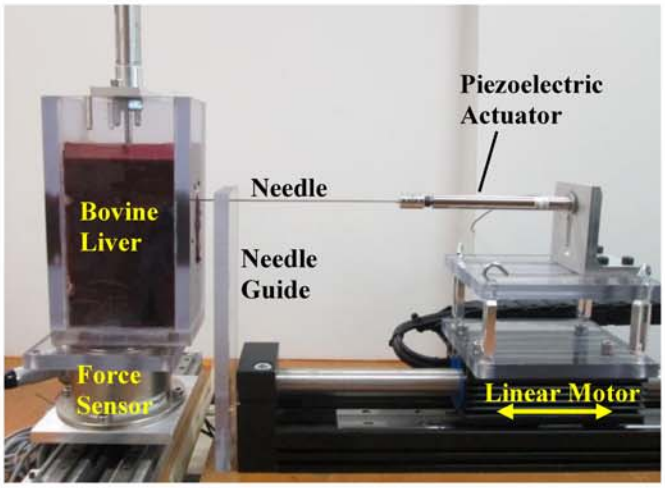

Figure 3-26. Force measurement setup for ex vivo tissue study.

Because workpiece holding is important in consistently cutting soft materials as shown by the study done by Shih et al. [120] on the cutting of elastomers, the bovine liver was held in a box and a slight pressure of 11.65 kPa was applied to the liver. The box had a slot on the front to allow the needle to pass into the tissue. The needle was passed through the middle of the tissue to eliminate effects of boundary conditions.

Tissue damage caused by the insertion of these needles was a factor that was not directly measured in these experiments. However, the needle force does give some indication as to the amount of damage that would be seen on the tissue. Lower force will create less pressure and bruising on the tissue. Needles with sharper geometry will produce less tissue damage by creating less tissue fracture. To more precisely quantify tissue damage future studies will perform histological evaluations.

Experimental Design

An experiment was designed to test the insertion force of different angled conical needles through bovine liver at various vibration frequencies and amplitudes. The steady insertion speed was kept at a constant 1 mm/s, supplied by the linear slide, for all trials. This is to isolate the effects of the vibration as well as the geometry of the needle. Each of the needles was tested at the 18 different combinations of amplitude and auditory frequency as the vibratory parameter study as listed in Table 3-2. Each needle was also inserted with no vibration as a control. The combinations test a broad range of frequencies and amplitudes in to determine the effects of the vibratory parameters and how they are related to the geometry of the needle. The limits of frequency and amplitude tested were determined by the amount of power that could be safely put into the piezoelectric actuator. Having both high frequency and high amplitude requires a large amount of power be applied to the piezoelectric actuator. Excessively high electrical power will cause the actuator to generate large amounts of heat and break the piezoelectric ceramic. The needle was inserted five times at each parameter combination including the control. Each trial was inserted into a new location in the tissue to avoid inserting into the same hole as a previous trial.

Phantom Tissue Procedure

Needle Insertion Testing Apparatus

The test setup shown in Figure 3-27 was utilized to insert the needles into a polyurethane sheet to verify the ex vivo results. This setup utilized the same linear motor, piezoelectric actuator, and six-axis force sensor as the previous setup and is very similar to the setup used in the vibratory parameter study shown in Figure 3-1. The polyurethane sheet was held between two plates to ensure

consistent boundary conditions between trials. The needle was able to pass completely through the sheet.

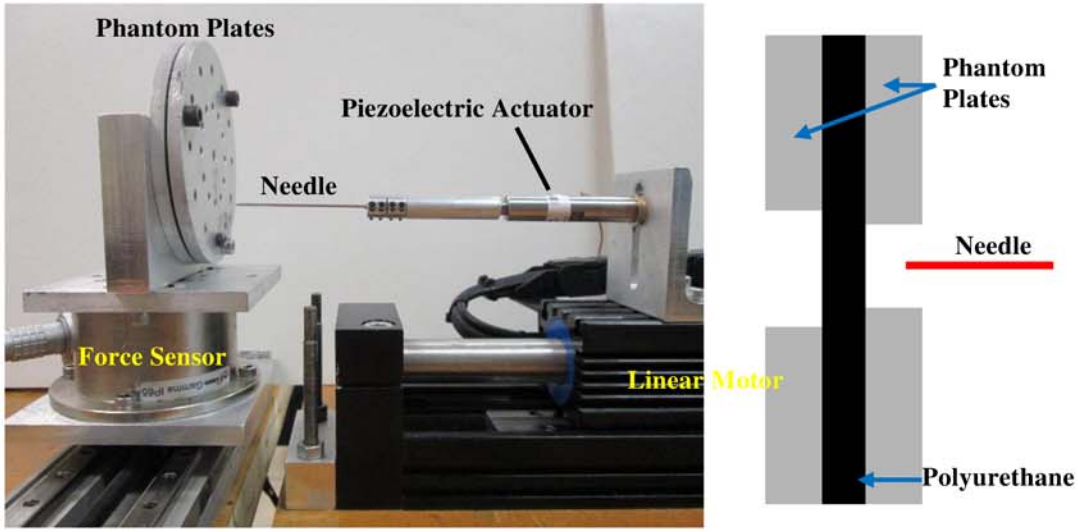

Figure 3-27. Force measurement setup for phantom tissue study.

Experimental Design

The 15° and 45° grind angle needles were inserted through the polyurethane sheets. For this study only two vibratory combinations were utilized in addition to the control insertion, as can be seen in Table 3-5. These parameters were chosen based on the results from the ex vivo tissue study, as well as their locations at the extremes of the combinations tested in the ex vivo tissue study. Each needle was inserted six times for each vibratory parameter. The 45° grind angle needle was utilized to test the blunter geometries due to the 60° and 70° grind angle needles being unable to puncture the polyurethane due to their inefficient cutting geometries.

Table 3-5. Phantom vibratory experimental space.

	Control	Combination #1	Combination #2
Frequency (Hz)	0	250	1500
Peak-to-Peak Amplitude (μm)	0	50	5

Results and Discussion

The results from the two experiments are discussed in this section. First, the insertion mechanics of the ex vivo tissue experiments are described. The insertion forces for each of the needles is then presented. Next, the results from the phantom tissue experiments are presented. These results were used to validate the results from the ex vivo tissue experiments due to the high variance in those trials.

Ex vivo Tissue Results

Insertion Cutting Mechanics

Different cutting mechanics were observed based on the different experimental parameters as summarized in Table 3-6. For the ex vivo tissue experiments it was shown that for 30°, 45°, 60°, and 75° needles with and without vibration had a typical two phase cutting mechanic, as shown in Figure 3-28. This two phase cutting mechanic was also shown in 15° needles without vibration. In Phase I, the tissue deflects and the force gradually rises. In Phase II, the tissue is cut by the needle. There can be many rises and falls of the force as the needle penetrates further into the tissue; repeating many cycles of Phase I and Phase II. The steady increase in force is due to more of the needle being inside the tissue, which increases the friction force. The insertion force is the puncture force that occurs at the first transition between Phase I and Phase II as illustrated in Figure 3-28.

Table 3-6. Insertion cutting mechanics observed for all experiments

	Testing Medium	Needles (°)	Vibration Applied (yes or no)	Cutting Mechanic Observed	Example Figure
Exp. 1	Bovine Liver	15	No	2 Phase, deflection and cutting	Fig. 3-28
		30, 45, 60, 75	Yes and No		
		15	Yes	Continuous cutting	Fig. 3-29
Exp. 2	Polyurethane	15	Yes and No	4 Phase	Fig. 3-38
		45	Yes and No	2 Phase, deflection and short time of cutting	Fig. 3-40
		60 and 75	Yes and No	Unable to break material	

Force and position data were collected for each trial. The data was sampled at four times the vibration frequency to accurately measure the force. A different cutting mechanic of continuous cutting was seen with the 15° grind angle needle with applied vibration than with all other insertions. The other insertions showed a typical cutting mechanic of deflection followed by cutting when cutting soft tissue. An example force plot of the 45° grind angle needle is shown in Figure 3-28. The example force plot in Figure 3-28 illustrates the insertion mechanics for the 30°, 45°, 60°, and 75° grind angle needles with and without applied vibration. As the needle is inserted into the bovine liver, two phases of insertion are observed. In Phase I, the tissue deflects and the force gradually rises. In Phase II, the tissue is cut by the needle. This is evident by a leveling off or decrease in the force. There can be many rises and falls of the force as the needle penetrates further into the tissue, repeating many cycles of Phase I and Phase II. The steady increase in force is due to more of the needle being inside the tissue, increasing the contact area between the needle and the tissue which increases the friction force. The insertion force is the puncture force that occurs at the first transition between Phase I and Phase II as illustrated in Figure 3-28.

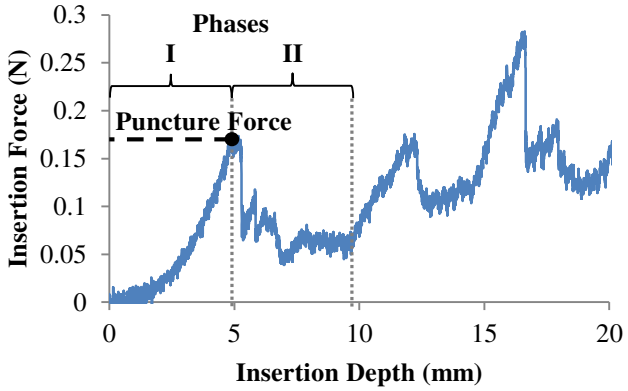

Figure 3-28. Cutting mechanic of deflection then cutting shown in insertion force for 45° grind angle needle without applied vibration.

The insertion force for the 15° grind angle displayed a different cutting mechanic with the vibration applied, as shown in Figure 3-29. Without applied vibration, the needle cutting mechanic was the same as Figure 3-28, with Phase I and Phase II distinctly present. With the vibration applied, the needle geometry in conjunction with vibration was sharp enough to cut without Phase I and Phase II being easily distinguishable from each other. This is evident by the constant increase in force as the needle is inserted deeper. This was true for all vibratory combinations tested. This cutting mechanic is important because the needle inserts into the tissue without large deflections, which can lead to better needle placement accuracy, important for many medical procedures. For the 15° grind angle trials with vibration applied, the insertion force was determined as the force at 7.5 mm insertion depth for all trials. This depth was chosen because it is the average insertion depth of the puncture force of the 15° grind angle control insertions. 7.5 mm is also twice the tip length for the 15° grind angle needle, allowing for the complete outer radius of the needle to enter the tissue.

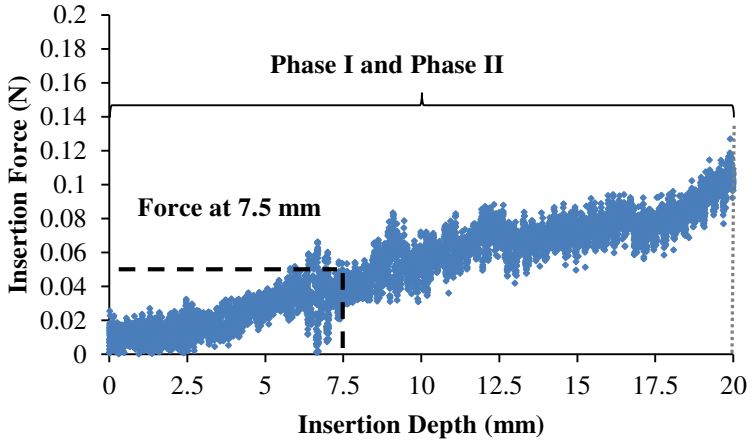

Figure 3-29. Cutting mechanic of continuous cutting shown in insertion force for 15° grind angle needle with applied vibration.

Frequency and Amplitude Results

The results for the insertion force trials were averaged across the five trials at each set of parameters. The results were then plotted against the amplitude and frequency of the vibration. A linear interpolation was conducted to map out the insertion force between tested parameters. This was done for the five different needles separately. The average standard deviation at each data point was 32.5%. This is attributed to the inherent variability in the liver tissue being tested. The results for the 15°, 30°, 45°, 60°, and 75° grind angle needles are shown in Figure 3-30 through Figure 3-34 respectively.

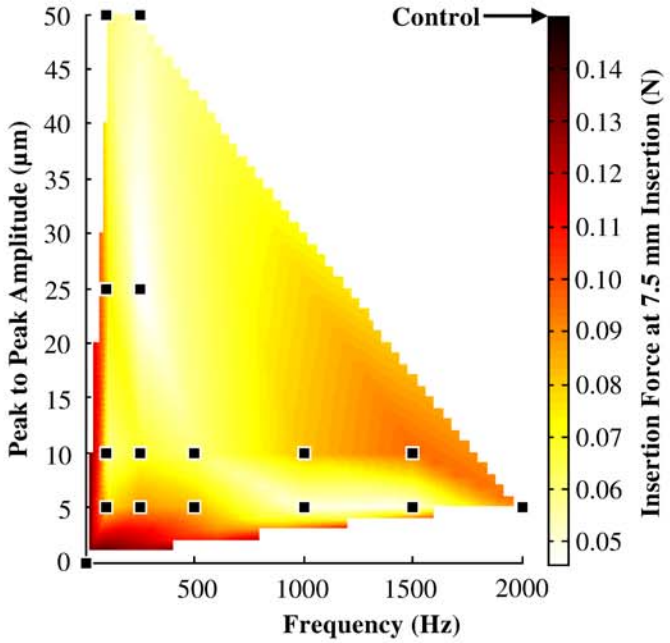

Figure 3-30. Insertion force map for 15° grind angle.

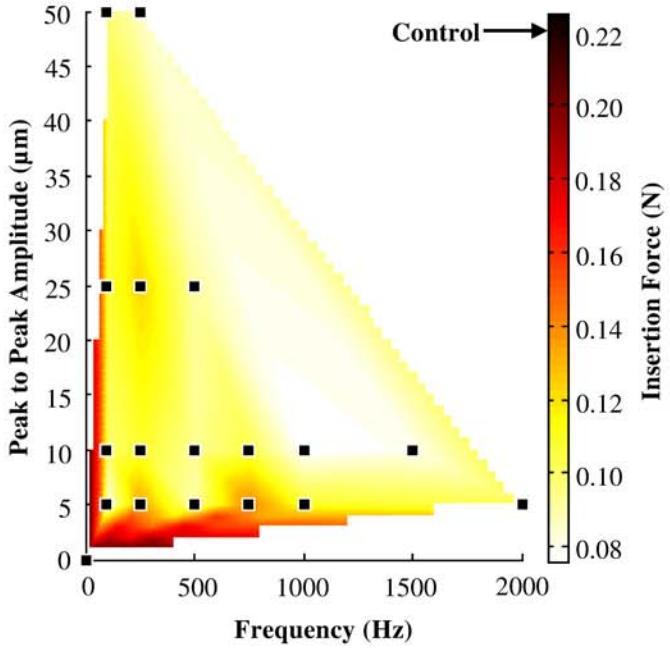

Figure 3-31. Insertion force map for 30° grind angle.

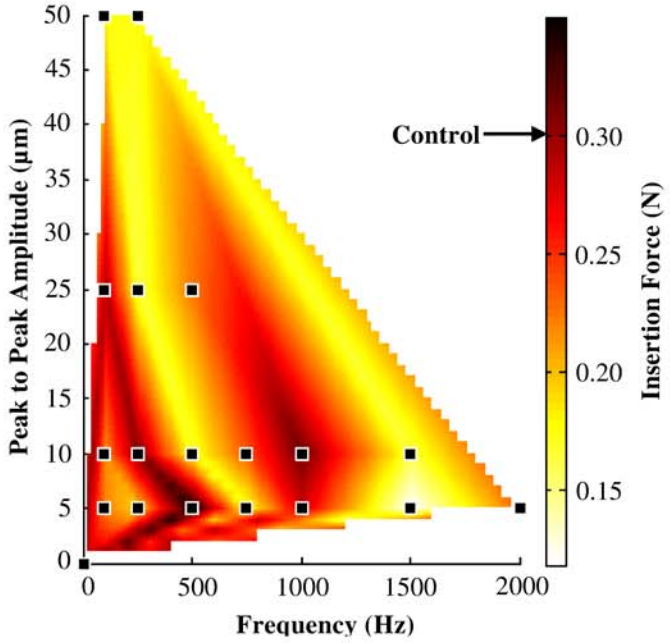

Figure 3-32. Insertion force map for 45° grind angle.

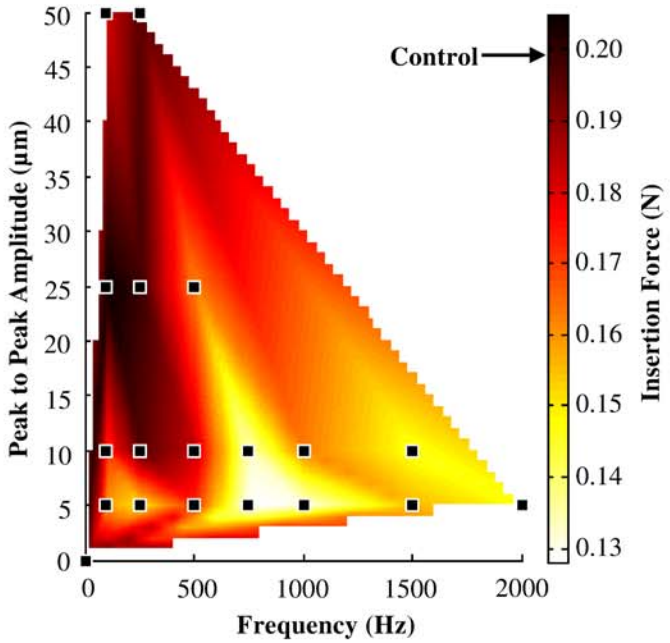

Figure 3-33. Insertion force map for 60° grind angle.

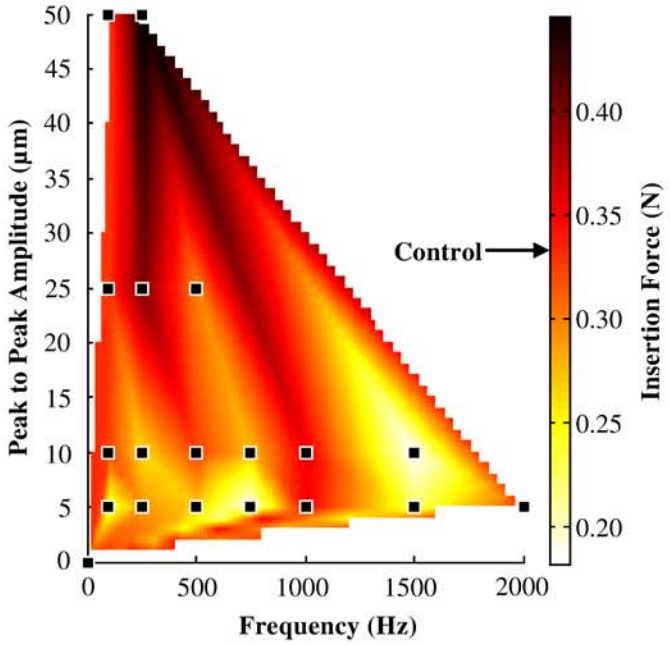

Figure 3-34. Insertion force map for 75° grind angle.

As the force maps in Figure 3-30 through Figure 3-34 show, there are regions of high and low forces in the plots. All needles show a reduction in force due to applied vibration. To quantify the reduction, the highest force and lowest force was determined for each needle. These maximums and minimums were compared to the control insertion for each needle and the percent difference from the control insertion is plotted in Figure 3-35. As can be seen in Figure 3-35, for the two sharpest needles, the 15° and 30° grind angles, the highest insertion force was the control insertion. The three blunter needles had the highest recorded insertion force occur at one of the vibratory parameter combinations. Figure 3-35 also shows the greatest reduction in cutting force for each needle. The maximum percent reduction and the vibratory parameters where the minimum occurred can be seen in Table 3-7. As can be seen, there was not one combination that lowered the insertion force the most for every needle, however the results show that vibration can be utilized to reduce the insertion force of needle penetration, by up to 67%. The sharpest needle, 15° grind angle, had

the greatest maximum reduction in force from the insertion with applied vibration (M = 0.048 N, SD = 0.018) over the control insertion (M = 0.150 N, SD = 0.074). The lowest reduction of force came from the 60˚ grind angle. The application of vibration (M = 0.13 N, SD = 0.03) was only able to reduce the force a maximum of 36% over the control insertion (M = 0.20 N, SD = 0.05).

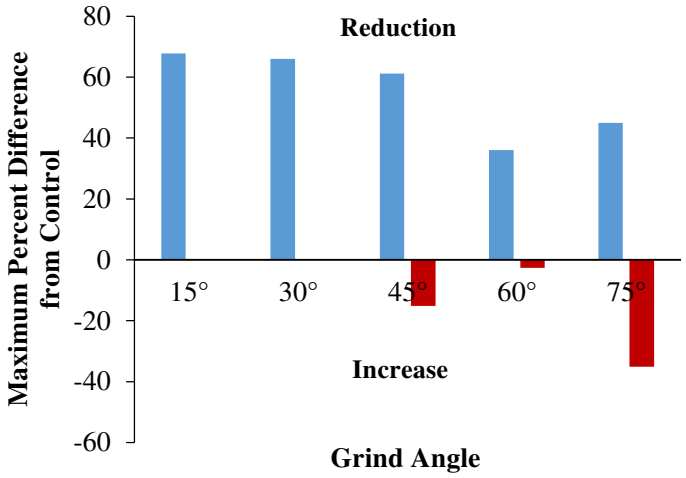

Figure 3-35. The maximum reduction and increase in insertion force from the control insertion due to applied vibration.

Table 3-7. The maximum insertion force reduction for each grind angle and the frequency and peak-to-peak amplitude of where it occurred.

Grind Angle (Degrees)	15	30	45	60	75
Maximum Percent Force Reduction	67.7%	66.0%	61.2%	36.0%	45.0%
Frequency (Hz)	1500	1000	1500	750	750
Peak-to-Peak Amplitude	5	10	5	5	5

As can be seen in Figure 3-35, as the needles become blunter, the control is no longer the highest insertion force. In addition, the maximum percent force reduction decreases with the blunter needles as well. This would imply geometry has a role in the effectiveness of the vibration in reducing the insertion force. To determine the effect of geometry on vibration tissue cutting, all the vibration trials were averaged together and compared to the control insertion. The results are shown in Figure 3-36. The results show that for the sharper needles, any applied vibration is beneficial and will reduce the insertion force. Significance was verified with unpaired T-tests. The 15˚ grind angle saw a 55% (SD = 9.07) average reduction in force with applied vibration over the control insertion, $t(52) = 3.20$, $p = 0.002$, and the 30˚ grind angle needle reduced the insertion force by 54% (SD = 9.71), $t(58) = 7.23$, $p < 0.001$. However, as the needles become blunter, the overall benefit of vibration begins to decrease and its ability to reduce the insertion force is lost. The 45˚ grind angle needle reduced the insertion force with applied vibration by an average of 30% (SD = 19.62) over the control insertion, $t(68) = 1.56$, $p = .12$, the 60˚ grind angle needle reduced 17% on average (SD = 12.20), $t(80) = 1.26$, $p = 0.21$, and the bluntest needle, 75˚ grind angle needle, with applied vibration reduced the insertion force by the least amount, 10% (SD = 20.91), $t(66) = 0.52$, $p = 0.60$. The three bluntest needles show no significant average reduction in force over the control insertion. This implies the application of vibration to the needle cannot overcome blunt, inefficient geometries to reduce the insertion force. The standard deviation also increases for the blunter geometries. This is due to the applied vibration not being as effective, causing the forces to be higher and more inconsistent.

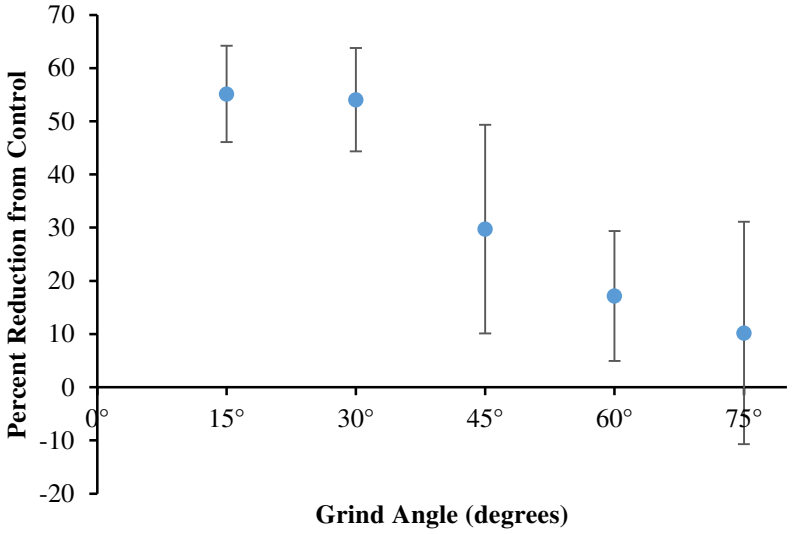

Figure 3-36. The average reduction in insertion force from the control insertion due to applied vibration.

The force map in Figure 3-34 for the bluntest needle (75° grind angle) shows the regions of high insertion force are located at higher amplitudes. This would imply that for blunter geometries, amplitude emerges as a factor for determining the insertion force. To determine the dependence of the amplitude of vibration on insertion force, the insertion forces were averaged at all frequencies at each amplitude. The 75° grind angle needle has a significantly, $t(34) = 2.76$, $p = 0.01$, greater insertion force at 50 µm amplitude ($M = 0.39$, $SD = 0.09$) than at 5 µm amplitude ($M = 0.26$, $SD = 0.06$) as illustrated in Figure 3-37. The 60° grind angle needle showed an increase in insertion force as the amplitude increased, but not as direct as the 75° needle. The 15°, 30° and 45° grind angle needles did not show general trends with respect to the amplitude of vibration. Linear fits were applied to the data to quantify the relationship between insertion force and amplitude. The rate of increase in the insertion force with respect to amplitude as well as the R^2-value for the fit can be seen in Figure 3-37. The 15° grind angle needle was omitted on the graph for ease of viewing and had a rate of -0.198 mN/µm and R^2-value of 0.61. The increase in insertion

force with higher amplitude of vibration for the 75° grind angle needle could be due to the blunter geometry not being able to cut the tissue and thus the higher amplitude deflecting the tissue more, increasing the insertion force. Also illustrated in the average insertion force experimental results, Figure 3-37, blunter geometries have higher standard deviations.

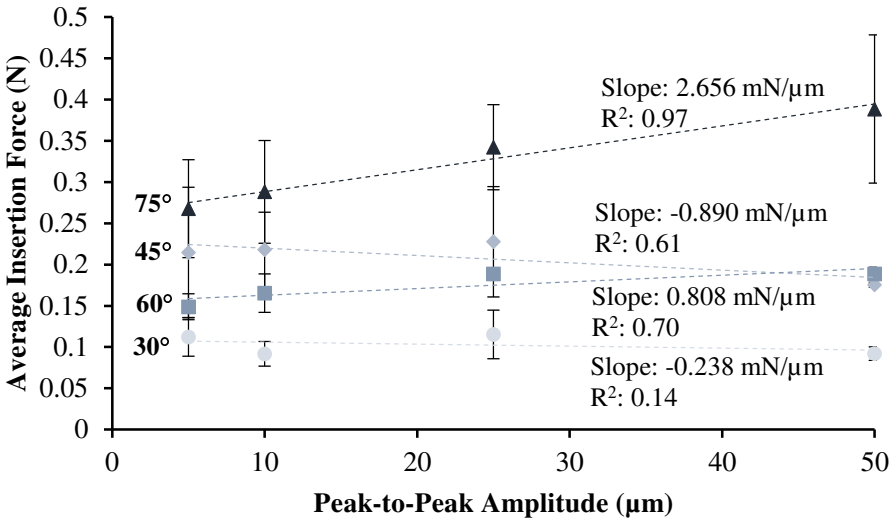

Figure 3-37. Average insertion forces for 30°, 45°, 60°, and 75° grind angle needles versus amplitude with linear trendlines.

Phantom Tissue Results

Insertion Force Mechanics

Similar to the ex vivo tissue experiments, force and position data was collected for each trial. A unique four phase cutting mechanic was found for the 15˚ needle with and without applied vibration as shown in Figure 3-38. For this plot, one insertion was a control insertion with no vibration applied and the other was with vibration combination #2 (250 Hz, 50 µm) as described in Table 3-5. In Phase I, the phantom tissue just deflects without being cut. Phase II is when the needle first punctures the phantom tissue. Phase III is the spreading of the crack to accommodate the

increased diameter of the needle as insertion progress. Phase IV is where the needle tip exits the phantom tissue and only friction remains. As can be seen in Figure 3-38, the vibration decreases the force needed to extend the crack in the phantom tissue and the friction force between the needle and the phantom. To determine the effect of vibration, the force at the first peak (end of Phase I) and the peak force in Phase III were recorded and plotted in Figure 3-39. The applied vibration (M = 2.18, SD = 0.12) does decrease the force needed to extend the crack in Phase III compared to the control insertion (M = 2.58, SD = 0.24) by 15.5%, $t(10) = 2.22$, $p = 0.03$, however, the puncture force is the same, a 1.8% difference, $t(8) = -1.48$, $p = 0.09$, for both no applied vibration (M = 2.48, SD = 0.03) and applied vibration (M = 2.53, SD = 0.06). The variances are higher for the force in Phase III than the puncture force in Phase I. The force needed to create the crack in the polyurethane was more consistent than the force needed to propagate the crack. Figures 3-38 and 3-39 show a benefit to using vibration, as the ex vivo tissue result suggested for the sharpest geometry.

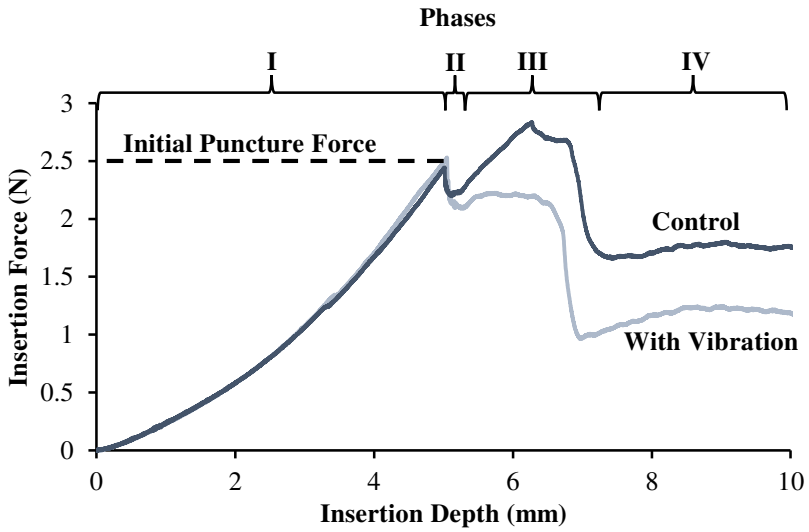

Figure 3-38. Insertion mechanics of 15° grind angle into phantom tissue.

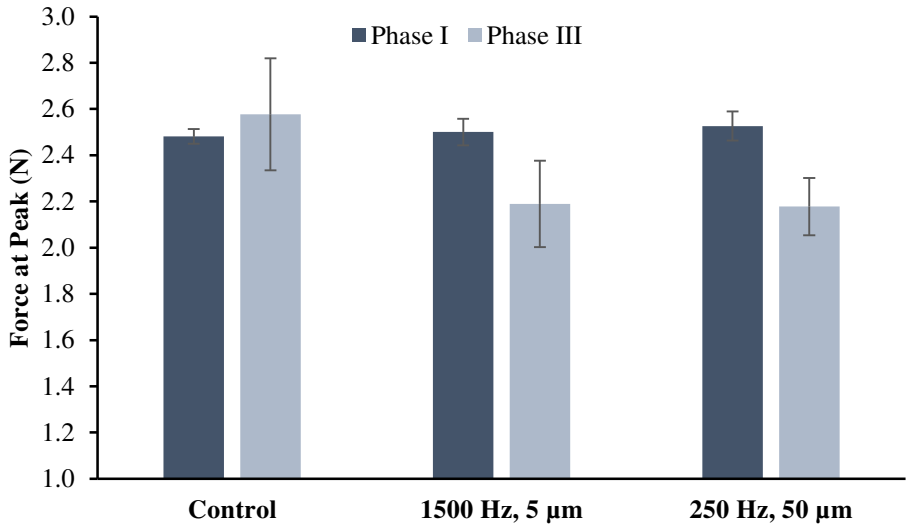

Figure 3-39. Peak forces for Phase I and Phase III for 15° grind angle needle with and without applied vibration.

A two phase cutting mechanic was found for the insertion of the 30° and 45° grind angle needle is shown in Figure 20. Figure 20 shows a 45° grind angle needle with a control insertion and an insertion with vibration combination #2 (250 Hz, 50 µm) as described in Table 3-5. The insertion of the 45° grind angle needle is shown in Figure 3-40. The plot shown is for a control insertion and an insertion with vibration combination #2 (250 Hz, 50 µm) as described in Table 3-5. For the blunter needle, there is no longer an initial puncture and then extension of a crack. The entire cutting occurs at one instance, as can be seen as the complete drop off of force after the puncture. The sudden release of force when the polyurethane is fractured creates vibrations in the experimental setup which causes oscillations in the force after the initial puncture force. The results of the 45° grind angle needle for the control insertion force ($M = 9.35$, $SD = 0.08$) and two vibratory combinations, Combination #1 ($M = 9.33$, $SD = 0.15$) and Combination #2 ($M = 9.32$, $SD = 0.05$, show no change in the initial puncture force across the three vibratory parameters. A three way ANOVA test was used to show no significant differences in the force between the three insertion

cases, $F(2,6) = 0.05$, $p = 0.95$. Once again, the standard deviation for the puncture force is low (1% on average). The force needed to create the crack is consistent for the 45˚

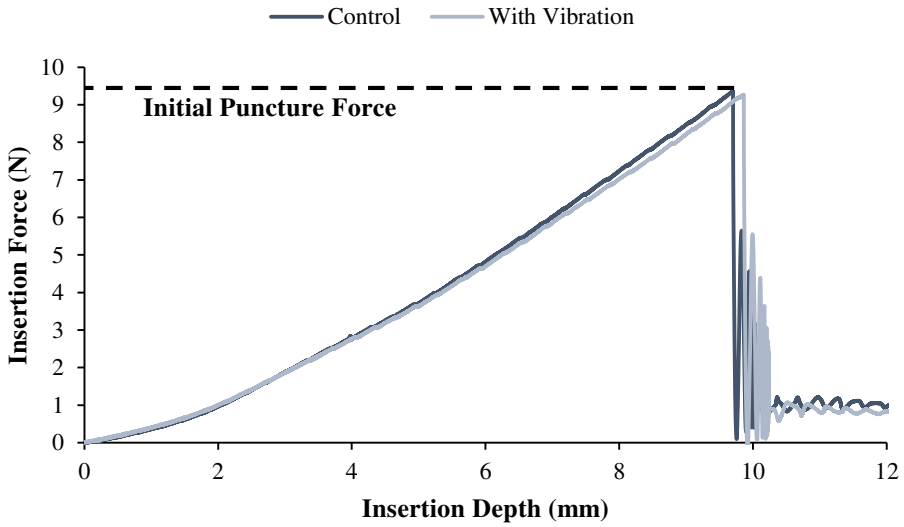

Figure 3-40. Insertion mechanics of 45° grind angle needle into phantom tissue.

The bluntest needles with 60° and 75° grind angles were unable to puncture the synthetic material. In these experiments, the needle begins to bend around 25 N, forcing the test to be stopped. This occurred for both with and without vibration. This exceptionally high force is a result of the needle tip geometry being unable to initiate a crack in the material.

The phantom results using conical needles show the force needed to initiate puncture was the same for a given needle regardless if there is applied vibration or not. In the sharpest needle (15° grind angle) after the initial puncture of the phantom tissue the vibration reduced the friction between the needle and the phantom and lowered the force needed to extend the crack (Phase III). The duller needles tested created so much force before puncture that the needle broke through the phantom in an extremely short time period. This high force and short cutting phase caused the vibration to not have a noticeable affect after fracture.

Concluding Remarks on Vibration Cutting

Needle vibration has been shown to be a viable solution in reducing insertion force to better perform medical procedures. Previous researchers have shown that with the application of axial vibration, the insertion force can be reduced; however, there is little fundamental knowledge about how specific vibratory parameters and geometry impact vibratory cutting force. The results presented in this chapter helped to fill this void in knowledge in two key ways:

- **Results show that applied vibration in the auditory frequency range tested in this study (100 Hz to 2000 Hz) can reduce the insertion force of the needle, up to 35% in ex vivo porcine skin.** However, no frequency and amplitude combination produced the lowest force across all the needles. By reducing force, medical procedures can be carried out with more success. Needle accuracy can be increased and patient pain can be reduced.
- **The effect of geometry on the performance of vibration tissue cutting was newly developed and presented.** Sharp, efficient cutting geometries showed an average reduction of 55% whereas no significant improvements for blunter needles were seen for insertion into ex vivo bovine liver. The vibration has been shown to not be able to overcome the inefficient cutting geometry of blunt needles, thus not reducing the insertion force. This implies vibration cannot be applied to blunt geometries to improve the performance of the needle. Vibration was also shown to change the cutting mechanics of needles, allowing for a more continuous cut as opposed to deflection then cutting. This could benefit the insertion process greatly by increasing needle accuracy by reducing the tissue deflection.

This chapter explored vibration tissue cutting and how it relates to the geometry of the needle. The high variance in the biological tissue results, due to large variances seen in biological tissue, made optimizing parameters difficult. However, the results still clearly show that vibration can significantly improve cutting forces. Chapter 4 uses the information developed in this chapter

to design a novel cutting geometry that utilizes vibration to change the cutting direction of the needle.

Chapter 4

Vibratory Needle Insertion of Compliant Geometry Needles

Compliant mechanisms use elastic deformation of the mechanism to transfer force or motion as opposed to linkages and joints used in traditional mechanisms [121]. The compliant mechanisms are used in micro-devices, actuators, tools, and other areas as a way to reduce weight and number of parts needed for a design. Researchers have previously used compliant needles to aid in needle steering procedures by changing the deflection of the needle [122-124]. The needles incorporate an actuation mechanism that bends the compliant needle to steer it through tissue. The compliant needles bend with less force than traditional needles making it easier to actuate the needle tip. This study explores the use of vibration and compliant geometry to reduce the cutting force of the needle. Experiments were performed in phantom tissue to determine the performance of the compliant needle. This chapter defines the compliant geometry and the cutting edge geometry of the needle, describes the test setup and procedure used to test the geometry, analyzes the results from the experiments, and presents the conclusion from the work.

Compliant Needle Geometry

A novel compliant needle is designed that responds to applied axial vibration to change the cutting direction of the needle tip. The applied vibration causes the compliant geometry of the needle tip to move perpendicular to the insertion direction as shown in Figure 4-1. This changes the cutting direction of the needle from parallel to the insertion direction to be perpendicular to the insertion direction. The purpose of the change in cutting direction is to reduce the deformation of tissue in the insertion direction. For example, for prostate brachytherapy, the parallel insertion force has been found to rotate the prostate up to 13.8°, moving the target location from its original

position [125]. The goal of perpendicular cutting is to reduce the insertion force in the parallel direction thereby reducing the tissue deformation.

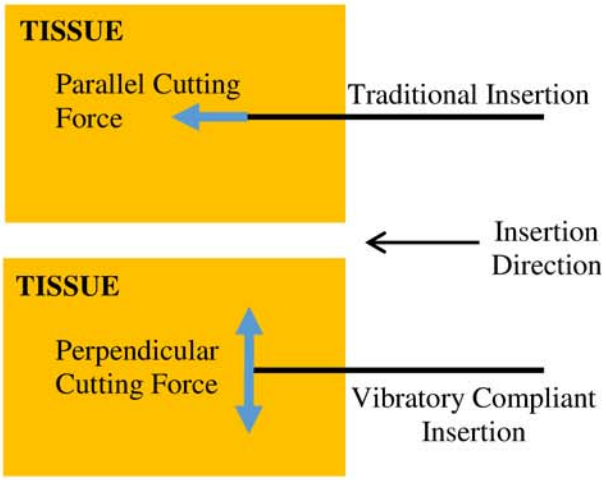

Figure 4-1. Traditional needle insertion with parallel cutting direction and the novel vibratory compliant insertion with perpendicular cutting force.

To achieve transverse cutting, the needle shown in Figure 4-2 was designed and manufactured. Two slits are cut into the needle a distance D_1 down from the tip offset a distance D_2 apart. The slits can be on the same side or opposite sides of the needle. For the needle in Figure 4-2, the slits are on opposite sides. The slits are cut to a depth H and with a thickness t. The needle has a radius r. The slits in the needle create a single axis flexural hinge which allows the tip of the needle to move in the transverse direction with the application of axial vibration. Single axis flexural hinges utilize geometry, a slender region of the structure, to allow the structure to rotate about one axis without the need of moving parts [126]. The needle is vibrated at resonance to achieve the greatest amplitude of vibration at the needle tip. The compliance of the needle is used to modify the axial mode shape to incorporate transverse motion. Tcherniak [127] similarly utilized compliant geometry to achieve the maximum displacement of a resonating structure.

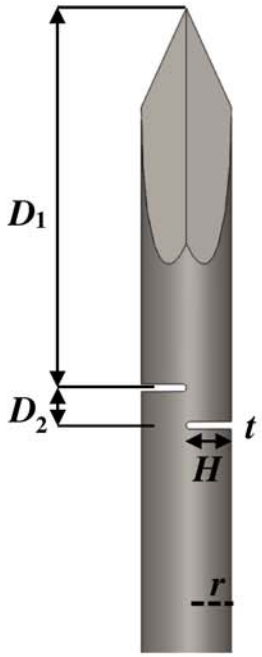

Figure 4-2. Definition of compliant geometry of needle.

Five compliant geometries are considered in this study. The needles parameters can be seen in Table 4-1. For this study, the distance from the tip D_1, the offset distance between the slits D_2, and the slit side location was varied. The radius of the needle was the same for all cases and was equivalent to the radius of an 18 gauge needle which is commonly used in brachytherapy and biopsy. The slit depth H and thickness t were held constant. The slit depth for this study was equal to the radius of the needle. Needles with deeper cut slits cannot achieve resonance with the current test setup as described in the *Experimental Setup* section of this chapter. The slits are 75 μm thick due to the limitations of the wire electron discharge machine (EDM) process used to manufacture the slits. The slits are as wide as the wire utilized during EDM machining, thereby limiting the slit size. A control needle with no slits was utilized to compare to the effects of the compliant geometry.

Table 4-1. Compliant geometry for needles used in this study.

Needle	*r (mm)*	D_1 (mm)	D_2 (mm)	*H*	*t* (µm)	Side
Control	0.635	n/a	n/a	n/a	n/a	n/a
Compliant 1	0.635	5	0.5	*r*	75	Opposite
Compliant 2	0.635	5	1	*r*	75	Opposite
Compliant 3	0.635	10	0.5	*r*	75	Opposite
Compliant 4	0.635	5	1	*r*	75	Same
Compliant 5	0.635	10	1	*r*	75	Same

Finite Element Analysis of Compliant Needle

Finite element analysis was conducted to determine the motion of the needle tip. For this study, the needles will be vibrated with an ultrasonic transducer at 20 kHz. For the ultrasonic vibration to maximize movement, the axial resonance frequency of the needle must match the driving frequency: 20 kHz. To determine the length of the needle, the equation for longitudinal wave propagation through a homogeneous rod with variable cross-section is used [128].

$$-\frac{d}{dx}\left[EA(x)\frac{dU(x)}{dx}\right]=\omega^2\rho A(x)U(x) \tag{23}$$

Where E is the Young's modulus of the material, $A(x)$ is the cross-sectional area of the rod at a given position x, ρ is the density of the material, ω is the resonant frequency of the needle, and $U(x)$ is the axial displacement of the horn at a given position x. The needle used in the finite element analysis had a length of 130 mm. The needle is made of 304 stainless steel with a Young's modulus of 200 GPa, a Poisson's ratio of 0.29, and a density of 8000 kg/m^3.

To determine the motion of the needle tip, a modal analysis study was conducted using ANSYS software (Canonsburg, PA). Ten node tetrahedral elements were used to mesh the tip of the needle down to 0.5 mm below the bottom slit, as they are the simplest geometry to mesh

complex shapes. Twenty node brick elements were used to mesh the rest of the needle to reduce the number of elements needed and to save on computation time. A three iteration mesh refinement was performed to determine that the mesh size was adequate (natural frequency within ±1% for each mesh size). The deformation results of the first axial mode of the control needle and five compliant geometries can be seen in Figure 4-3(a-f). The contours represent the mass normalized *X*-direction displacement (transverse motion). To compare the displacements of each needle to the others, the displacement of the mode shape of each needle was normalized to the maximum axial displacement (*Uz*). This allowed the performance of the compliant needle to be determined by how much transverse motion (*Ux*) was achieved from axial vibration. The results, shown in Table 4-2, show the control needle has no motion in the transverse direction, as to be expected. The wider offset D_2 provided more transverse motion, as did having the slits farther down the needle (larger D_1). The transverse motion was also improved by having the slits on the same side of the needle as opposed to opposite sides.

Table 4-2. Mode shape displacements of the needle tip in the *Z*-direction (axial) and *X*-direction (transverse) normalized to the axial displacement.

	Control	**Compliant 1**	**Compliant 2**	**Compliant 3**	**Compliant 4**	**Compliant 5**
Uz	1	1	1	1	1	1
Ux	$-3.152*10^{-5}$	-0.0042	-0.0167	-0.0452	-0.0496	0.1796

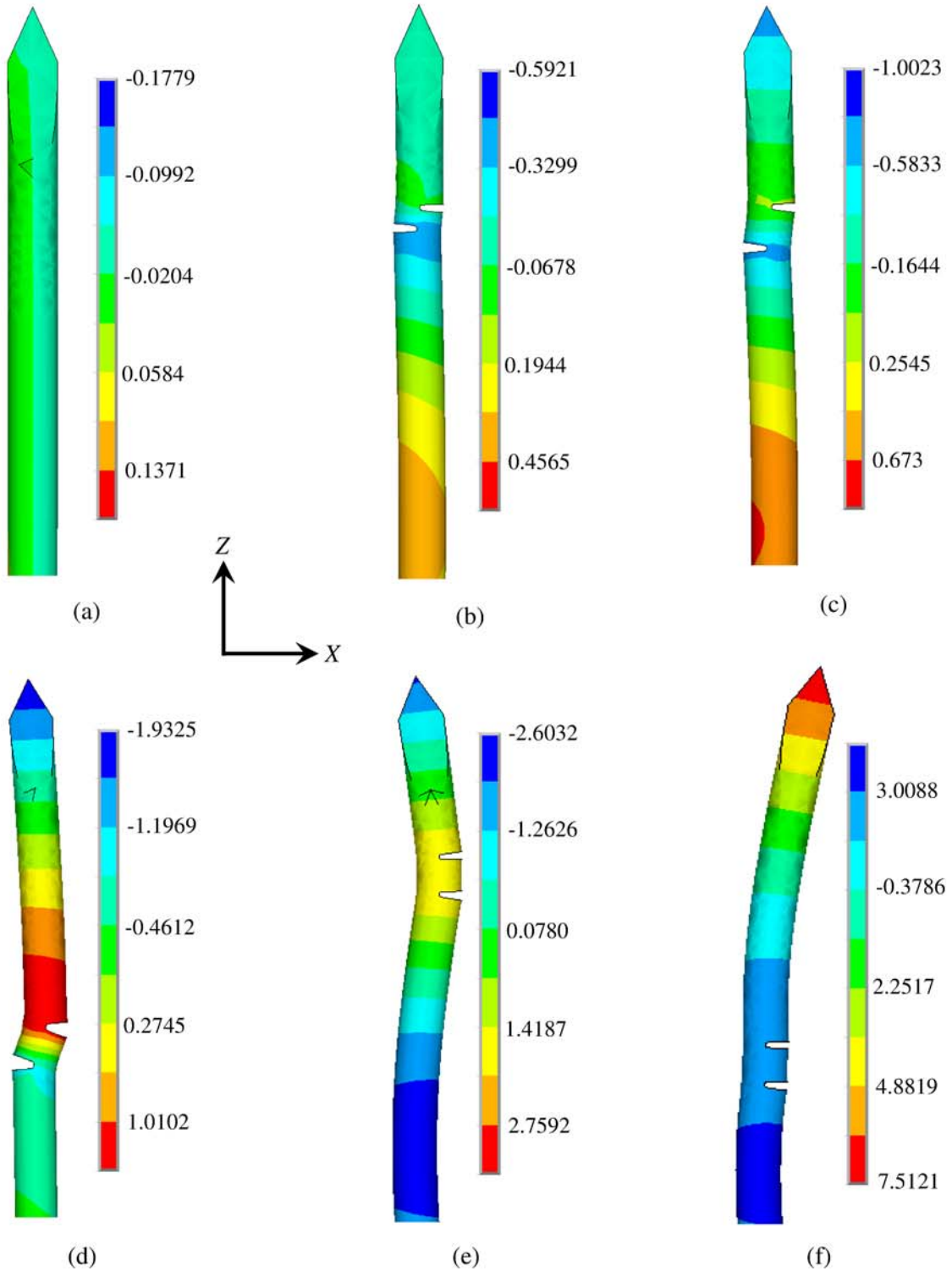

Figure 4-3. Modal analysis *X*-direction mass normalized displacement results for (a) control needle, (b) Compliant 1, (c) Compliant 2, (d) Compliant 3, (e) Compliant 4, and (f) Compliant 5.

Variable Cutting Geometry

The needle tip was designed such that it could cut both parallel and perpendicular to the insertion direction. The needle tip is manufactured by grinding four planes. The tip geometry can be described by two angles: ξ and β. The manufacturing process is shown in Figure 4-4. The grind angle ξ is the tilt of the needle into the grind plane. The rotation angle β is defined as the rotation of the grind plane in the *X*-*Y* plane as can be seen in Step 3 in Figure 4-4. In Step 4, the needle is flipped 180° to grind the planes on the backside of the needle. For all the needles used in this study $\xi = 10°$ and $\beta = 20°$.

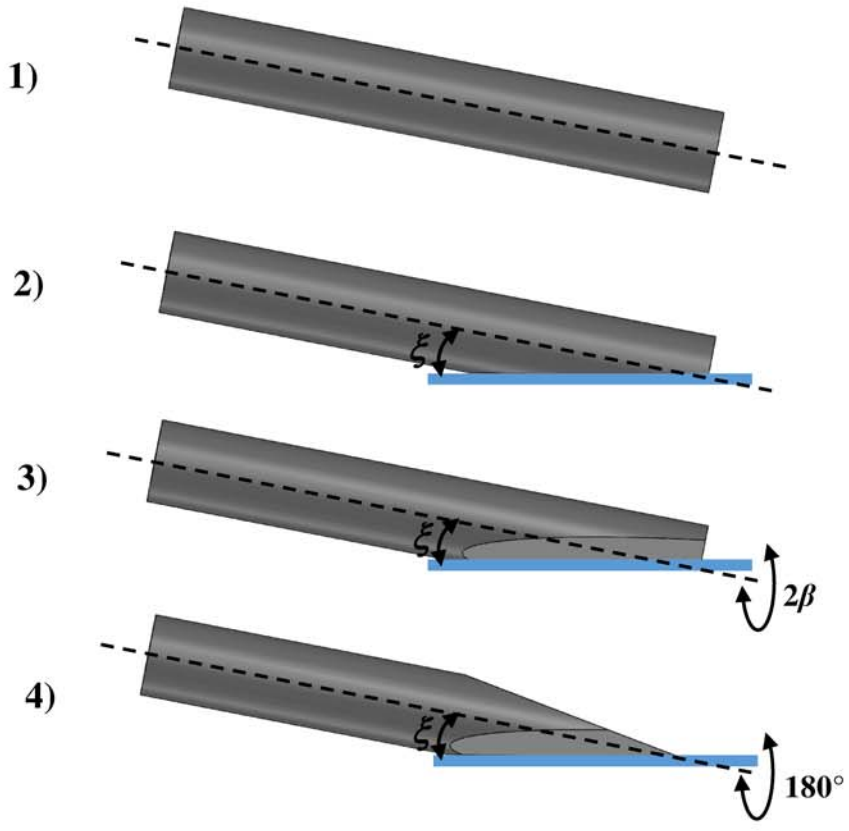

Figure 4-4. Description of manufacturing process of needle determined by grind angle ξ and rotation angle β.

Oblique cutting geometry is used in this study to describe the cutting geometry of the needle. Oblique cutting is utilized in manufacturing to characterize the cutting face of a tool and is defined by two angles: inclination and rake angles [27]. The definition of the inclination and rake angles of oblique cutting can be seen in Figure 4-5. The cutting edges of a needle can be described by oblique cutting geometry. Moore et al. shows the dependence of the insertion force of a needle on the rake and inclination angles of the tip [29]. A high inclination angle cuts with a lower force.

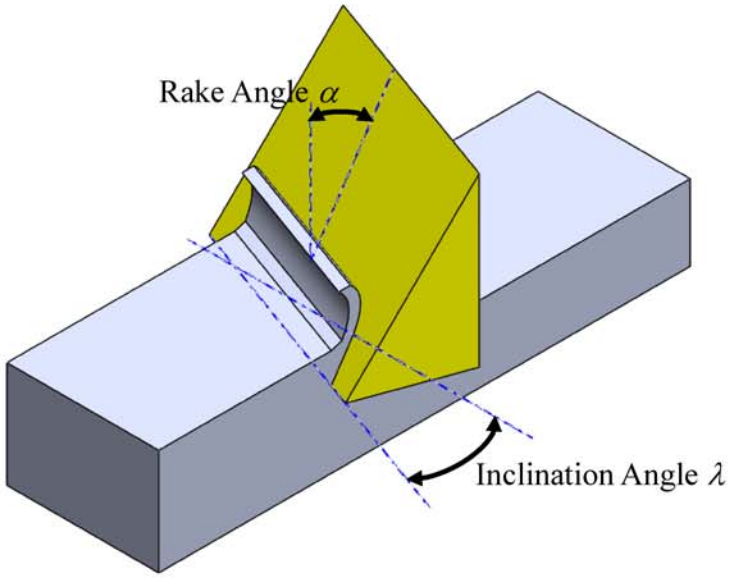

Figure 4-5. Definitions of rake and inclination angles in oblique cutting.

In this study, the rake and inclination angles of the cutting edge are defined based on the cutting direction. An *XYZ* coordinate system is created with the origin at the tip of the needle, the *Z*-axis is aligned with the axis of the needle pointing down the needle, and the *X*-axis aligned in the direction of the perpendicular cutting direction. Parametric equations are developed to describe the edges of the needle tip to calculate the angles. The three edges of one cutting plane are labelled in Figure 4-6. The parametric equations describing Edge 1 are:

$$x = 0$$

$$y = \psi \tag{24}$$

$$z = \psi \cos \beta \cot \xi$$

where the parameter ψ varies from 0 to r. The parametric equations for Edge 2 are:

$$x = r \sin \gamma$$

$$y = r \cos \gamma \tag{25}$$

$$z = r \cos (\gamma - \beta) \cot \xi$$

where γ is from 0° to 90° and is the radial angle describing the position along Edge 2 with respect to the Y-axis. The parametric equations for Edge 3 are:

$$x = \psi$$

$$y = 0 \tag{26}$$

$$z = \psi \sin \beta \cot \xi$$

where the parameter ψ goes from 0 to r. Edge 3 is the cutting edge for this needle geometry.

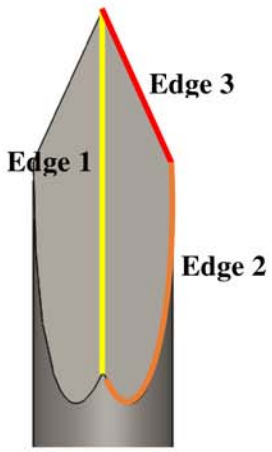

Figure 4-6. Edges of needle face.

The variable cutting direction can be described with the plane P_r which has a normal vector $\boldsymbol{v}$ in the cutting direction as shown in Figure 4-7. The normal vector is $\boldsymbol{v}$ = (sin $\theta(t)$, 0, -cos $\theta(t)$) where $\theta(t)$ is the rotation of the cutting direction in the XZ plane with $\theta = 0°$ being parallel to the insertion direction and $\theta = 90°$ being perpendicular to the insertion direction. Due to the nature of the motion of the needle tip, the cutting direction $\theta(t)$ varies with time t. The tangent vector $\boldsymbol{s}$ of the cutting edge for this geometry (Edge 3) is $\boldsymbol{s}$ = (-1, 0, -sin $\theta(t)$ cot ξ). The inclination angle $\lambda(t)$ in oblique cutting is defined as the angle between the plane P_r and the tangent vector of the cutting edge $\boldsymbol{s}$ as shown in Figure 4-7.

$$\lambda(t) = \arcsin\frac{|s \bullet v|}{\|s\|\|v\|} = \arcsin\frac{|\cos\theta(t)\sin\beta\cot\xi - \sin\theta(t)|}{\sqrt{1+\sin^2\beta\cot^2\xi}} \tag{27}$$

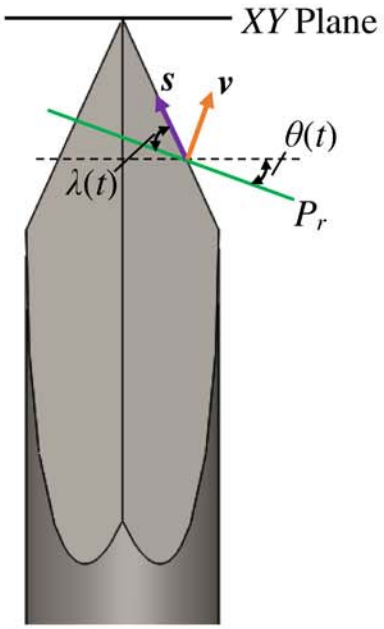

Figure 4-7. Inclination angle of needle tip with variable cutting direction.

The rake angle α in oblique cutting is defined as the angle between the needle face A_γ and plane P_r measured in the plane P_n as shown in Figure 4-8. The plane P_r is the defined as the plane

with a normal vector in the cutting direction, $\boldsymbol{v}$ = (sin $\theta(t)$, 0, -cos $\theta(t)$), and P_n is defined as the cutting edge normal plane. The normal vector of P_n is the tangent vector of the cutting edge, $\boldsymbol{s}$ = (-1, 0, -sin $\theta(t)$ cot ξ). The normal vector of the needle face A_γ is $\mathbf{n}_\gamma$ = (sin β cot ξ, cos β cot ξ, -1). The intersections of planes P_nA_γ and P_nP_r are vectors $\boldsymbol{a}$ and $\boldsymbol{b}$ respectively, as shown in Figure 4-8. The intersection vector of two planes is defined as the cross product of the normal vectors of the plane. $\boldsymbol{a}$ and $\boldsymbol{b}$ are defined as:

$$\boldsymbol{a} = \boldsymbol{s} \times \boldsymbol{n}_\gamma = (\sin\beta\cos\beta\cot^2\xi,\ 1 + \sin^2\beta\cot^2\xi,\ \cos\beta\cot\xi) \tag{28}$$

$$\boldsymbol{b} = \boldsymbol{s} \times \boldsymbol{v} = (0,\ \cos\theta(t) + \sin\theta(t)\sin\beta\cot\xi,\ 0) \tag{29}$$

The rake angle α, shown in Figure 4-8, is the angle between $\boldsymbol{a}$ and $\boldsymbol{b}$:

$$\alpha = \arccos\frac{|a \bullet b|}{\|a\|\|b\|} = \arccos\frac{\left|1+\sin^2\beta\cot^2\xi\right|}{\sqrt{\csc^2\xi\left(1+\sin^2\beta\cot^2\xi\right)}} \tag{30}$$

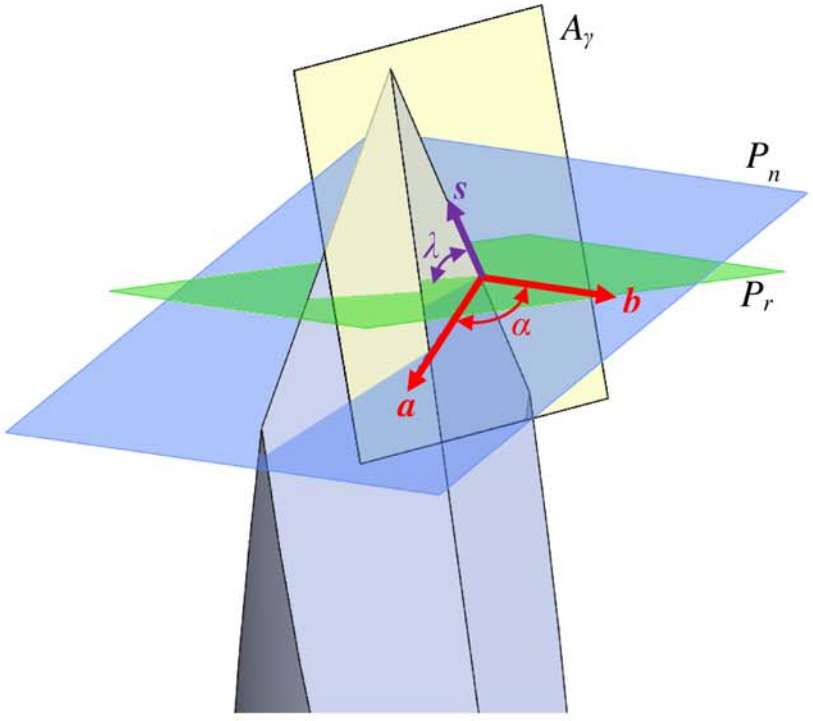

Figure 4-8. Rake angle of needle geometry.

As evident in Equations 27 and 30, the inclination angle is dependent on the needle cutting direction and the rake angle is independent of the cutting angle. The inclination angle and rake angle are plotted as a function of cutting direction in Figure 4-9. For this geometry, the highest inclination angle (most efficient cutting geometry) occurs when cutting parallel to the cutting direction ($\theta = 0$).

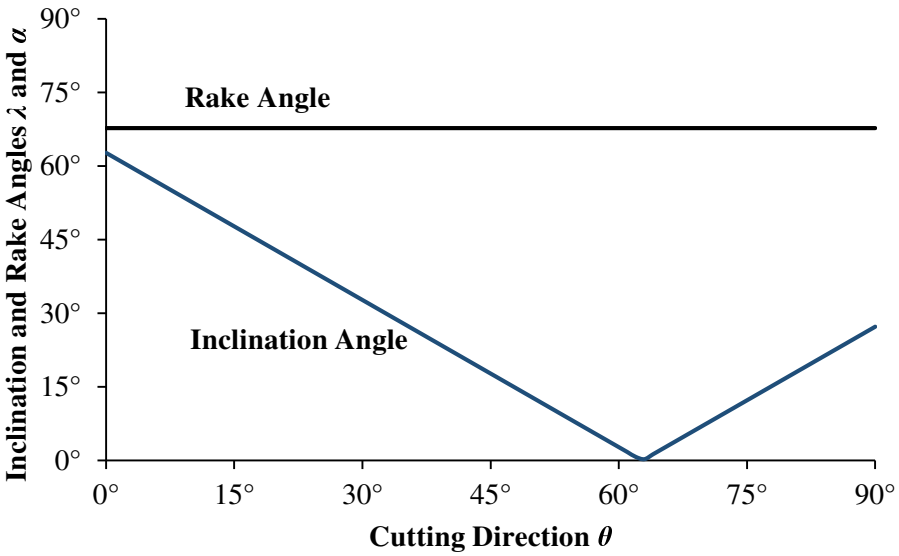

Figure 4-9. Effect of cutting direction θ on inclination angle λ and rake angle α.

Experimental Procedures

Needle cutting experiments were performed to determine the effects of the compliant geometry on the insertion force. The experiment utilized three needles. The needles used were the control needle, Compliant 1, and Compliant 2 as outlined in Table 4-1. Compliant 3 needle was not used in the experimental study due to it breaking from the stress caused by the vibration before a satisfactory amount of data could be collected. Compliant 4 and Compliant 5 needles were not manufactured. The needles were made out of 304 stainless steel and have the same diameter as an

18 gauge needle. The needles were inserted with an applied axial ultrasonic vibration of 20 kHz. The control needle was also inserted without applied vibration. The needles had a length of 127 mm to match the resonance of the ultrasonic transducer. The needles were inserted at a constant rate of 1 mm/s to isolate the effects of the vibration. The needles were inserted into a polyurethane sheet of Shore hardness 40A (Polyurethane Products, Addison, IL) and 1.588 mm thick. The polyurethane was used due to its consistency. Ex vivo tissue cutting experiments can yield results with standard deviations up to 25% [29] making it difficult to determine meaningful conclusions. Polyurethane has been used in other studies to simulate skin dermis [118, 119].

Ultrasonic Transducer

For this study, an ultrasonic vibration is applied to the needle in the axial direction. An ultrasonic piezoelectric transducer is used to apply the vibration. The piezoelectric ceramics in the transducer have a very low actuation length. However, the actuation length can be amplified if the frequency of actuation is the same as the axial resonance of the transducer. Because of this, ultrasonic transducers are limited to only being able to operate at one frequency. An ultrasonic horn can be used to amplify the vibration further.

An ultrasonic horn is a device which magnifies the amplitude of vibration, usually made from a high strength material such as stainless and hard steels, titanium and aluminum [129].The ultrasonic horn is a tapered bar of variable cross-section that connects to the transducer. The cross-sectional area of the input end (the end connected to the transducer) is generally larger than the area of the output end (the tool end of the horn). The length of the horn is determined by the axial resonance of the horn, usually a multiple of the half wavelength of the system [130]. For the horn to work, the axial resonance of the horn must match the axial resonance of the transducer. To

determine the length of the horn, the equation for longitudinal wave propagation through a homogeneous rod with variable cross-section is used (Equation 23) [128].

Three main shapes of horns are used in industry: conical, stepped, and exponential, examples of such can be seen in Figure 4-10. For this study, a stepped horn shape is used due to its ease of manufacturing. To reduce the stress in the horn, a short conical section is added in between the steps. The solution to Equation 23 for a stepped horn is given by:

$$L = k_1 \frac{c}{4f} + k_2 \frac{c}{4f} \tag{31}$$

Where L is the length of the horn, c is the wave propagation speed of the material which is defined as $c = \sqrt{E/\rho}$, f is the desired frequency of vibration, and k_1 and k_2 are correction factors. The correction factors can be assumed to be unity yielding [130]:

$$L = \frac{c}{2f} \tag{32}$$

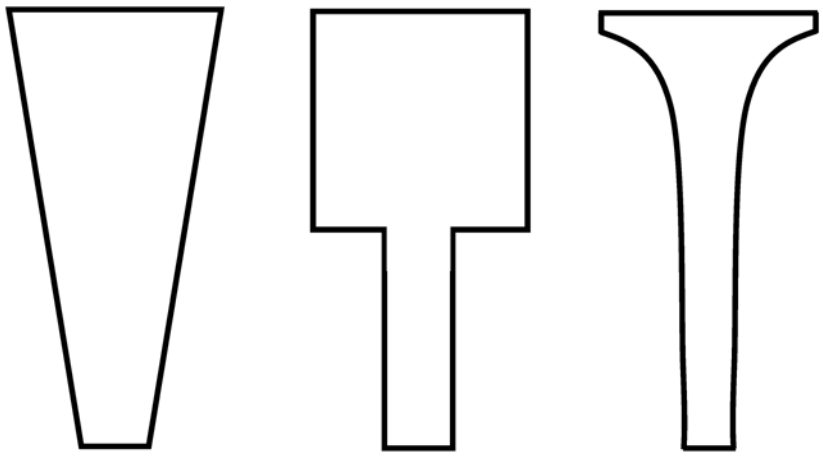

Figure 4-10. Various ultrasonic horn shapes: (a) conical, (b) stepped, (c) exponetial.

The horn used in this study was made of 6061 aluminum for its high strength and manufacturability (Young's modulus E = 68.9 MPa, density ρ = 2700 kg/m^3). The desired frequency of operation is 20 kHz. The approximate solution for the conical horn designed yields a length of 126.3 mm. To determine a more exact length, a finite element analysis was run utilizing ANSYS. Ten-node tetrahedron elements were used to mesh the three-dimensional horn geometry shown in Figure 4-11(a). The boundary conditions of the horn can be assumed to be free-free to achieve the half wavelength mode shape [130]. Using a modal analysis, the length of the horn was determined to be 128.3 mm to achieve the 20 kHz resonant frequency. Results of the analysis can be seen in Figure 4-11(b).

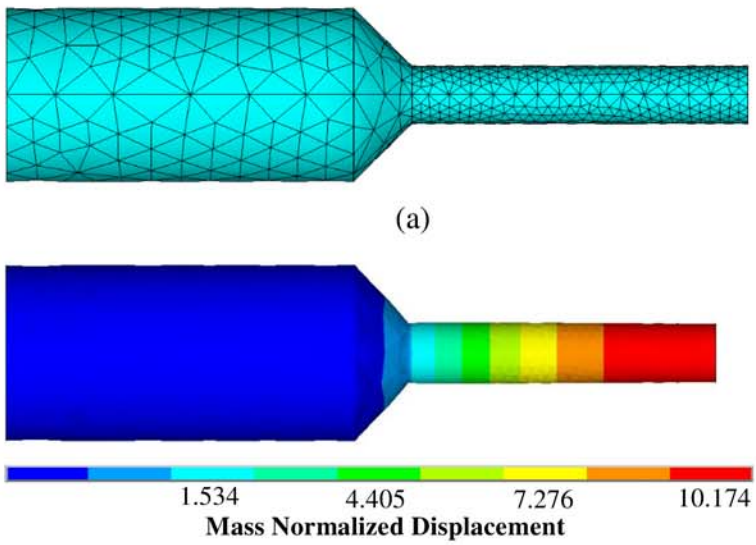

Figure 4-11. Finite element analysis (a) mesh and (b) modal results.

The stepped horn was manufactured to the length specified in the FE analysis and tested for its effectiveness. An optical probe (MTI Instruments, Albany, NY) was used to measure the displacement of the transducer with and without the ultrasonic horn attached. The displacement

results are plotted in Figure 4-12 for a 100 V peak-to-peak sine wave driving the transducer. The horn was able to amplify the vibration by 477% compared to the transducer without the horn.

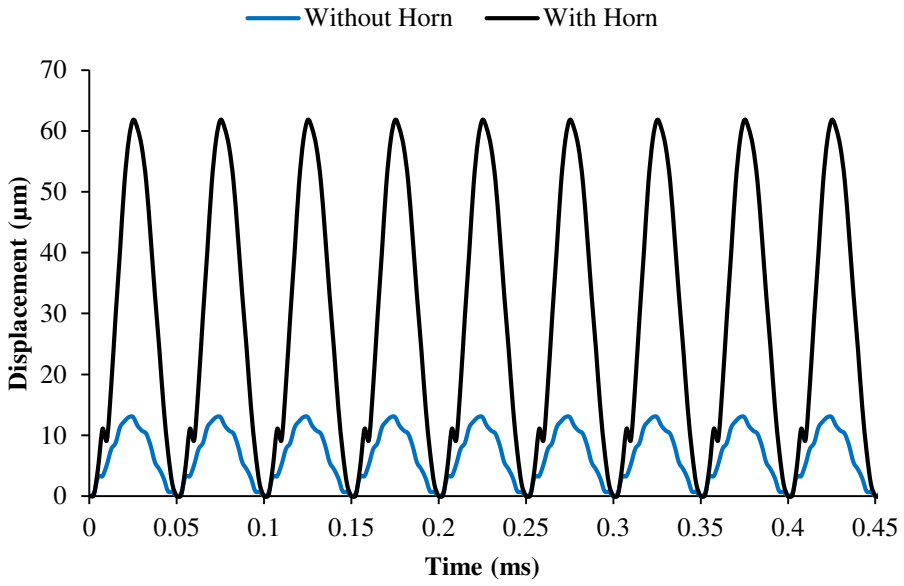

Figure 4-12. Displacement of ultrasonic transducer with and without horn.

Experimental Setup

The experimental setup shown in Figure 4-13 was utilized to perform the insertion tests. A linear motor (Dunkermotoren, Bonndorf, Germany) is used to insert the needles into the polyurethane at a constant rate of 1 mm/s. The force was recorded with a six-axis force sensor (ATI Industries, Apex, NC). A 20 kHz piezoelectric transducer (Honda Electronics, Toyohashi, Japan) applies axial ultrasonic vibration to the needle. The polyurethane is mounted between two plates to ensure constant boundary conditions for each trial.

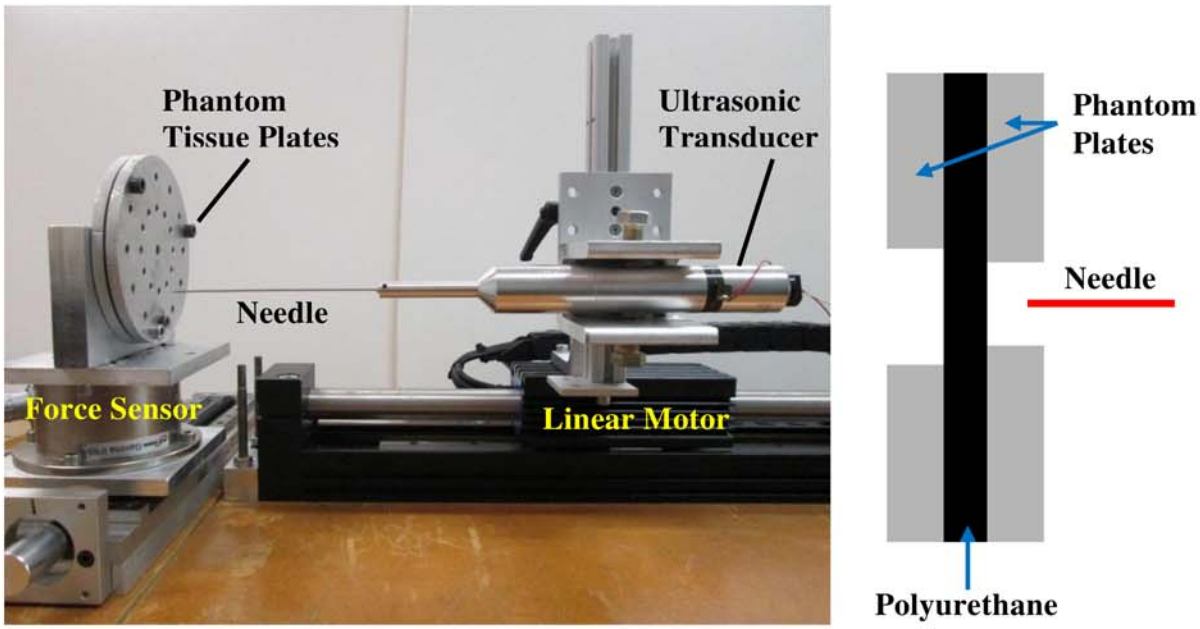

Figure 4-13. Experimental setup utilized to test the compliant needles.

Results

Compliant Needle Motion

To determine the effects of the compliant geometry on the motion of the needles, the displacements of the tips were measured using a stereo microscope (Zeiss, Oberkochen, Germany). Images were captured for each needle with and without vibration applied. The motion of the tip was determined by the ghost image in the capture, as shown in Figure 4-14(b,c). Figure 4-14(a,b) shows the needle tip of Compliant Needle 2 with and without vibration applied. The motion can be tracked by measuring the displacement of the reflected bright spots caused by surface textures shown in Figure 4-14(b). The exposure time for the images was 10 ms. At 20 kHz frequency, this allowed for 200 cycles to be captured in each image, ensuring the capture of the full range of motion.

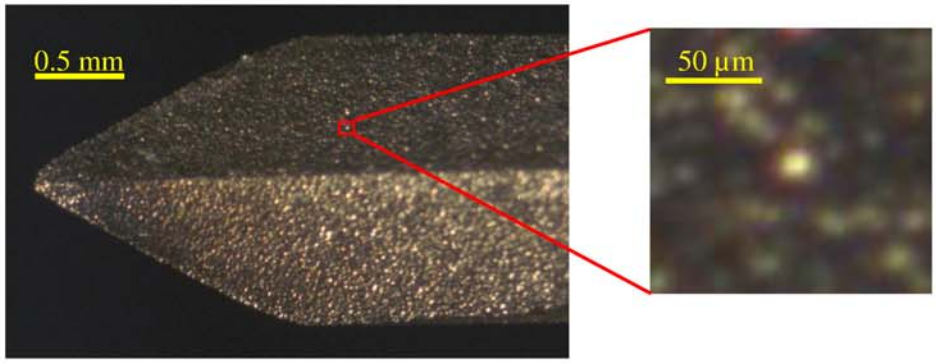

(a)

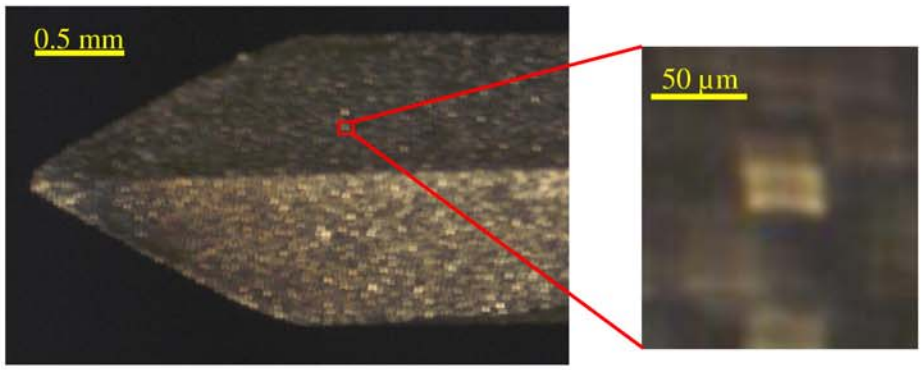

(b)

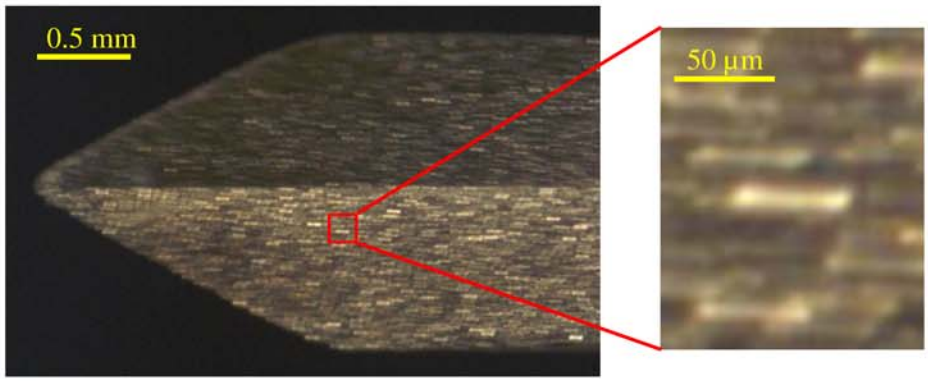

(c)

Figure 4-14. Image of (a) compliant needle without applied vibration, (b) compliant needle with applied vibration, and (c) control needle with applied vibraiton.

The motion was recorded for each of the three needles used in this study. The control needle only had motion in the axial direction of the vibration shown in Figure 4-14(c) and Table 4-3. The

ghost image only showed the reflected dots moving only along the axis of the needle. However, the compliant geometries had motion in both the axial direction and the transverse direction. The transverse motion is evident in Figure 4-14(b) by the square pattern of the reflected dot's ghost image. Compliant Needle 2 (slits farther apart) had more transverse motion than Compliant Needle 1 as shown in Table 4-3. The values were only measured once for each needle due to the constraints of the microscope.

Table 4-3. Displacement of needle tip in the axial and transverse direction due to applied axial vibration.

	Axial (μm)	**Transverse (μm)**
Control	52.3	0
Compliant 1	43.2	4.55
Compliant 2	32.9	16.0

The motion of the tip caused by the vibration is neither pure axial or transverse. The square-patterned motion causes the inclination angle of the cutting to change with time. For the needles used in this study, the rake angle is 67.7° from Equation 30. The inclination angle, calculated from Equation 27, is 62.7° in the axial direction and 27.27° in the transverse direction. Further work is needed to optimize the cutting motion created by the compliant geometry with the cutting edge geometry.

Force Results

Force and position data was collected for each trial. An example plot can be seen in Figure 4-15, showing the insertion forces for the control needle with and without vibration and Compliant Needle 1 with vibration. The puncture force is the force at the first peak of the insertion plot. Prior

to the peak, the needle is only deflecting the polyurethane, no cutting is occurring. At the peak where the puncture force is recorded, a crack is initiated and the needle begins to cut through the material. The friction force is taken to be the force between the needle and the polyurethane once the needle tip has exited the polyurethane as shown in Figure 4-15.

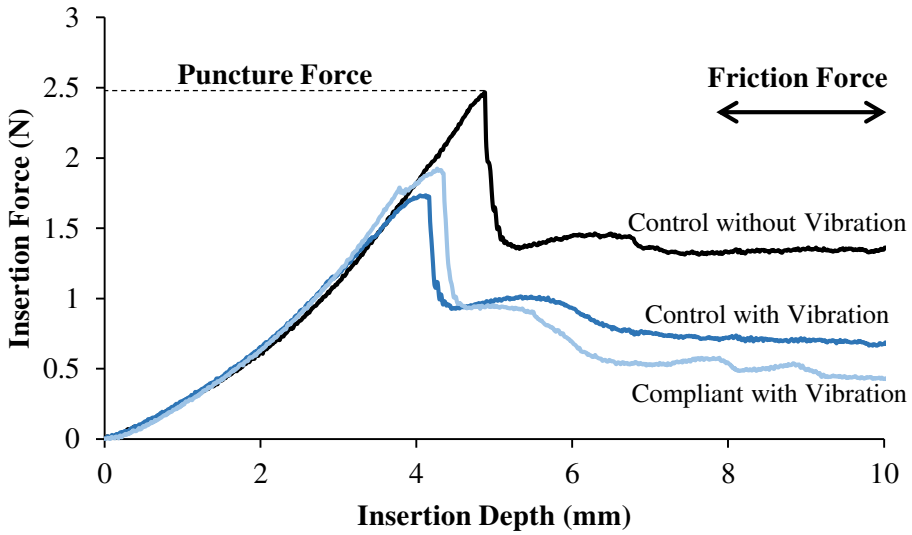

Figure 4-15. Insertion mechanics of control and compliant needles into polyurethane.

The puncture force and friction force were recorded for the control needle with and without applied vibration and also for the two compliant needles with vibration. Using single factor ANOVA tests, the results, shown in Figure 4-16, show a significant decrease in puncture force for the trials with applied vibration for both the control needle and the compliant needles compared to the control insertion with no vibration (M = 2.44, SD = 0.040). The control needle with vibration (M = 1.72, SD = 0.019) reduced the puncture force by 29.5%, $F(1,4) = 810.65$, $p < 0.001$, where Compliant 1 (M = 1.99, SD = 0.071) reduced the puncture force by 18.8%, $F(1,6) = 102.65$, $p < 0.001$, and Compliant 2 (M = 2.10, SD = 0.171) reduced by 14.1%, $F(1,6) = 11.24$, $p = 0.02$, compared to the control insertion with no vibration. The control needle with vibration added had

the lowest puncture force. This could be due to the control needle having the largest axial amplitude of vibration. The puncture forces for the two compliant needles are insignificantly different from each other, $F(1,8) = 1.88$, $p = 0.21$. The standard deviation of the puncture force is much lower in the polyurethane (at most 8%) than with insertion into biological tissue (on average 19% for hypodermic needles into ex vivo porcine skin). Compliant 2 had the highest standard deviation in the puncture force.

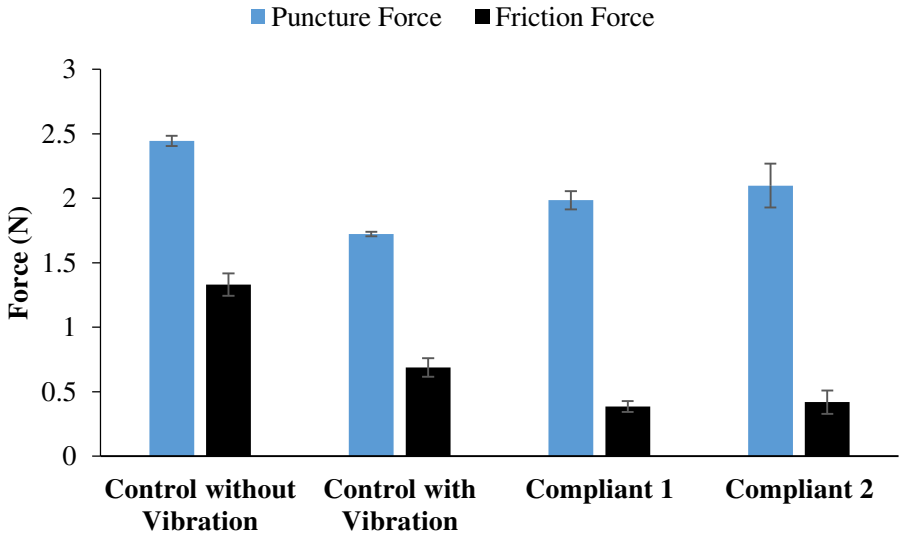

Figure 4-16. Puncture and friction force results for the needles used in this study.

The friction force between the needle and the polyurethane was significantly reduced, determined by single factor ANOVA tests, with the applied vibration for the control needle and two compliant needles compared to the control needle with no applied vibration ($M = 1.33$, $SD = 0.087$). The control needle with applied vibration ($M = 0.69$, $SD = 0.072$) reduced the friction force by 48.3%, $F(1,4) = 96.87$, $p < 0.001$, where Compliant 1 ($M = 0.39$, $SD = 0.042$) reduced the friction force 71.0%, $F(1,6) = 447.85$, $p < 0.001$, and Compliant 2 ($M = 0.42$, $SD = 0.090$) reduced the friction force by 68.4%, $F(1,5) = 109.72$, $p < 0.001$. Similar to the puncture force results, the friction

force of the two compliant needles is insignificantly different from each other, $F(1,8) = 1.67$, $p = 0.23$.

To determine the cause of the decrease in friction force of the compliant needles to the control needle, the cracks created in the polyurethane from the needles were examined. The cracks from the control needle with and without applied vibration as well as the cracks from the compliant needle with and without applied vibration can be seen in Figure 4-17 (a-d) respectively. As can be seen, the compliant needle when vibration is applied creates a larger, more complex crack. The average crack lengths are shown in Figure 4-18. The control insertion had an average crack length of 804.7 µm (*SD* = 195.4) where the compliant needle with vibration had an average crack length of 2331.2 µm (*SD* = 491.7). The larger crack allows the needle to pass through the polyurethane without having to stretch the polyurethane as much as a smaller crack. This reduces the normal force the polyurethane exerts on the needle, thus reducing the friction force. The larger standard deviation of the compliant needle with applied vibration was the highest of the four cases. This is due to the complex shape of the crack varying more from trial to trial than the straight cuts from the control needle. This higher standard deviation in crack size affects the variance of the friction force, as the Compliant 2 friction force standard deviation was highest for all the cases.

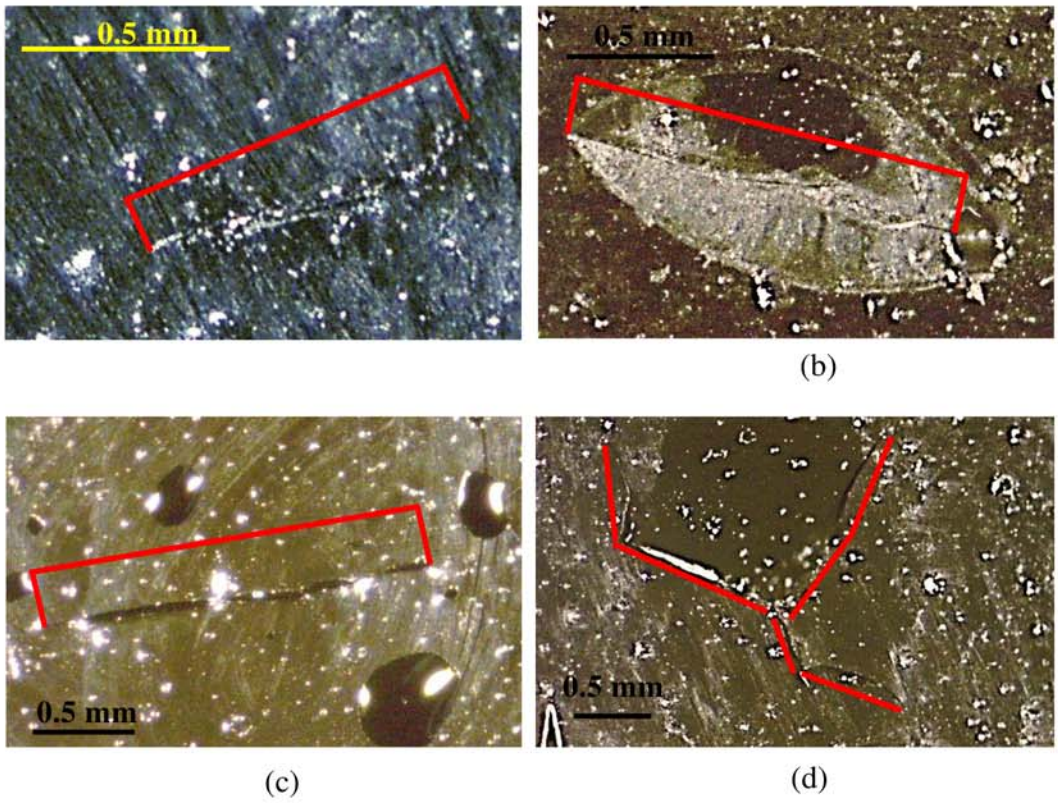

Figure 4-17. Cracks formed by (a) control needle with no vibration, (b) control needle with vibration, (c) compliant needle with no vibration, and (d) compliant needle with vibration.

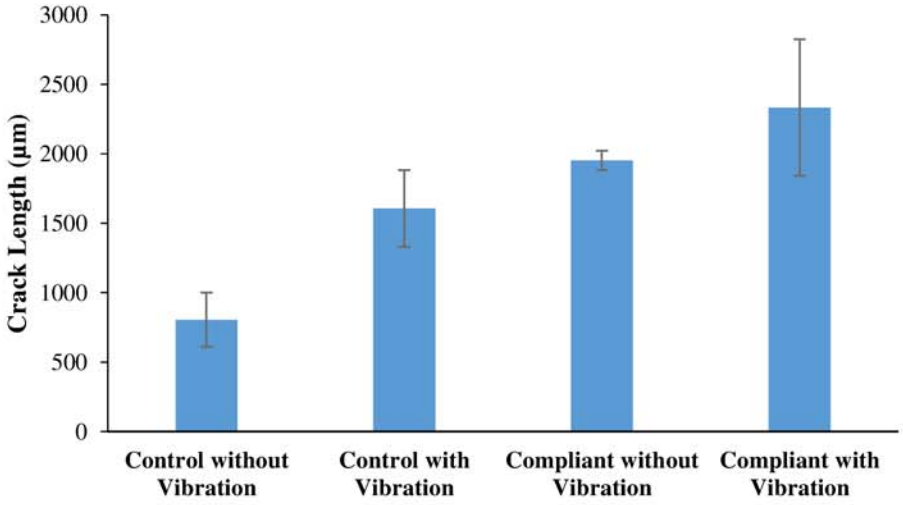

Figure 4-18. Crack lengths formed by needle insertion.

Concluding Remarks

A novel compliant needle was presented in this chapter. The compliant geometry utilized vibration to transform axial motion into transverse motion. To achieve this, the geometry of the needle was constructed such that the axial mode shape of the needle when vibrated at resonance now has transverse motion as well. This is a novel approach to cutting tissue.

In this chapter, the design of the needle was described and a finite element analysis of its motion was performed. The variable cutting geometry of the needle tip was also defined. Experiments were conducted to determine the effectiveness of a novel compliant needle geometry at reducing insertion forces. The compliant needles were able to reduce the puncture force of the insertion by 18.8% and the friction force by 71.0% compared to the control needle without vibration. Although the vibration applied to the control needle outperformed the compliant needles in reducing the puncture force, the compliant needles were able to reduce the friction force by the greatest amount. As shown in the previous chapter, the friction force increases as the needle is inserted further into the tissue. Therefore reducing the friction force can have a significant impact on reducing total needle insertion force for deeply placed needles.

Further design of the compliant and cutting geometries is needed to improve the performance of the compliant needles. This study presented evidence of the compliant geometry causing transverse motion of the needle tip. The transverse motion was shown to change the cutting mechanics of insertion by increasing and changing the shape of the crack created in the phantom tissue. Currently, the compliant needle is being outperformed by the non-compliant control needle with vibration applied in reducing the initial puncture force. To achieve better performance than the control needle, further work will need to be performed to optimize the compliant geometry. In addition, the cutting geometry of the needle can be further developed to cut the most efficiently for the complex motion of the compliant needle tip.

Chapter 5

Conclusions and Future Work

Needles are commonly used in minimally invasive procedures; however, complications still are prevalent with these procedures due to high insertion forces acting on the needle causing misplacement inside the body. This can lead to ineffective treatment and many adverse side effects, which lower patient quality of life and increase healthcare costs. Many methods have been studied to reduce the insertion force including using smaller diameter needles, altering the tip geometry, and utilizing the dynamic insertion methods of increased insertion speed and applied needle vibration. However, current state of the art needle cutting technology and research lacks an understanding of the specific impact velocity and vibration have on needle force and how needle tip geometry impacts vibrational cutting force. This lack of knowledge has led to dynamic insertion methods not being widely and effectively used in medical procedures. This dissertation contributes to the understanding of dynamic needle insertion by addressing how dynamic parameters (insertion speed, amplitude, and frequency of vibration) and needle geometry affect the insertion forces.

The major contributions of this dissertation are:

- **A velocity dependent fracture mechanics force model was successfully developed**. Previous force models did not describe how the velocity dependence of tissue properties contributes to the total insertion force. This is addressed in Chapter 2 by developing a fracture mechanics model that successfully determines how tissue properties, insertion speed, and needle gauge specifically impact the total insertion force. The parameters of tissue fracture toughness, tissue shear modulus, crack size caused by the needle, and friction force between the needle and the tissue were experimentally determined. For the study, tough porcine skin was utilized. It was found that the fracture toughness was not dependent on speed. The shear modulus reduced as speed increased due to shear thinning. Friction force increased with higher

insertion speed. Overall the insertion speed caused no significant change in the total insertion force in the tough porcine skin. The benefit of increasing insertion speed is more evident in softer tissues of organs and muscles, where there is a lower velocity impact to friction. The fracture mechanics model provided insight into why the reduction of force was not observed in the porcine skin. The fracture mechanics model allowed for the breakdown of the component forces of insertion showing that for porcine skin; 70% of the total insertion force comes from tearing the tissue (determined by the fracture toughness), 13% is due to spreading the tissue to accommodate the needle (determined by the shear modulus), and 17% is due to the friction between the tissue and the needle. Therefore the higher velocity benefits to the shear modulus were offset by the disadvantage of higher friction in tough porcine skin.

- **The effectiveness of vibration at reducing tissue cutting was discovered to be strongly dependent on needle geometry.** Previous research on vibration needle tissue cutting does not explore how geometry affects insertion force. This dissertation in Chapter 3 determines which needle geometries are most suited for vibration tissue cutting. Experiments were performed to determine how vibratory parameters (amplitude and frequency) affect the insertion force of different sized hypodermic needles (commonly used needle in many medical procedures). It was found that vibration was able to reduce the insertion force by up to 35% on these sharp needles. The smaller gauge needles had the lowest insertion forces at the highest frequencies, which is hypothesized to be due to the strain rate sensitivities of the tissue described in Chapter 2. Blunt needles aimed at reducing the number of accidental needlestick injuries that occur during procedures were then developed. The blunt needle experiments showed that vibration was able to reduce insertion force by only 17%, half that of the sharp needles. To further evaluate the needle geometry effect on vibratory insertion force, an in depth study was performed with conical needles. These needles were developed with varying grind angles to isolate the effects of geometry. In bovine liver experiments vibration reduced the insertion force

by up to 67.7% for the sharpest needle, bevel angle of 15°, and there was on average no significant reduction in force for the bluntest needle, bevel angle of 75°. Relatively large standard deviations were observed in the insertion force results due to the large variance in ex vivo tissue. The bovine liver results were validated with experiments into a polyurethane sheet. The sharpest needle saw a reduction in the force needed to propagate the crack in the material during the steady cutting phase whereas the blunt needle punctured through in a short period of time, not having a steady cutting phase.

- **A novel compliant needle geometry that utilizes vibration to reduce the insertion force was designed and developed.** The needle uses the novel approach of designed compliance to turn axial vibration into transverse motion. In Chapter 4 experiments were performed to determine the effectiveness of the compliant geometry. The motion of the needle tip was measured and showed 16.0 microns of motion in the transverse direction versus 32.9 microns in the axial direction. The puncture force for the compliant needle into polyurethane material was reduced 18.8% over the control insertion with no compliant geometry and no applied vibration. The friction force was reduced by 71.0% over the control insertion. The compliant needle created a larger crack upon insertion which reduced the normal force on the needle, thereby reducing the friction.

Limitations and Recommendations for Future Work

This dissertation furthered the understanding of dynamic needle insertion. There are areas of research that could extend from the work presented in this dissertation. Recommended future avenues of work are as follows:

- The fracture mechanics insertion model could be expanded to softer tissues. In Chapter 2, the fracture mechanics insertion model was only tested on porcine skin. The

insertion model can be used with any material. A study on the properties of a soft tissue (bovine liver for example) would be worthwhile. This would allow for the determination of why the insertion force into soft tissues reduces with increased insertion speeds whereas the insertion force remains constant with increased insertion speeds into tougher materials. This study can be used to determine the optimal insertion speed throughout a variety of tissues.

- The fracture mechanics insertion model can be expanded to tissue-mimicking synthetic materials. The creation of force models using biological tissue is difficult due the variance of the tissue as demonstrated in this study. Phantom tissue is useful in determining the performance of needles and insertion methods because of its consistency and shelf life. However, determining whether the phantom tissue results are representative of results from in vivo or ex vivo tissue is difficult. A synthetic material study using the fracture mechanics insertion model can determine how various force components quantitatively compare to those of in vivo or ex vivo tissue. This can be used to select or develop an accurate phantom tissue material.
- The vibratory parameter study can be expanded to include ultrasonic frequencies. The parameter study performed in this work utilized only auditory vibration which was shown to reduce the insertion force. However, when ultrasonic vibration was applied to the control needle in the compliant vibration study, a significant reduction in force was observed. Ultrasonic vibration can be studied to determine its effectiveness on insertion forces. A vibratory parameter study can be performed to determine how different ultrasonic vibrations have different effects on the insertion force.
- The geometry of the compliant needle can be further optimized to reduce insertion force. The compliant needle was shown to have transverse motion and change the cutting mechanics of the needle. However, the control needle outperformed the

compliant needle in reducing the puncture force. Further work is needed to optimize the compliant geometry to increase the transverse motion. Part of the optimization study will be to determine the stresses in the needle. Compliant needle 3 broke under fatigue stress. Calculating the stress in the needles will determine the limits of needle motion. In addition, the cutting geometry can be optimized to work best with the optimized motion.

The work presented in this dissertation has led to a better understanding of dynamic needle insertions, including the creation of a novel needle geometry. This research along with continuing research on increasing insertion speed and vibratory tissue cutting will lead to these techniques being utilized by medical professionals during procedures. Dynamic needle insertion has the potential to greatly increase needle placement accuracy in numerous procedures, thereby improving procedure efficacy and patient quality of life.

References

[1] Y. J. Hutin, A. M. Hauri, and G. L. Armstrong, "Use of injections in healthcare settings worldwide, 2000: literature review and regional estimates," *Bmj,* vol. 327, p. 1075, 2003.

[2] A. Zivanovic and B. L. Davies, "A robotic system for blood sampling," *Ieee Transactions on Information Technology in Biomedicine,* vol. 4, pp. 8-14, Mar 2000.

[3] M. R. Prausnitz, S. Mitragotri, and R. Langer, "Current status and future potential of transdermal drug delivery," *Nature Reviews Drug Discovery,* vol. 3, pp. 115-124, Feb 2004.

[4] S. Kang, D. Goodnough, Y. Lee, R. Olson, J. Borshoff, M. Furlano*, et al.*, "Comparison of 26-and 27-G needles for spinal anesthesia for ambulatory surgery patients," *Anesthesiology,* vol. 76, pp. 734-738, 1992.

[5] F. Piccinino, E. Sagnelli, G. Pasquale, and G. Giusti, "Complications Following Percutaneous Liver-Biopsy - a Multicenter Retrospective Study on 68 276 Biopsies," *Journal of Hepatology,* vol. 2, pp. 165-173, 1986.

[6] N. Abolhassani, R. Patel, and M. Moallem, "Needle insertion into soft tissue: A survey," *Medical engineering & physics,* vol. 29, pp. 413-431, 2007.

[7] S. Nath, Z. Chen, N. Yue, S. Trumpore, and R. Peschel, "Dosimetric effects of needle divergence in prostate seed implant using I-125 and Pd-103 radioactive seeds," *Medical Physics,* vol. 27, pp. 1058-1066, May 2000.

[8] J. H. Youk, E.-K. Kim, M. J. Kim, J. Y. Lee, and K. K. Oh, "Missed Breast Cancers at US-guided Core Needle Biopsy: How to Reduce Them 1," *Radiographics,* vol. 27, pp. 79-94, 2007.

[9] J. A. Talcott, J. A. Clark, P. C. Stark, and S. P. Mitchell, "Long-term treatment related complications of brachytherapy for early prostate cancer: A survey of patients previously treated," *Journal of Urology,* vol. 166, pp. 494-499, Aug 2001.

[10] D. C. Miller, M. G. Sanda, R. L. Dunn, J. E. Montie, H. Pimentel, H. M. Sandler*, et al.*, "Long-term outcomes among localized prostate cancer survivors: Health-related quality-of-life changes after radical prostatectomy, external radiation, and brachytherapy," *Journal of Clinical Oncology,* vol. 23, pp. 2772-2780, Apr 20 2005.

[11] Y. Yu, L. L. Anderson, Z. F. Li, D. E. Mellenberg, R. Nath, M. C. Schell*, et al.*, "Permanent prostate seed implant brachytherapy: Report of the American Association of Physicists in Medicine Task Group No. 64," *Medical Physics,* vol. 26, pp. 2054-2076, Oct 1999.

[12] S. F. Shariat and C. G. Roehrborn, "Using biopsy to detect prostate cancer," *Rev Urol,* vol. 10, p. 262, 2008.

[13] H. Q. Li, P. M. Boiselle, J. A. O. Shepard, B. TrotmanDickenson, and T. C. McLoud, "Diagnostic accuracy and safety of CT-Guided percutaneous needle aspiration biopsy of the lung: Comparison of small and large pulmonary nodules," *American Journal of Roentgenology,* vol. 167, pp. 105-109, Jul 1996.

[14] H. Tsukada, T. Satou, A. Iwashima, and T. Souma, "Diagnostic accuracy of CT-guided automated needle biopsy of lung nodules," *American Journal of Roentgenology,* vol. 175, pp. 239-243, Jul 2000.

[15] R. Siegel, D. Naishadham, and A. Jemal, "Cancer statistics, 2013," *CA: a cancer journal for clinicians,* vol. 63, pp. 11-30, 2013.
[16] J. C. Blasko, T. Mate, J. E. Sylvester, P. D. Grimm, and W. Cavanagh, "Brachytherapy for carcinoma of the prostate: techniques, patient selection, and clinical outcomes," *Semin Radiat Oncol,* vol. 12, pp. 81-94, Jan 2002.
[17] A. T. Porter, J. C. Blasko, P. D. Grimm, S. M. Reddy, and H. Ragde, "Brachytherapy for prostate cancer," *CA Cancer J Clin,* vol. 45, pp. 165-78, May-Jun 1995.
[18] G. Strassmann, P. Olbert, A. Hegele, D. Richter, E. Fokas, N. Timmesfeld*, et al.*, "Advantage of robotic needle placement on a prostate model in HDR brachytherapy," *Strahlenther Onkol,* vol. 187, pp. 367-72, Jun 2011.
[19] G. Fichtinger, J. P. Fiene, C. W. Kennedy, G. Kronreif, I. Iordachita, D. Y. Song*, et al.*, "Robotic assistance for ultrasound-guided prostate brachytherapy," *Medical Image Analysis,* vol. 12, pp. 535-545, Oct 2008.
[20] N. N. Stone and R. G. Stock, "Complications following permanent prostate brachytherapy," *Eur Urol,* vol. 41, pp. 427-433, Apr 2002.
[21] B. T. Sitzman and D. R. Uncles, "The effects of needle type, gauge, and tip bend on spinal needle deflection," *Anesthesia & Analgesia,* vol. 82, pp. 297-301, 1996.
[22] D. Glozman and M. Shoham, "Image-guided robotic flexible needle steering," *Robotics, IEEE Transactions on,* vol. 23, pp. 459-467, 2007.
[23] R. Alterovitz, K. Goldberg, J. Pouliot, R. Taschereau, and I. C. Hsu, "Sensorless planning for medical needle insertion procedures," *Iros 2003: Proceedings of the 2003 Ieee/Rsj International Conference on Intelligent Robots and Systems, Vols 1-4,* pp. 3337-3343, 2003.
[24] S. P. DiMaio and S. E. Salcudean, "Needle insertion modeling and simulation," *Ieee Transactions on Robotics and Automation,* vol. 19, pp. 864-875, Oct 2003.
[25] Y. R. J. van Veen, A. Jahya, and S. Misra, "Macroscopic and microscopic observations of needle insertion into gels," *Proceedings of the Institution of Mechanical Engineers Part H-Journal of Engineering in Medicine,* vol. 226, pp. 441-449, 2012.
[26] H. Egekvist, P. Bjerring, and L. Arendt-Nielsen, "Pain and mechanical injury of human skin following needle insertions," *European Journal of Pain,* vol. 3, pp. 41-49, 1999.
[27] G. K. Boothroyd, Winston A., *Fundamentals of Machining and Machine Tools*, Third Edition ed. Boca Raton, FL: Taylor & Francis, 2006.
[28] J. Z. Moore, K. Malukhin, A. J. Shih, K. F. Ehmann, and S. Malkin, "Hollow needle tissue insertion force model," *Cirp Annals-Manufacturing Technology,* vol. 60, pp. 157-160, 2011.
[29] J. Z. Moore, A. J. Shih, P. McLaughlin, C. McGill, Q. Zhang, and H. Zheng, "Blade oblique cutting of tissue for investigation of biopsy needle insertion," *Trans. NAMRI/SME,* vol. 37, pp. 49-56, 2009.
[30] M. A. Towler, W. McGregor, G. T. Rodeheaver, P. V. Cutler, R. F. Bond, D. Phung*, et al.*, "Influence of cutting edge configuration on surgical needle penetration forces," *J Emerg Med,* vol. 6, pp. 475-81, Nov-Dec 1988.
[31] T. Podder, D. Clark, J. Sherman, D. Fuller, E. Messing, D. Rubens*, et al.*, "Effects of tip geometry of surgical needles: an assessment of force and deflection," in *IFMBE Proc*, 2005, pp. 1727-1983.
[32] Y. C. Wang, R. K. Chen, B. L. Tai, P. W. McLaughlin, and A. J. Shih, "Optimal needle design for minimal insertion force and bevel length," *Medical Engineering & Physics,* vol. 36, pp. 1093-1100, Sep 2014.

[33] Y. C. Wang, B. L. Tai, R. K. Chen, and A. J. Shih, "The Needle With Lancet Point: Geometry for Needle Tip Grinding and Tissue Insertion Force," *Journal of Manufacturing Science and Engineering-Transactions of the Asme,* vol. 135, Aug 2013.

[34] Y. C. Wang, R. K. Chen, B. L. Tai, and A. J. Shih, "Advanced Five-Plane Lancet Needle Design, Grinding, and Tissue Insertion," *Proceedings of the Asme 9th International Manufacturing Science and Engineering Conference, 2014, Vol 2,* 2014.

[35] L. Vedrine, W. Prais, P. E. Laurent, C. Raynal-Olive, and M. Fantino, "Improving needle-point sharpness in prefillable syringes," *Med Device Technol,* vol. 14, pp. 32-5, May 2003.

[36] J. L. Doyle and S. L. Koziol, "Five beveled point geometry for a hypodermic needle," ed: Google Patents, 1998.

[37] L. Hirsch, M. Gibney, J. Berube, and J. Manocchio, "Impact of a modified needle tip geometry on penetration force as well as acceptability, preference, and perceived pain in subjects with diabetes," *Journal of diabetes science and technology,* vol. 6, pp. 328-335, 2012.

[38] S. P. Davis, B. J. Landis, Z. H. Adams, M. G. Allen, and M. R. Prausnitz, "Insertion of microneedles into skin: measurement and prediction of insertion force and needle fracture force," *Journal of Biomechanics,* vol. 37, pp. 1155-1163, Aug 2004.

[39] S. Kaushik, A. H. Hord, D. D. Denson, D. V. McAllister, S. Smitra, M. G. Allen*, et al.*, "Lack of pain associated with microfabricated microneedles," *Anesthesia and Analgesia,* vol. 92, pp. 502-504, Feb 2001.

[40] S. P. Davis, W. Martanto, M. G. Allen, and M. R. Prausnitz, "Hollow metal microneedles for insulin delivery to diabetic rats," *Ieee Transactions on Biomedical Engineering,* vol. 52, pp. 909-915, May 2005.

[41] J. H. Park, Y. K. Yoon, S. O. Choi, M. R. Prausnitz, and M. G. Allen, "Tapered conical polymer microneedles fabricated using an integrated lens technique for transdermal drug delivery," *Ieee Transactions on Biomedical Engineering,* vol. 54, pp. 903-913, May 2007.

[42] S. P. Sullivan, D. G. Koutsonanos, M. D. Martin, J. W. Lee, V. Zarnitsyn, S. O. Choi*, et al.*, "Dissolving polymer microneedle patches for influenza vaccination," *Nature Medicine,* vol. 16, pp. 915-U116, Aug 2010.

[43] P. Van Damme, F. Oosterhuis-Kafeja, M. Van der Wielen, Y. Almagor, O. Sharon, and Y. Levin, "Safety and efficacy of a novel microneedle device for dose sparing intradermal influenza vaccination in healthy adults," *Vaccine,* vol. 27, pp. 454-459, Jan 14 2009.

[44] Y. C. Kim, J. H. Park, and M. R. Prausnitz, "Microneedles for drug and vaccine delivery," *Advanced Drug Delivery Reviews,* vol. 64, pp. 1547-1568, Nov 2012.

[45] M. Heverly, P. Dupont, and J. Triedman, "Trajectory optimization for dynamic needle insertion," *2005 Ieee International Conference on Robotics and Automation (Icra), Vols 1-4,* pp. 1646-1651, 2005.

[46] Y. Kobayashi, T. Sato, and M. G. Fujie, "Modeling of Friction Force based on Relative Velocity between Liver Tissue and Needle for Needle Insertion Simulation," *2009 Annual International Conference of the Ieee Engineering in Medicine and Biology Society, Vols 1-20,* pp. 5274-5278, 2009.

[47] N. Abolhassani, R. Patel, and M. Moallem, "Trajectory generation for robotic needle insertion in soft tissue," *Proceedings of the 26th Annual International Conference of the Ieee Engineering in Medicine and Biology Society, Vols 1-7,* vol. 26, pp. 2730-2733, 2004.

[48] T. B. Frick, D. D. Marucci, J. A. Cartmill, C. J. Martin, and W. R. Walsh, "Resistance forces acting on suture needles," *Journal of Biomechanics,* vol. 34, pp. 1335-1340, Oct 2001.

[49] W. Koelmans, G. Krishnamoorthy, A. Heskamp, J. Wissink, S. Misra, and N. Tas, "Microneedle characterization using a double-layer skin simulant," *Mechanical Engineering Research,* vol. 3, p. p51, 2013.

[50] G. Nishimura, Y. Jimbo, and S. Shimakawa, "Ultrasonic Machining-Part I," *J. Fac. Eng., Univ. Tokyo,* vol. 24, pp. 65-100, 1954.

[51] H. Suzuki and H. Yagishita, "Burrless drilling by vibration cutting applying ultrasonic torsional mode vibration," *Transactions of the North American Manufacturing Research Institution of SME 2005, Vol 33, 2005,* vol. 33, pp. 461-468, 2005.

[52] H. Takeyama and S. Kato, "Burrless drilling by means of ultrasonic vibration," *Cirp Annals-Manufacturing Technology,* vol. 40, pp. 83-86, 1991.

[53] S. Aoki, S. Hirai, and T. Nishimura, "Prevention from delamination of composite material during drilling using ultrasonic vibration," *Advances in Abrasive Technology Viii,* vol. 291-292, pp. 465-470, 2005.

[54] C. S. Liu, B. Zhao, G. F. Gao, and X. H. Zhang, "Study on ultrasonic vibration drilling of particulate reinforced aluminum matrix composites," *Advances in Abrasive Technology Viii,* vol. 291-292, pp. 447-452, 2005.

[55] L. Balamuth, "Ultrasonic Assistance to Conventional Metal Removal," *Ultrasonics,* vol. 4, pp. 125-&, 1966.

[56] G. L. Chern and J. M. Liang, "Study on boring and drilling with vibration cutting," *International Journal of Machine Tools & Manufacture,* vol. 47, pp. 133-140, Jan 2007.

[57] E. Neppiras, "Ultrasonic machining and forming," *Ultrasonics,* vol. 2, pp. 167-173, 1964.

[58] J. Pujana, A. Rivero, A. Celaya, and L. N. L. de Lacalle, "Analysis of ultrasonic-assisted drilling of Ti6Al4V," *International Journal of Machine Tools & Manufacture,* vol. 49, pp. 500-508, May 2009.

[59] X. Wang, L. J. Wang, and J. P. Tao, "Investigation on thrust in vibration drilling of fiber-reinforced plastics," *Journal of Materials Processing Technology,* vol. 148, pp. 239-244, May 15 2004.

[60] P. Guzzo, A. Shinohara, and A. Raslan, "A comparative study on ultrasonic machining of hard and brittle materials," *Journal of the Brazilian Society of Mechanical Sciences and Engineering,* vol. 26, pp. 56-61, 2004.

[61] A. Celaya, L. N. L. de Lacalle, F. J. Campa, and A. Lamikiz, "Ultrasonic Assisted Turning of mild steels," *International Journal of Materials & Product Technology,* vol. 37, pp. 60-70, 2010.

[62] P. Mehbudi, V. Baghlani, J. Akbari, A. R. Bushroa, and N. A. Mardi, "Applying ultrasonic vibration to decrease drilling-induced delamination in GFRP laminates," *Proceedings of the Seventeenth Cirp Conference on Electro Physical and Chemical Machining (Isem),* vol. 6, pp. 577-582, 2013.

[63] A. Sadek, M. H. Attia, M. Meshreki, and B. Shi, "Characterization and optimization of vibration-assisted drilling of fibre reinforced epoxy laminates," *Cirp Annals-Manufacturing Technology,* vol. 62, pp. 91-94, 2013.

[64] K. Alam, A. V. Mitrofanov, and V. V. Silberschmidt, "Experimental investigations of forces and torque in conventional and ultrasonically-assisted drilling of cortical bone," *Medical Engineering & Physics,* vol. 33, pp. 234-239, Mar 2011.

[65] M. Yang and J. D. Zahn, "Microneedle insertion force reduction using vibratory actuation," *Biomedical Microdevices,* vol. 6, pp. 177-182, Sep 2004.

[66] Y. C. Huang, M. C. Tsai, and C. H. Lin, "A piezoelectric vibration-based syringe for reducing insertion force," *International Symposium on Ultrasound in the Control of Industrial Processes (Ucip 2012),* vol. 42, 2012.

[67] H. Izumi, T. Yajima, S. Aoyagi, N. Tagawa, Y. Arai, and M. Hirata, "Combined harpoonlike jagged microneedles imitating mosquito's proboscis and its insertion experiment with vibration," *Ieej Transactions on Electrical and Electronic Engineering,* vol. 3, pp. 425-431, Jul 2008.

[68] N. D. Begg and A. H. Slocum, "Audible frequency vibration of puncture-access medical devices," *Med Eng Phys,* vol. 36, pp. 371-7, Mar 2014.

[69] D. Bi and Y. Lin, "Vibrating Needle Insertion for Trajectory Optimization," *2008 7th World Congress on Intelligent Control and Automation, Vols 1-23,* pp. 7444-7448, 2008.

[70] K. G. Yan, W. S. Ng, K. V. Ling, T. I. Liu, Y. Yu, and T. Podder, "High frequency translational oscillation & rotational drilling of the needle in reducing target movement," *2005 IEEE International Symposium on Computational Intelligence in Robotics and Automation, Proceedings,* pp. 163-168, 2005.

[71] A. C. Barnett, Y.-S. Lee, and J. Z. Moore, "Fracture Mechanics Model of Needle Cutting Tissue," *Journal of Manufacturing Science and Engineering,* vol. 138, 2016.

[72] J. R. Crouch, C. M. Schneider, J. Wainer, and A. M. Okamura, "A velocity-dependent model for needle insertion in soft tissue," *Medical Image Computing and Computer-Assisted Intervention - Miccai 2005, Pt 2,* vol. 3750, pp. 624-632, 2005.

[73] K. G. Yan, T. Podder, Y. Yu, T.-I. Liu, C. W. S. Cheng, and W. S. Ng, "Flexible needle–tissue interaction modeling with depth-varying mean parameter: preliminary study," *Biomedical Engineering, IEEE Transactions on,* vol. 56, pp. 255-262, 2009.

[74] E. Dehghan, X. Wen, R. Zahiri-Azar, M. Marchal, and S. E. Salcudean, "Modeling of needle-tissue interaction using ultrasound-based motion estimation," *Medical Image Computing and Computer-Assisted Intervention - MICCAI 2007, Pt 1, Proceedings,* vol. 4791, pp. 709-716, 2007.

[75] A. M. Okamura, C. Simone, and M. D. O'Leary, "Force modeling for needle insertion into soft tissue," *Ieee Transactions on Biomedical Engineering,* vol. 51, pp. 1707-1716, Oct 2004.

[76] R. J. Roesthuis, Y. R. van Veen, A. Jahya, and S. Misra, "Mechanics of needle-tissue interaction," in *Intelligent Robots and Systems (IROS), 2011 IEEE/RSJ International Conference on*, 2011, pp. 2557-2563.

[77] O. A. Shergold and N. A. Fleck, "Mechanisms of deep penetration of soft solids, with application to the injection and wounding of skin," *Proceedings of the Royal Society a-Mathematical Physical and Engineering Sciences,* vol. 460, pp. 3037-3058, Oct 8 2004.

[78] S. Misra, K. B. Reed, B. W. Schafer, K. T. Ramesh, and A. M. Okamura, "Mechanics of Flexible Needles Robotically Steered through Soft Tissue," *International Journal of Robotics Research,* vol. 29, pp. 1640-1660, Nov 2010.

[79] M. Mahvash and P. E. Dupont, "Mechanics of Dynamic Needle Insertion into a Biological Material," *Ieee Transactions on Biomedical Engineering,* vol. 57, pp. 934-943, Apr 2010.

[80] T. L. Anderson, *Fracture mechanics: fundamentals and applications*: CRC press, 2005.

[81] A. G. Atkins and Y.-W. Mai, *Elastic and plastic fracture: metals, polymers, ceramics, composites, biological materials*: Ellis Horwood; Halsted Press, 1985.

[82] T. Azar and V. Hayward, "Estimation of the fracture toughness of soft tissue from needle insertion," *Biomedical Simulation, Proceedings,* vol. 5104, pp. 166-175, 2008.

[83] M. Mahvash and V. Hayward, "Haptic rendering of cutting: A fracture mechanics approach," *Haptics-e,* vol. 2, pp. 1-12, 2001.

[84] O. A. Shergold and N. A. Fleck, "Experimental investigation into the deep penetration of soft solids by sharp and blunt punches, with application to the piercing of skin," *Journal of Biomechanical Engineering-Transactions of the Asme,* vol. 127, pp. 838-848, Oct 2005.

[85] B. H. Newman and D. A. Waxman, "Blood donation-related neurologic needle injury: Evaluation of 2 years' worth of data from a large blood center," *Transfusion,* vol. 36, pp. 213-215, Mar 1996.

[86] M. Ogorman, P. Trabulsy, and D. B. Pilcher, "Zero-Time Prehospital-Iv," *Journal of Trauma-Injury Infection and Critical Care,* vol. 29, pp. 84-86, Jan 1989.

[87] P. J. Westenend, A. R. Sever, H. J. Beekman-de Volder, and S. J. Liem, "A comparison of aspiration cytology and core needle biopsy in the evaluation of breast lesions," *Cancer Cytopathology,* vol. 93, pp. 146-150, 2001.

[88] V. Tangpricha, B. Chen, N. Swan, A. Sweeney, A. de las Morenas, and J. Safer, "Twenty-one-gauge needles provide more cellular samples than twenty-five-gauge needles in fine-needle aspiration biopsy of the thyroid but may not provide increased diagnostic accuracy," *Thyroid,* vol. 11, pp. 973-976, 2001.

[89] W. L. Atkinson, L. K. Pickering, B. Schwartz, B. G. Weniger, J. K. Iskander, and J. C. Watson, "General recommendations on immunization," *Recommendations of the Advisory Committee on Immunization Practices (ACIP) and the American Academy of Family Physicians (AAFP) MMWR Recomm Rep,* vol. 51, pp. 1-35, 2002.

[90] H. S. Gill and M. R. Prausnitz, "Does needle size matter?," *Journal of diabetes science and technology,* vol. 1, pp. 725-729, 2007.

[91] L. Hiemenz, A. Litsky, and P. Schmalbrock, "Puncture mechanics for the insertion of an epidural needle," in *Proceedings of the Twenty-First Annual Meeting of the American Society of Biomechanics*, 1997.

[92] C. S. McGill, J. A. Schwartz, J. Z. Moore, P. W. McLaughlin, and A. J. Shih, "Precision grid and hand motion for accurate needle insertion in brachytherapy," *Medical Physics,* vol. 38, pp. 4749-4759, Aug 2011.

[93] J. Ankersen, A. E. Birkbeck, R. D. Thomson, and P. Vanezis, "Puncture resistance and tensile strength of skin simulants," *Proceedings of the Institution of Mechanical Engineers Part H-Journal of Engineering in Medicine,* vol. 213, pp. 493-501, 1999.

[94] F. H. Silver, J. W. Freeman, and D. DeVore, "Viscoelastic properties of human skin and processed dermis," *Skin Research and Technology,* vol. 7, pp. 18-23, 2001.

[95] A. N. Annaidh, K. Bruyère, M. Destrade, M. D. Gilchrist, and M. Otténio, "Characterization of the anisotropic mechanical properties of excised human skin," *Journal of the mechanical behavior of biomedical materials,* vol. 5, pp. 139-148, 2012.

[96] B. Zhou, F. Xu, C. Q. Chen, and T. J. Lu, "Strain rate sensitivity of skin tissue under thermomechanical loading," *Philosophical Transactions of the Royal Society a-Mathematical Physical and Engineering Sciences,* vol. 368, pp. 679-690, Feb 13 2010.

[97] J. Vincent, *Structural biomaterials*: Princeton University Press, 2012.

[98] R. K. Nalla, J. S. Stolken, J. H. Kinney, and R. O. Ritchie, "Fracture in human cortical bone: local fracture criteria and toughening mechanisms," *Journal of Biomechanics,* vol. 38, pp. 1517-1525, Jul 2005.

[99] R. W. Ogden, G. Saccomandi, and I. Sgura, "Fitting hyperelastic models to experimental data," *Computational Mechanics,* vol. 34, pp. 484-502, Nov 2004.

[100] C. Gokgol, C. Basdogan, and D. Canadinc, "Estimation of fracture toughness of liver tissue: Experiments and validation," *Medical engineering & physics,* vol. 34, pp. 882-891, Sep 2012.

[101] B. P. Pereira, P. W. Lucas, and T. SweeHin, "Ranking the fracture toughness of thin mammalian soft tissues using the scissors cutting test," *Journal of Biomechanics,* vol. 30, pp. 91-94, Jan 1997.
[102] P. P. Purslow, "Measurement of the Fracture-Toughness of Extensible Connective Tissues," *Journal of Materials Science,* vol. 18, pp. 3591-3598, 1983.
[103] O. A. Shergold, N. A. Fleck, and D. Radford, "The uniaxial stress versus strain response of pig skin and silicone rubber at low and high strain rates," *International Journal of Impact Engineering,* vol. 32, pp. 1384-1402, Sep 2006.
[104] A. C. Barnett, K. Wolkowicz, and J. Z. Moore, "Vibrating Needle Cutting Force," in *ASME 2014 International Manufacturing Science and Engineering Conference*, Detroit, Michigan, 2014.
[105] A. C. Barnett, A. M. Abdullah, A. Gordon, and J. Z. Moore, "Vibration Tissue Cutting for Blunt Hollow Needle," in *41st North American Manufacturing Research Conference*, Madison, Wisconsin, 2013.
[106] E. A. Bolyard, O. C. Tablan, W. W. Williams, M. L. Pearson, C. N. Shapiro, S. D. Deitchman*, et al.*, "Guideline for infection control in health care personnel, 1998," *American Journal of Infection Control,* vol. 26, pp. 289-354, Jun 1998.
[107] K. Henry and S. Campbell, "Needlestick/sharps injuries and HIV exposure among health care workers. National estimates based on a survey of US hospitals," *Minnesota medicine,* vol. 78, p. 41, 1995.
[108] J. P. Leigh, M. Gillen, P. Franks, S. Sutherland, H. H. Nguyen, K. Steenland*, et al.*, "Costs of needlestick injuries and subsequent hepatitis and HIV infection," *Current Medical Research and Opinion,* vol. 23, pp. 2093-2105, Sep 2007.
[109] M. Mendelson, R. Sperling, M. Brodman, P. Dottino, J. Morrow, J. Solomon*, et al.*, "Evaluation of blunt suture needles in preventing percutaneous injuries among health-care workers during gynecologic surgical procedures - New York City, March 1943 June 1994 (Reprinted from MMWR, vol 46, pg 25-29, 1997)," *Jama-Journal of the American Medical Association,* vol. 277, pp. 451-452, Feb 12 1997.
[110] M. Davis, "How Blunt is Blunt? Choosing and Using Blunt Suture Needles," *Advances in Exposure Prevention,* vol. 7, p. 25, 2005.
[111] J. Z. Moore and A. J. Shih, "Tissue oblique cutting flow angle and needle insertion contact length," *Transactions of NAMRI/SME,* vol. 38, pp. 711-718, 2010.
[112] J. Z. Moore, Q. H. Zhang, C. S. McGill, H. J. Zheng, P. W. McLaughlin, and A. J. Shih, "Modeling of the Plane Needle Cutting Edge Rake and Inclination Angles for Biopsy," *Journal of Manufacturing Science and Engineering-Transactions of the Asme,* vol. 132, Oct 2010.
[113] J. Z. Moore, Q. H. Zhang, C. S. McGill, H. J. Zheng, P. W. McLaughlin, and A. J. Shih, "Modeling cutting edge geometry for plane and curved needle tips," *Proceedings of the Institution of Mechanical Engineers Part B-Journal of Engineering Manufacture,* vol. 226, pp. 861-869, May 2012.
[114] J. E. Heavner, G. B. Racz, B. Jenigiri, T. Lehman, and M. R. Day, "Sharp versus blunt needle: A comparative study of penetration of internal structures and bleeding in dogs," *Proceedings of the 12th International Pain Clinic: World Society of Pain Clinicians,* pp. 263-270, 2006.
[115] A. Mingoli, P. Sapienza, G. Sgarzini, G. Luciani, G. DeAngelis, C. Modini*, et al.*, "Influence of blunt needles on surgical glove perforation and safety for the surgeon," *American Journal of Surgery,* vol. 172, pp. 512-517, Nov 1996.
[116] J. E. Hartley, S. Ahmed, R. Milkins, G. Naylor, J. R. T. Monson, and P. W. R. Lee, "Randomized trial of blunt-tipped versus cutting needles to reduce glove puncture during

mass closure of the abdomen," *British Journal of Surgery,* vol. 83, pp. 1156-1157, Aug 1996.

[117] T. Washio and K. Chinzei, "Needle force sensor, robust and sensitive detection of the instant of needle puncture," *Medical Image Computing and Computer-Assisted Intervention - Miccai 2004, Pt 2, Proceedings,* vol. 3217, pp. 113-120, 2004.

[118] M. D. Gilchrist, S. Keenan, M. Curtis, M. Cassidy, G. Byrne, and M. Destrade, "Measuring knife stab penetration into skin simulant using a novel biaxial tension device," *Forensic Science International,* vol. 177, pp. 52-65, May 2 2008.

[119] C. T. McCarthy, M. Hussey, and M. D. Gilchrist, "On the sharpness of straight edge blades in cutting soft solids: Part I - indentation experiments," *Engineering Fracture Mechanics,* vol. 74, pp. 2205-2224, Sep 2007.

[120] A. J. Shih, M. A. Lewis, and J. S. Strenkowski, "End milling of elastomers - Fixture design and tool effectiveness for material removal," *Journal of Manufacturing Science and Engineering-Transactions of the Asme,* vol. 126, pp. 115-123, Feb 2004.

[121] L. L. Howell, *Compliant mechanisms*: John Wiley & Sons, 2001.

[122] N. V. Datla, B. Konh, and P. Hutapea, "A flexible active needle for steering in soft tissues," in *Northeast Bioengineering Conference (NEBEC), 2014 40th Annual*, 2014, pp. 1-2.

[123] T. K. Podder, A. P. Dicker, P. Hutapea, K. Darvish, and Y. Yu, "A novel curvilinear approach for prostate seed implantation," *Medical Physics,* vol. 39, pp. 1887-1892, Apr 2012.

[124] S. C. Ryu, P. Renaud, R. J. Black, B. L. Daniel, and M. R. Cutkosky, "Feasibility Study of an Optically Actuated MR-compatible Active Needle," *2011 Ieee/Rsj International Conference on Intelligent Robots and Systems,* 2011.

[125] V. Lagerburg, M. A. Moerland, J. J. W. Lagendijk, and J. J. Battermann, "Measurement of prostate rotation during insertion of needles for brachytherapy," *Radiotherapy and Oncology,* vol. 77, pp. 318-323, Dec 2005.

[126] N. Lobontiu, *Compliant mechanisms: design of flexure hinges*: CRC press, 2002.

[127] D. Tcherniak, "Topology optimization of resonating structures using SIMP method," *International Journal for Numerical Methods in Engineering,* vol. 54, pp. 1605-1622, Aug 20 2002.

[128] L. Meirovitch, *Analytical methods in vibration*. New York, NY: The MacMillan Company, 1967.

[129] G. F. Benedict, *Nontraditional manufacturing processes* vol. 19: CRC Press, 1987.

[130] K. H. W. Seah, Y. S. Wong, and L. C. Lee, "Design of Tool Holders for Ultrasonic Machining Using Fem," *Journal of Materials Processing Technology,* vol. 37, pp. 801-816, Feb 1993.

Vita

Andrew Barnett received his B.S. in Mechanical Engineering from Johns Hopkins University in May 2011. While there he conducted research into the microscale mechanical properties of superalloys and carbon-carbon composites. In August of 2011 he joined Pennsylvania State University in pursuit of a doctoral degree. Once there, he began researching needle insertion mechanics. His research interests include tissue cutting, medical device design, and structural dynamics.

SELECT PUBLICATIONS

[1] **A. C. Barnett**, Y.-S. Lee, and J. Z. Moore, "Fracture Mechanics Model of Needle Cutting Tissue," *Journal of Manufacturing Science and Engineering,* 2015.

[2] **A. C. Barnett**, M. Freidner, and J. Z. Moore, "Vibration Needle Tissue Cutting with Varying Tip Geometry," in *ASME 2015 International Manufacturing Science and Engineering Conference*, Charlotte, NC, 2015.

[3] A. Gordon, I. Kim, **A. C. Barnett**, and J. Z. Moore, "Needle Insertion Force Model for Haptic Simulation," in *ASME 2015 International Manufacturing Science and Engineering Conference*, Charlotte, NC, 2015.

[4] P. P. Shetty, R. W. Hatton, **A. C. Barnett**, A. J. Homich, and J. Z. Moore, "Modeling the cutting edge geometry of scalpel blades," *Proceedings of the Institution of Mechanical Engineers, Part B: Journal of Engineering Manufacture*, 2015.

[5] **A. C. Barnett**, K. Wolkowicz, and J. Z. Moore, "Vibrating Needle Cutting Force," in *ASME 2014 International Manufacturing Science and Engineering Conference*, Detroit, Michigan, 2014.

[6] **A. C. Barnett**, A. M. Abdullah, A. Gordon, and J. Z. Moore, "Vibration Tissue Cutting for Blunt Hollow Needle," in *41st North American Manufacturing Research Conference*, Madison, Wisconsin, 2013.

[7] **A. C. Barnett**, P. W. McLaughlin, H. Zheng, and J. Z. Moore, "Novel Instant Vacuum Biopsy Needle System," in *ASME 2013 International Design Engineering Technical Conferences and Computers and Information in Engineering Conference*, 2013.

[8] M. Doerzbacher, **A. C. Barnett**, N. Brandmeir, D. Wolfe, S. Y. Zheng, and J. Moore, "Advanced Needle Coatings for Improved Lumbar Drain Procedure," *Journal of Medical Devices-Transactions of the ASME,* vol. 7, Sep 2013.

[9] A. M. Abdullah, **A. C. Barnett**, C. Golecki, D. E. Wolfe, and J. Z. Moore, "Investigation of Friction in Needle to Soft Tissue Interaction," in *North American Manufacturing Research Conference*, Madison, Wisconsin, 2013.

[10] A. Abdullah, C. Golecki, **A. C. Barnett**, and J. Moore, "Surface Texture and Insertion Speed Effect On Needle Friction," *Medical Physics,* vol. 39, pp. 3612-3612, Jun 2012.